



ADVERTIMENT. L'accés als continguts d'aquesta tesi queda condicionat a l'acceptació de les condicions d'ús establertes per la següent llicència Creative Commons:  <https://creativecommons.org/licenses/?lang=ca>

ADVERTENCIA. El acceso a los contenidos de esta tesis queda condicionado a la aceptación de las condiciones de uso establecidas por la siguiente licencia Creative Commons:  <https://creativecommons.org/licenses/?lang=es>

WARNING. The access to the contents of this doctoral thesis it is limited to the acceptance of the use conditions set by the following Creative Commons license:  <https://creativecommons.org/licenses/?lang=en>



Universitat Autònoma de Barcelona
Autonomous University of Barcelona
Faculty of Science, Physics Department

Innovative Approximation Methods in QCD and Flavor Physics.

A thesis submitted to the Doctoral School and Physics Department for the degree of
PHILOSOPHIAE DOCTOR

BY

CAMILO ALEJANDRO ROJAS PACHECO

SUPERVISOR

Prof. PhD. PERE MASJUAN QUERALT

TUTOR

Prof. PhD. RAFEL ESCRIBANO

Barcelona, Spain

© 2024

Abstract

This thesis explores the application of Padé and D-Log Padé approximants in Quantum Chromodynamics (QCD), focusing on their potential to model divergent functions while maintaining essential analytical properties. We propose a new convergence conjecture for D-Log Padé approximants in the case of Stieltjes functions and perform a comparative analysis of both techniques across several QCD-related scenarios. These include determining the anomalous magnetic moment of the muon, parameterising form factors in B-meson decays. Our findings demonstrate the effectiveness of these approximants in reducing uncertainties and improving parameterisations of expressions with poles or branch cuts.

Keywords

- *Padé and D-Log approximants,*
- *Flavour Physics,*
- *CKM unitarity,*
- *Form Factors B- meson decays*
- *Anomalous magnetic dipole moment of Muon*

Dedicatory

I dedicate this work to my wife, my greatest love, the reason and the bliss in my life, who gives color to my equations and smiles to my ideas, the beauty who give me the courage and happiness which I need every day in my job.

Porque este logro es tan tuyo como mío. ¡Para ti, hermosa!

Acknowledgment

I would like to express my deepest gratitude to the theoretical research group at IFAE for providing me with the opportunity to be a part of such a vibrant and stimulating academic environment. The guidance, support, and valuable insights from my colleagues and mentors have been crucial in shaping my research. Their expertise and encouragement have greatly contributed to both my professional growth and the completion of this work. I am truly thankful for the inspiring discussions with my thesis director Pere Masjuan.

Pere, tú has demostrado ser una persona con gran amabilidad y carisma en cada uno de los días que trabajamos juntos. Fue un privilegio poder ser parte de nuestro grupo de investigación, donde aprendí y aclaré conceptos, además de desarrollar herramientas que seguramente me serán muy útiles en la vida. Pero, sobre todo, fue maravilloso poder hacer grandes amigos allí. He podido compartir contigo ideas tanto en lo académico como en lo personal, lo que me ha dado un referente de cómo me gustaría ser en mi vida profesional. Sabes despertar un gran asombro por la física en todos los niveles de enseñanza, y pienso que esto es fundamental como científico para conectar con las nuevas generaciones que quieren ser parte de la comunidad científica. Gracias, Pere, por tu dirección y tu amistad.

Por supuesto, quiero agradecer a todos aquellos que me acompañaron en este camino. Rafel, siempre estuviste abierto a las pequeñas tertulias en los pasillos del IFAE y a ayudarme en todo lo que necesitaba. También agradezco por su amistad y colaboración a todos los miembros del BreakingBad Group; estoy seguro de que todos tuvimos momentos en los que aprendimos montones. Arnau, gracias por tu amistad y tu compañía. Pudimos compartir excelentes momentos en Mainz, y seguro habrá futuras ocasiones donde volveremos a encontrarnos. Mucho obrigado, Cristiane! Fue un año en el que pude disfrutar de tu compañía, de tus risas y de tu ayuda en el trabajo. También le agradezco a Sergi por su amistad y su colaboración.

Gracias, corazón, por toda tu ayuda y tu compañía, por escucharme tantas horas y por ser parte de esta aventura que nos ha dado risas y llantos, pero que nos llena de vida y nos

hace ser quienes somos.

A toda mi familia quiero darle un agradecimiento especial, porque este esfuerzo representa un logro que comenzó cuando era niño, y gracias a su compañía y al soporte que mi papá, mi mamá y mi hermano me han dado toda su vida es que he podido llegar lejos y cumplir tantos logros académicos y de vida. Además, tuvimos la oportunidad de viajar y disfrutar de tantos lugares por Europa; gracias por visitarnos y llevar la calidez de la familia a la ciudad condal.

Gracias por todo el apoyo financiero que me ofreció Colombia mediante los programas de crédito-beca de Colfuturo y el programa de doctorados en el exterior de Colciencias.

Contents

Abstract	iii
Introduction	XIII
1 Quantum Chromodynamics Theory	1
1.1 QCD Fundamentals	1
1.2 Non-Perturbative QCD and Effective Approaches	3
1.3 Challenges in QCD	5
1.4 Summary & highlights	6
2 Convergence Techniques and Padé Theory	7
2.1 Padé approximants	8
2.1.1 Canonical construction of a Padé approximant	9
2.1.2 Convergence for meromorphic functions	11
2.1.3 Convergence for Stieltjes functions	13
2.1.4 Extensions of Padé approximants	17
2.2 D-log Padé approximants	18
2.2.1 Canonical construction of D-Logs	20
2.2.2 Extensions of D-Log approximants	23
2.3 Recap of convergence techniques	24
3 About convergence in D-Log Padé approximants	27
3.1 Convergence for the Taylor expansion	27
3.2 Conjecture of convergence for Stieltjes functions	29
3.2.1 Example 1. "Stieltjes logarithm"	32
3.2.2 Example 2: "Stieltjes Exponential Integral"	34

4	Extrapolation MUonE data to find a_μ	37
4.1	Hadronic Vacuum Polarization of a_μ	40
4.1.1	$\Delta\alpha_{\text{had}}(t)$ Analytic Properties	42
4.2	A model for the Euclidean correlator	43
4.3	approximants to the Taylor series	45
4.3.1	Convergence of PAs results	45
4.3.2	Convergence of D-Logs and comparison with PAs results	47
4.4	approximants to data with no error	49
4.5	approximants to data with realistic errors	55
4.6	Summary & highlights	64
5	V_{ub} determination	67
5.1	Lagrangian - Decay Amplitude and Form Factors	71
5.2	PAs and D-Logs apply to z-parameterisation	73
5.2.1	Padé Approximation	76
5.2.2	D-Log Padé Approximation	80
5.3	Fits to the decay $B \rightarrow \pi l \nu_\ell$	86
5.4	Fits to the decay $B_s \rightarrow K l \nu_\ell$	95
5.5	Combined fits to the decays $B \rightarrow \pi l \nu_\ell$ and $B_s \rightarrow K l \nu_\ell$	99
5.6	Phenomenological Applications	104
5.7	Summary & highlights	108
6	Findings and Conclusions	113
A	Notation	115
B	Fitting functions for PAs and D-Logs	117
C	B-meson Form Factors simulation & correlation tables	119
	Bibliografy	121

List of Tables

2.1	Singularities determined by D-Logs in an example function	22
4.1	Fitting functions constructed as PAs to determined $a_\mu^{\text{HVP,LO}}$	51
4.2	Fitting functions constructed as D-Logs to determined $a_\mu^{\text{HVP,LO}}$	53
4.3	Results for $a_\mu^{\text{HVP,LO}}$ from the PAs and D-Logs	59
4.4	Final results for $a_\mu^{\text{HVP,LO}}$ from PAs, D-Logs, the Toy-model and QED-model varying the extrapolation range	60
5.1	Input meson masses used in the z -parameterisation.	75
5.2	Recent z -parameterisation coefficients provided by FLAG and FNAL/MILC	75
5.3	Comparison of convergence between PAs and D-Logs approaching to the vector form factor.	86
5.4	Synthetic data used to fit $B \rightarrow \pi$ vector and scalar form factors, based on FLAG results of 2019 Review	88
5.5	Fitting results for $B \rightarrow \pi$ using Padé sequences of the type P_1^M and P_2^M . .	90
5.6	Fitting results for $B \rightarrow \pi$ using Padé sequences of the type \mathbb{T}_1^M and $\mathbb{P}_{1,1}^M$. .	90
5.7	Fitting results only for the vector form factor using P_1^M in the channel $B \rightarrow \pi$	92
5.8	Fitting results for $B \rightarrow \pi$ using D-Log sequences of the type D_1^N and D_2^N .	93
5.9	Fitting results for $B \rightarrow \pi$ using D-Log sequences of the type $\mathbb{PD}_{0,1}^N$ and $\mathbb{PD}_{1,1}^N$	93
5.10	Synthetic data used to fit $B_s \rightarrow K$ vector and scalar form factors, based on FNAL/MILC results of 2019	96
5.11	Best fitting results using PAs, PPAs and TPAs for $B_s \rightarrow K$ decay	97
5.12	Best fitting results using D-Logs and Partial D-Logs for $B_s \rightarrow K$ decay . . .	99
5.13	Best result for the combined fit and the corresponding correlation matrix using PAs	101

5.14 Best result for the combined fit and the corresponding correlation matrix using D-Logs	102
C.1 Fitting results and correlation matrix for $\mathbb{P}_{1,1}^2$ in $B \rightarrow \pi$ decay	119
C.2 Synthetic data using to fit only the $B \rightarrow \pi$ vector form factor	120
C.3 Fitting results and correlation matrix for $\mathbb{P}_{1,1}^3$ in $B_s \rightarrow K$ decay	120

Introduction

One of the major successes in the history of science is the high predictive power of the Standard Model (SM) of particle physics. This model provides a framework for understanding the subatomic world through a set of fundamental particles and the interactions between them. Based on quantum field theory, the Standard Model effectively describes the behaviors associated with basically two types of interactions: the electroweak sector (EW), which encompasses the weak nuclear and electromagnetic interactions, and Quantum Chromodynamics (QCD), which deals with the strong nuclear interaction. While both sectors are the focus of active research, this work will specifically address some of the challenges associated with the physics of the strong force.

From a mathematical standpoint, into the formulations of QCD, various analytical expressions may exhibit points of divergence, manifesting as poles or branch cuts. These singularities hold significance within both perturbative and non-perturbative regimes of QCD calculations¹. In many physical systems, obtaining exact theoretical formulations for several of these expressions proves challenging, lacking a generic modelling approach. Among these expressions are hadronic structure functions and Form Factors involved in diverse hadronic processes. Additionally, QCD theory entails Green's functions, including propagators or Kernel Functions with the same type of structures. Despite their theoretical importance, a precise parameterisation of these expressions remains an ongoing challenge due to the complex nature of QCD interactions.

The lack of precision and certainty when modeling divergence points can result in a possible source of error or uncertainty in the calculation of observables. Therefore, it is crucial to develop highly efficient and precise methods for modeling these divergent functions. These methods must also adhere to the analytical properties established by QCD.

¹A detailed explanation about these two types of regimes will be presented in Section 1.1

We aim to present and evaluate two powerful and promising tools for this task: Padé approximants and D-Log Padé approximants. The former has been successfully studied in various scenarios, demonstrating excellent precision in many hadronic computations. The latter, an innovative technique, has been recently considered for modeling divergent functions in QCD, specially to reproduce branch cuts. In this thesis, we will conduct an in-depth exploration of D-Log Padé approximants and provide a comparative analysis with Padé approximants. Overall, these two techniques could offer improved parameterisations of expressions involving poles or branch cuts, potentially outperforming existing models.

What makes our approach unique is the application of both Padé and D-Log Padé approximants, which are model-independent methods, and testing them in some QCD scenarios. These techniques offer distinct advantages over traditional approaches. First, Padé approximants possess a robust theoretical framework that aligns well with the parameterisation needs of QCD expressions, even when these expressions are not precisely known but must adhere to certain analytical properties. Moreover, these approximants reduce uncertainties due to their fast convergence, improving the precision of calculations. While Padé functions have shown great success, certain limitations they present in complex scenarios can be addressed by D-Log Padé approximants, which introduce a richer analytical structure. This dual approach provides a more versatile and accurate modeling framework for QCD.

While Padé approximants have been extensively studied and successfully applied in various QCD contexts, the exploration of D-Log Padé approximants remains incomplete in the current literature. Although a few articles have begun incorporating D-Log ideas, there is no comprehensive analysis available. In this thesis, for instance we present a novel convergence conjecture for D-Log Padé approximants specifically in the case of Stieltjes functions, which has not been addressed before. Additionally, we test both Padé and D-Log Padé approximants across three different scenarios, providing a detailed comparative analysis of their convergence behavior. This work not only expands the understanding of D-Log Padé approximants but also offers a direct comparison with traditional Padé methods, highlighting the potential of D-Logs to overcome certain limitations of the latter.

The thesis is organized to progressively introduce the reader to both the theoretical foundations and the novel applications of Padé and D-Log Padé approximants in some QCD scenarios. In **Chapter 1**, we provide a brief introduction to QCD theory, presenting the most essential concepts that frame our work. This chapter includes a section discussing non-perturbative and effective approaches, such as lattice QCD, chiral perturbation theory, and the Large N_c expansion, which are key tools in addressing the complexities of QCD. We

also dedicate a section to some of the major challenges in QCD, highlighting the hadronic scenarios where our approximants will be tested. In **Chapter 2**, we delve into the theoretical fundamentals of both Padé and D-Log Padé approximants. We explain their canonical construction, explore other related rational approximants and their extensions, and present key convergence theorems, particularly those related to meromorphic and Stieltjes functions. Following this, **Chapter 3** is devoted entirely to presenting a new convergence conjecture for using D-Log Padé approximants to approximate Stieltjes functions, which is a central contribution of this thesis. Moving into the applied part of the work, **Chapter 4** introduces the first scenario where both techniques —Padé and D-Log Padé approximants— are employed to fit experimental data and determine the anomalous magnetic moment of the muon. **Chapter 5** presents a second application, where we use these approximants to parameterise vector and scalar form factors in semileptonic decays of the B meson, with the goal of determining the CKM matrix element V_{ub} . Finally, we summarize our findings and present the conclusions of the thesis, reflecting on the implications of the results and potential directions for future research.

Quantum Chromodynamics Theory

The Standard Model (SM) of particle physics is a Yang-Mills¹ gauge theory that describes the fundamental interactions at a microscopic level with unprecedented success. It is based on the symmetry group $SU(3)_c \times SU(2)_I \times U(1)_Y$, where $SU(3)_c$ represents the strong interaction, also known as Quantum Chromodynamics (QCD). This chapter will present the essentials of QCD, which describes the behavior of quarks and gluons, the fundamental constituents of hadronic particles such as protons, neutrons, and all kind of mesons. QCD serves as the physical theoretical framework for later chapters, especially in the context of precision tests involving the anomalous magnetic moment of the muon (see. Chapter 4) or hadronic form factors (see. Chapter 5). Additionally, we will discuss the role of Chiral Perturbation Theory in describing low-energy meson dynamics and its connections to large- N_c approximations.

1.1 QCD Fundamentals

QCD is a Yang-Mills gauge theory based on the $SU(3)_c$ symmetry group, where the subscript c refers to color charge which is the one associated with the strong interaction. The theory describes six types (flavors) of quarks –up (u), down (d), strange (s), charm (c), bottom (b) and top (t)– interacting via gluons, the force carriers of QCD. Quarks transform under the fundamental representation of $SU(3)_c$, meaning they color charge is: red, green or

¹Yang-Mills theory is a gauge theory based on non-Abelian Lie groups, where the gauge fields mediate interactions between particles.

blue². The gluons, in contrast, transform under the adjoint representation of $SU(3)_c$, and there are eight distinct gluons that also are charged and could interact between them [1–3].

The QCD Lagrangian is given by [4]:

$$\mathcal{L}_{\text{QCD}} = \sum_{i=1}^{N_f} \bar{q}_i (i\not{D} - m_i) q_i - \frac{1}{4} G_{\mu\nu}^a G^{a,\mu\nu}, \quad (1.1)$$

where q_i represents the quark fields (with N_f flavors), m_i is the quark mass³, and $\not{D} = \gamma^\mu D_\mu$ with γ^μ the Dirac matrices (see Appendix A), refers to the covariant derivative defined as:

$$D_\mu = \partial_\mu - ig_s T^a A_\mu^a \quad (1.2)$$

Here, g_s is the strong coupling constant, A_μ^a represents the 8 gluon fields, and T^a are the generators of the $SU(3)_C$ group. The term $G_{\mu\nu}^a$ represents the gluon field strength tensor, defined as:

$$G_{\mu\nu}^a = \partial_\mu A_\nu^a - \partial_\nu A_\mu^a + g_s f^{abc} A_\mu^b A_\nu^c \quad (1.3)$$

where f^{abc} are the structure constants of $SU(3)_c$, which are defined from $[t^a, t^b] = i f^{abc} t^c$.

The QCD Lagrangian encodes several key properties of the strong interaction, including confinement and asymptotic freedom [4]. In this context, the coupling constant g_s plays a crucial role in determining the strength of interactions at different energy scales, providing deeper insight into the phenomena of confinement and asymptotic freedom.

Two regimes in QCD

In any QFT, renormalization effects cause the coupling constant to vary with energy, a phenomena known as running. This energy dependence is governed by the renormalization group (RG) equations for the coupling constant, defined as $\alpha_s = \frac{g_s^2}{4\pi}$ [5, ch. 9].

$$\mu^2 \frac{d\alpha_s}{d\mu^2} = \beta(\alpha_s) = -\alpha_s \left(\beta_0 \frac{\alpha_s}{4\pi} + \beta_1 \left(\frac{\alpha_s}{4\pi} \right)^2 + \beta_2 \left(\frac{\alpha_s}{4\pi} \right)^3 + \dots \right), \quad (1.4)$$

with $\beta_0 = 11 - \frac{2}{3}n_f$, where n_f is the number of active quark flavors at energy scale μ . For $n_f \leq 6$, the β_0 coefficient is positive, leading to a decrease in α_s at high energies (or equivalently, short distances) where strong interaction becomes weaker, allowing the use of perturbation theory (PT) in this regime. This behavior is known as asymptotic freedom,

²Antiquarks transform with the conjugate representation, so they could carry the opposite charge (antired, antigreen or antiblue)

³The spectrum of masses m_i span over five orders of magnitude ($m_u \approx 2.2 \text{ MeV}$, $m_t \approx 1.73 \times 10^5 \text{ MeV}$).

which essentially explains why quarks behave almost like free particles at high energies, enabling precise perturbative calculations in QCD. The discovery of asymptotic freedom is one of the most significant achievements in QCD, recognized by the 2004 Nobel Prize awarded to D. J. Gross, F. Wilczek, and H. D. Politzer [1, 2].

On the other hand, at low energies (toward $\Lambda_{\text{QCD}} \sim 200$ MeV), the coupling constant grows, leading to a non-perturbative behavior and a strong-coupling regime [1, 6]. This low-energy regime is characterized by confinement, where quarks and gluons are never observed as free particles but always exist in color-neutral bound states called hadrons [7]. Confinement is believed to be a consequence of the self-interaction of gluons, which leads to the formation of a strong, non-perturbative potential between quarks at large distances. Understanding the detailed mechanism of confinement, and providing a rigorous proof, remains an open question in theoretical physics [8, 9].

1.2 Non-Perturbative QCD and Effective Approaches

To study the non-perturbative regime of QCD, alternative approaches have been developed since PT becomes ineffective. Two of the most important methods are lattice QCD and effective field theories such as Chiral Perturbation Theory, and the large- N_c expansion.

Lattice QCD

An exact calculation from first principles based on the QCD Lagrangian (Eq. (1.1)) has been achieved only through Lattice QCD, a powerful numerical method developed by K. Wilson in the 70s [6]. This approach discretizes the QCD action on a four-dimensional Euclidean space-time lattice and perform Monte Carlo simulations to compute observables such as hadron masses, decay constants, and form factors [5, ch. 17]. Additionally, the Dyson-Schwinger equations offer a continuum, non-perturbative framework for quantum field theories, although they are typically solved with further approximations [10].

Despite the remarkable progress in Lattice QCD over recent years, certain observables remain inaccessible, and the method remains computationally expensive, often requiring careful guidance for extrapolations, especially in the presence of small quark masses or long-range interactions [5, ch. 17].

A complementary and analytically successful approach is Chiral Perturbation Theory, which serves as the low-energy effective field theory of QCD.

Chiral Perturbation Theory and Low-Energy QCD

Chiral Perturbation Theory (ChPT) is an effective field theory that describes the low-energy dynamics of QCD. It is based on the approximate chiral symmetry of QCD and its spontaneous breaking, resulting in pseudo-Goldstone bosons, which could be identified with the light mesons like pions, kaons, and eta [11–13]. In this framework, the low-energy regime can be described using a perturbative expansion in powers of momenta and quark masses.

The most general Lagrangian at leading order, reads [13–15]

$$\mathcal{L}_{\text{ChPT}} = \frac{f_\pi^2}{4} \text{Tr} \left[D_\mu U D^\mu U^\dagger \right] + \frac{f_\pi^2}{4} \text{Tr} \left[\chi U^\dagger + U \chi^\dagger \right], \quad (1.5)$$

where f_π is known as the pion decay constant in the chiral limit, U represents the matrix of pseudo-Goldstone bosons, and the covariant derivative is defined as:

$$D_\mu U = \partial_\mu U - i r_\mu U + i U l_\mu = \partial_\mu U - i [v_\mu, U] - i \{a_\mu, U\} \quad (1.6)$$

This derivative definition facilitates coupling pseudo-Goldstone bosons to external left-handed (l_μ) and right-handed (r_μ) currents, or alternatively to vector (v_μ) and axial (a_μ) currents. Finally, we have in the lagrangian, $\chi = 2B(s + ip)$, where B is tied to the quark condensate $\langle \bar{q}q \rangle_0$ in the chiral limit, with $s(p)$ representing external scalar (pseudoscalar) currents. This structure allow us introduce finite quark mass effects by setting $s \rightarrow \mathcal{M} = \text{diag}(m_u, m_d, m_s)$ [16, 17]. A more deeper and formal description of the ChPT can be found in references [12, 18].

ChPT provides systematic predictions for low-energy phenomena, such as pion-pion scattering and the modeling of pion form factors. Seminal works by Gasser and Leutwyler [13, 14] laid the foundation for these applications. The pion form factor, $F_\pi(q^2)$, is essential for understanding hadron structure and serves as a precision test of QCD, offering valuable insights into the strong interaction at low energies [19–22].

The Large N_c Limit and the Minimal Hadronic Approximation

The large N_c limit of QCD, introduced by 't Hooft, offers another perspective on the strong interaction [23]. In this limit, the number of colors N_c is treated as a large parameter, and QCD simplifies in certain respects. For instance, in the gluon self-energy computation, quark loops are suppressed⁴ by powers of $1/N_c$, and through this approximation the theory

⁴Strictly speaking, we refer to non-planar diagrams and quark loops.

becomes more tractable. This limit provides insight into the structure of mesons and baryons and helps explain some aspects of confinement and hadronization [24, 25].

The Minimal Hadronic Approximation (MHA) is a technique used within the large N_c framework to model hadronic physics [26]. It involves truncating the spectrum of hadronic states to the lightest few resonances, providing a simple yet effective way to compute certain QCD observables. The MHA has been applied successfully in areas like the calculation of form factors, decay constants, and contributions to the hadronic vacuum polarization [27–29].

The large- N_c approach, combined with techniques like Padé approximants (that we will explain in the next chapter), provides insight into the connection between low-energy chiral expansions and high-energy perturbative QCD results [26].

A deeper and detailed description for the large- N_c approximation can be found in references [25, 30, 31].

1.3 Challenges in QCD

During this thesis, we will explore various scenarios in particle physics where hadronic calculations play a crucial role, focusing on areas that are both highly active in current research and closely related to unresolved problems in QCD. Specifically, we will address topics such as the hadronic contributions to the anomalous magnetic moment of the muon and the importance of accurately modeling the form factors of B mesons for determining the transition probability of a bottom quark into an up quark.

QCD also plays a role in understanding CP violation⁵, which is explained within the SM by the complex phases in the Cabibbo-Kobayashi-Maskawa (CKM) matrix. This matrix encodes the mixing of quark flavors through weak interactions [32, 33]. Precise determinations of CKM elements are essential for constraining CP-violating processes in the strong sector [34]. Therefore, QCD plays an essential role in the analysis of these processes because the strong interactions contribute to the hadronic structure of meson decays and impact in the extraction of CKM matrix element associated (see Chapter 5). The interplay between QCD and weak interactions, especially in B-meson decays, provides key insights into CP-violating processes. In consequence, the precised determination of the CKM element V_{ub} provided by B-meson decays, has lead to stringent tests of the Standard Model and has opened the door to searches for new physics [35, 36].

⁵Charge Parity (CP) symmetry violation is essential for explaining the observed matter-antimatter asymmetry in the universe.

In the context of loop computations, QCD corrections are vital for many processes, including the determination of the anomalous magnetic moment of the muon, $(g - 2)_\mu$. The precise calculation of the hadronic contributions of $(g - 2)_\mu$ involves both perturbative and non-perturbative QCD [37–39]. These corrections are particularly challenging because they require a detailed understanding of hadronic vacuum polarization and hadronic light-by-light scattering, which are influenced by strong interactions at low energies [40, 41].

Recent discrepancies between the experimental and theoretical values for the $(g - 2)_\mu$ suggest effects of new physics beyond the Standard Model [42–44]. Several efforts have been made both theoretically and experimentally to obtain a better understanding of the QCD contributions to clarify this point (for a clear example of these efforts, see Chapter 4).

All these scenarios with hadronic processes are typically studied through a combination of lattice QCD, ChPT, the Large N_c limit expansion among other approaches.

1.4 Summary & highlights

Quantum Chromodynamics remains one of the most successful yet challenging components of the Standard Model. While the theory has explained a wide range of phenomena, from high-energy asymptotic freedom to low-energy hadron interactions, significant challenges remain. The precise determination of CKM matrix elements, the role of QCD in CP violation, and the understanding of confinement are central areas of ongoing research. Additionally, loop computations and contributions to the anomalous magnetic moment of the muon are pressing topics that rely on detailed QCD calculations. Effective theories like Chiral Perturbation Theory and large N_c techniques continue to play an essential role in bridging the gap between the non-perturbative nature of QCD and experimental observables. Therefore, it is necessary to propose other complementary techniques to address these challenges, such as those presented in this thesis.

Convergence Techniques and Padé Theory

Convergence Techniques essentially refers to a mathematical tool used to ensure that a series approaches a specific value or specific function as more terms of that series are added. These techniques are crucial in numerical analysis and in some applied fields like particle physics, where approximations are used to solve problems that cannot be addressed with exact solutions. In specific, we are interested in applying these type of techniques in order to obtain a good approximation for correlation functions that appear in QCD as well for Form Factors that could be characterised in terms of different poles within their domain.

To approximate a function, we would usually use its Taylor series, but only when the Taylor series expansion converges absolutely, then defines uniquely the value of a function which is differentiable an arbitrary number of times. However, this expansion presents some practical difficulties that include computing the Taylor coefficients and determining the range of applicability of the Taylor expansion.

On the other hand, when perturbation methods are used to solve a problem in QCD, the answer usually emerges as an infinite series. This perturbation series either has fast convergence, slow convergence or it is a divergent series, in the latter case we need a method that accelerates the convergence or assigns a relevant meaning to the sum even if only a few terms of the series are available. A divergent series is an indication of presence of singularities in the limit function, and a polynomial is not enabled to approximate the function in the whole convergence range, another motivation to find a suitable summation method.

Some example of acceleration methods include Euler, Borel Summation, Chebyshev

acceleration, continued fractions, among others [45, 46]. Each of these techniques are designed to enhance the range of convergence or make it possible to sum a divergent series or accelerate its convergence. However in the case of Euler and Borel summation all terms of the series must be known before apply the summation method, which is unrealistic, the common case is to have knowledge of the first few terms [47]. In this case, an excellent candidate to converge to the sum of the series or the function is the Padé Summation technique or Padé approximants, proposed by Henri Padé in his thesis in 1892 [48–50]. In the next section, we present the most relevant elements of Padé Theory.

This chapter is organized as follows: Section 2.1 will introduce the most relevant elements of Padé Theory and provide the formal definition of Padé approximants. It will cover an example of their canonical construction of Padé approximants in Subsection 2.1.1, convergence theorems for meromorphic functions in Subsection 2.1.2, and convergence for Stieltjes-type functions in Subsection 2.1.3. Finalizing Padé theory, we will explore extensions of Padé approximants in Subsection 2.1.4. A separate section will be dedicated to a variation that introduces a type of approximant which is not a rational function but employs the logarithmic derivative to construct approximants with a more complex analytical structure: the D-Log Padé approximants. This will be addressed in Section 2.2, where we will discuss their canonical construction with an example in Subsection 2.2.1, and potential extensions of this type of approximants in Subsection 2.2.2.

2.1 Padé approximants

Since the notion of Padé approximants has already been introduced, a more detailed and rigorous description will be presented in this section. Given a function $f(z)$ of complex variable z with a well defined power expansion around the origin¹ with a certain radius of convergence $|z|=R$

$$f(z) = \sum_{n=0}^{\infty} f_n z^n, \quad (2.1)$$

a Padé approximant (PA) for the function $f(z)$ can be defined as a ratio of two polynomials in the variable z . The polynomial $A_N(z)$ with N as the highest degree in the numerator and the polynomial $B_M(z)$ with M as the highest degree in the denominator. This rational function can be denoted as $P_M^N(z)$ ²,

¹The definition is not special for the origin ($z=0$) and generally applies to any point z_0 in the complex plane as long as the series expansion is well-defined around $z=z_0$.

²In the mathematical literature $P_M^N(z)$ is often referred to as $[N/M]$ or $[N|M]$

$$P_M^N(z) = \frac{A_N(z)}{B_M(z)} = \frac{\sum_{n=0}^N a_n z^n}{\sum_{m=0}^M b_m z^m}, \quad (2.2)$$

where coefficients a_n, b_m can be determined using the following relation:

$$|f(z) - P_M^N(z)| = \mathcal{O}(z^{N+M+1}), \quad (2.3)$$

therefore, when expanding $P_M^N(z)$ around $z = 0$, the first $M + N + 1$ coefficients of the expansion for $f(z)$ (Eq. 2.1) are exactly reproduced. Since the fractional values of each power remain invariant if both polynomials (A_N, B_M) are multiplied by a non-zero constant, we can define a standard normalization using $b_0 = 1$ without loss of generality.

A Padé approximant could generate different sequences of approximants that can ensure the convergence to the original function, therefore those of spacial interest are the near-diagonal sequences when $N = M + J$, for a fixed J . In particular, it will be very useful to us the diagonal ($J = 0$), subdiagonal ($J = -1$) and superdiagonal sequence ($J = 1$).

A more extended theoretical description can be found in references [16, 47, 51–53], and more recent developments in numerical analysis and classical analysis that involve Padé approximants as a very useful and versatile tool can be found in references [54–57].

2.1.1 Canonical construction of a Padé approximant

In order to observe how is the behaviour of PAs when the method is applied to divergent series, let us to consider the following function

$$f(z) = \frac{\ln(z+1)}{z} \left(\frac{z-2}{\sqrt{z+5}} \right). \quad (2.4)$$

This function has one branch point located in $z = -1$, and one branch cut in $z = -5$, thus, the real domain for this function is $(-1, \infty)$. The function also has a zero in $z = 2$ and lastly a pole in zero which cancels with logarithm function. PAs have the ability to converge to the function beyond the radius of convergence of the corresponding power series for the function $f(z)$ as shown in Figure 2.1. In the same figure, can be noted that increasing the order of the PA, the approximant converges to the original function even when the series diverges. In this case, the convergence is so fast that we need to zoom into the range $(-1, 1)$ of $f(z)$ to distinguish between the first Padé sequences, as shown in Figure 2.1(b). Additionally, it's worth noting that there is no significant improvement between P_2^2 and P_3^3 , which could be attributed to a type of noise that occasionally affects some PAs, known

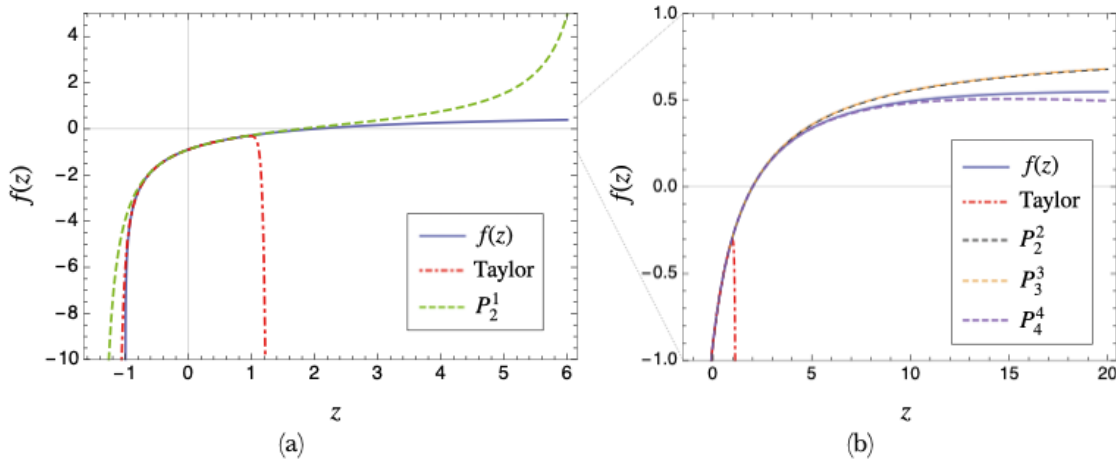


Figure 2.1: Convergence behaviour of different PAs, where solid blue line corresponds to the example function, dot-dashed red line is the truncated Taylor Series and all dashed lines are Padé approximants considered.

as *defects*³, essentially they are regions of the complex plane that have a pole and a near by zero, but their effect is limited to an area around the pole and not the entire complex plane. Their proximity can be so high that they practically cancel each other out reducing the order of the approximant by one unit in its sequence.

Another notable behavior of PAs is their ability to "reproduce" a branch point or a branch cut of the original function by accumulating zeros and poles along the real negative axis⁴. As the order of the PA increases, the density of these zeros and poles around the singularity also increases and in some sense the PA resemble the branch cut, as it is formally proven in [47, 60, 61]. This behavior around the first branch point ($z = -1$) of the example function is shown in Figure 2.2. However, identifying the precise location of the cut using this trend requires a large number of coefficients. Moreover, the potential appearance of aforementioned "defect-pairs" very close to the cut location complicates this process, as it becomes difficult to determine whether they are part of the trend or not. This could lead to an incorrect identification of the cut's position, as seen with the PA P_6^6 , which has a defect at $z = -0.937$. Other defects are presented in the third column of Figure 2.2. Additionally, the same figure shows that the zero at $z = 2$ is obtained with high precision from lower-order PAs ($\sim P_2^2$).

³Defects are also known as *Froissart doublets*, since this effect was observed by Marcel Froissart in the 60's [58, 59].

⁴In a rigorous way, diagonal and subdiagonal PAs converge for all z in the cut-plane ($|\arg z| < \pi$) [47, 51]

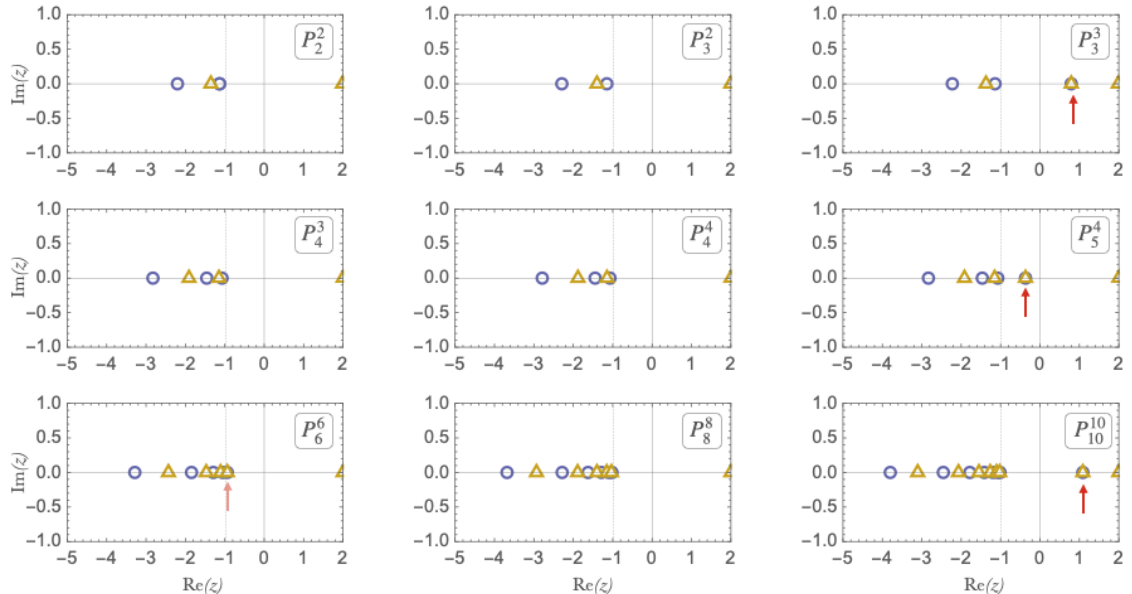


Figure 2.2: Accumulation of poles (blue circles) and zeros (yellow triangles) towards the cut $z = -1$ of example function (Eq. (2.4)) in the domain $-5 < \text{Re}(z) < 2$, using 9 different PAs. *Defect* pairs are indicated with a red arrow.

2.1.2 Convergence for meromorphic functions

As shown above PAs become a powerful tool when we are dealing with divergent series, they cannot only dramatically improve the convergence rate within $|z| < R$ with respect to Eq. (2.1), but may provide convergence in a larger domain. However, since many functions can be asymptotic to the same divergent series, the issue arises of identifying the limit function to which a PA sequence converges. While there is no general theory for Padé summation applicable to arbitrary series, the convergence theory of Padé approximants is relatively well-known for specific classes, including Stieltjes series, meromorphic functions, continued fractions, hypergeometric functions, and Bessel functions [47, 51].

In this section, we will describe the convergence properties for meromorphic functions, while Stieltjes functions convergence will be presented in the next section (see 2.1.3), these type of functions are of our interest because are representative cases of QCD Green's functions.

A meromorphic function could be defined as a function which is analytic in the whole complex plane except for a set of isolated poles. The convergence properties of PAs to this kind of functions are very well-known and can be summarized in terms of Montessus' and Pommerenke's theorems [47, 52].

Montessus's theorem

Let $f(z)$ be a meromorphic function inside the disk $|z| \leq R$ with m multiple poles (z_1, z_2, \dots, z_m) located in different positions according to the following hierarchy:

$$0 \leq |z_1| \leq |z_2| \leq \dots \leq |z_m| \leq R \quad (2.5)$$

Considering that, a multiple pole z_k could have multiplicity ν_k (where $\nu_k \in \mathbb{N}$), then we can set the total multiplicity as $\sum_{k=1}^m \nu_k = M$. Then we have,

$$f(z) = \lim_{L \rightarrow \infty} P_M^L(z), \quad (2.6)$$

uniformly on any compact subset of

$$\mathfrak{D}_m = \{z \mid |z| \leq R, z \neq z_k, k = 1, 2, \dots, m\}. \quad (2.7)$$

Montessus's theorem guarantees the Padé sequence convergence within the circle $|z| < R$, ensuring that the poles and residues of the PAs converge to their true values as $L \rightarrow \infty$ [62] [52, ch. 6.2]. This uniform convergence implies no spurious poles will appear within this disk, and the positions of the m poles will be accurately determined (as an example of its application see Refs. [20, 63–65]). However, the theorem says nothing about the region outside the circle $|z| < R$, and the number of poles must be known in advance, Pommerenke's theorem can be considered as an alternative.

Pommerenke's theorem

Pommerenke's theorem states the following; let $f(z)$ be an analytic function at the origin as well as in the entire complex plane except for a countable number of isolated poles and/or essential singularities, then the sequence of PAs P_M^L where $L = \lambda M$ (with $\lambda \neq 0$ and $\lambda \neq \infty$) satisfies:

$$f(z) = \lim_{M \rightarrow \infty} P_M^{\lambda M}, \quad (2.8)$$

on any compact set of the z -plane except for a set of points of zero measure⁵ [66].

This theorem guarantees that, in any compact region of the complex plane, the spurious poles of this type of sequences will either move away from this area as the order of the PA

⁵It means that convergence is not guaranteed when $|f(z) - P_M^{\lambda M}| \leq \varepsilon$ is no longer valid on an arbitrarily small circle around this point.

increases or will appear in pairs near the zeros of the function, producing the aforementioned *defects*. An interesting corollary of this theorem, as mentioned in Ref. [52], extends this guarantee to PAs sequences P_N^{N+k} for a fixed k , ensuring convergence as $N \rightarrow \infty$.

The theorem has three very relevant benefits: first, the poles don't have to be specified in advance; second, it ensures convergence practically in the entire complex plane; third, it accounts for not just poles but also essential singularities. However, a challenging situation arises when one has to deal with these unwanted poles –poles which are not part of the original function–. Additionally, increasing the order of the Padé sequence P_N^{N+k} by one requires two new coefficients as input parameters, while Montessus' theorem only needs one new coefficient to increase the order of its sequence. For a nice illustration of this property and the use of Pommerenke's theorem, we refer to [64, 67].

2.1.3 Convergence for Stieltjes functions

In this chapter, we will present the Stieltjes functions, exploring their fundamental properties and its proper definition. We will discuss how the convergence of Padé approximants can be reliably ensured for these types of functions, an essential aspect in later chapters since their analytical properties can be guaranteed for some Green's functions (correlators) in QCD. Through this exploration, we aim to provide a powerful tool to parameterize different functions that satisfy the Stieltjes structure, thereby ensuring important convergence behavior. Additionally, this approach can offer an uncertainty value between the original function and the approximant.

Stieltjes functions

A Stieltjes function is a function that can be represented by a Stieltjes integral

$$f(z) = \int_0^\infty \frac{d\phi(u)}{1+zu}, \quad |\arg(z)| < \pi. \quad (2.9)$$

where $\phi(u)$ is a bounded non-decreasing function on the interval $0 \leq u < \infty$ with finite positive moments given by

$$f_n = \int_0^\infty u^n d\phi(u), \quad \forall n \geq 0. \quad (2.10)$$

Since moments f_n correspond to a measure $\phi(u)$ inside the interval $[0, \infty)$, then $f(z)$ can be expressed with its expansion in power series, called Stieltjes series⁶,

$$f(z) = \sum_{n=0}^{\infty} f_n (-z)^n. \quad (2.11)$$

A necessary and sufficient condition [52] for a function to be Stieltjes is that all the Hankell determinants $\mathcal{D}_{m,n}^f$ with $m \geq 0$ and $n \geq 0$ must be strictly positive⁷.

$$\mathcal{D}_{m,n}^f = \begin{vmatrix} f_m & f_{m+1} & \cdots & f_{m+n} \\ f_{m+1} & f_{m+2} & \cdots & f_{m+n+1} \\ \vdots & \vdots & \ddots & \vdots \\ f_{m+n} & f_{m+n+1} & \cdots & f_{m+2n} \end{vmatrix} > 0. \quad (2.12)$$

These determinants produce constraints between the power series coefficients f_n of the Stieltjes functions. This will be essential in our analysis in later chapters since a PA constructed from a Stieltjes function has the same Stieltjes properties as the original function has [51, 52].

The function in Eq. (2.4) is a not Stieltjes type function. However, it will be easy to prove that the factor $\frac{\ln(z+1)}{z}$ can be represented as a Stieltjes function with the interest of giving an example. The series expansion for $\ln(z+1)$ reads:

$$\ln(1+z) = \sum_{n=1}^{\infty} \frac{(-1)^{n-1} z^n}{n} \rightarrow \sum_{n=0}^{\infty} \frac{(-1)^n z^{n+1}}{n+1} \rightarrow z \sum_{n=0}^{\infty} \frac{(-z)^n}{n+1}, \quad |z| < 1. \quad (2.13)$$

That series diverge for $|z| > 1$, however, it can be summed as long as $|\arg(z)| < \pi$ using PAs for Stieltjes series. Dividing by z in both sides, we can note it is already in Stieltjes series representation (Eq. (2.11)), where moments satisfy

$$f_n = \frac{1}{n+1}. \quad (2.14)$$

It can be easily shown that

$$f_n = \int_0^{\infty} u^n d\phi(u) = \int_0^1 u^n du = \frac{1}{n+1}, \quad (2.15)$$

⁶it would be easier to use the positive-definite coefficients (f_n) in Eq. (2.11) rather than the standard notation for a power series due the resultant conditions in the Hankel determinants (Eq. (2.12))

⁷In some references, the condition is described as non-negative; however, in the case of all Hankel determinants being zero, this results in a trivial case, specifically corresponding to the PA P_1^0

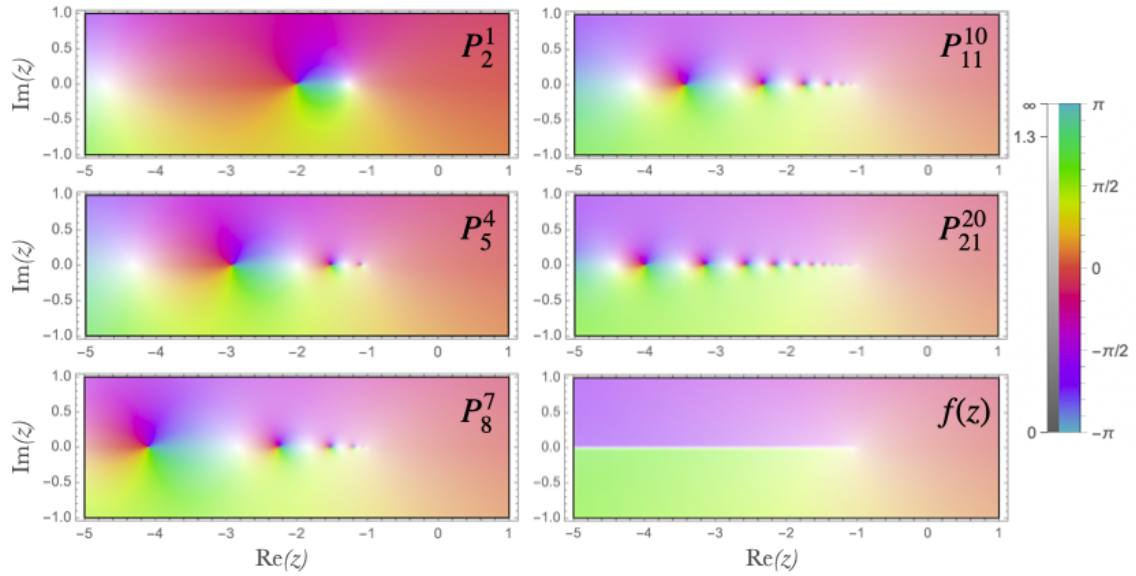


Figure 2.3: Representation of poles (white points) and zeros (black points) using 5 different PAs of sequence P_N^{N-1} to approximate the Stieltjes function $f(z) = z^{-1} \ln(z+1)$.

where we only have to define $\phi(u) = u$ for $0 \leq u \leq 1$ and $\phi(u) = 1$ for $1 < u$, therefore we get the following Stieltjes function

$$\ln(z+1) = z \int_0^1 \frac{du}{1+zu}.$$

Recall the ability of the PAs to resemble a branch cut by increasing their order, which results in the accumulation of poles and zeros. In this case, these poles and zeros cluster near $z = -1$, all located on the negative real axis, as illustrated in Fig. 2.3. This behavior is a direct consequence of the guaranteed convergence within the cut plane ($|\arg(z)| < \pi$), a topic we will discuss in more detail in the next subsection.

Convergence properties

For functions that belong to the Stieltjes type functions, a well-established theorem based in the Carleman condition within the theory of Padé approximants ensures the convergence of the $P_N^{N+J}(z)$ sequence in the cut complex plane for $J \geq -1$ when $N \rightarrow \infty$ [47, 51, 52, 68, 69].

The Padé sequence of a Stieltjes series representation exhibits notable convergence properties when its weight function is nonnegative. It can be proved that, for $z > 0$:

- The diagonal Padé sequence $P_N^N(z)$ decreases monotonically as N increases.

- The subdiagonal Padé sequence $P_{N+1}^N(z)$ increases monotonically as N increases. This also applies for superdiagonal sequence $P_N^{N+1}(z)$.
- The sequence $P_N^N(z)$ has a lower bound, while the sequence $P_{N+1}^N(z)$ or $P_N^{N+1}(z)$ has an upper bound.

These properties imply; first, $\lim_{N \rightarrow \infty} P_N^N(z)$ and $\lim_{N \rightarrow \infty} P_{N+1}^N(z)$ both exist for real positive z ; secondly, $\lim_{N \rightarrow \infty} P_{N+1}^N(z) \leq \lim_{N \rightarrow \infty} P_N^N(z)$. In the case we have the equality then there is just one Stieltjes function corresponding to the limit function of the approximants. Even more, all Stieltjes functions $f(z)$ with the same finite series representation used in the Padé summation satisfy

$$\lim_{N \rightarrow \infty} P_{N+1}^N(z) \leq f(z) \leq \lim_{N \rightarrow \infty} P_N^N(z), \quad (2.16)$$

these previous inequalities can be generalized in the following way: for any $J \geq -1$ the Padé sequence $P_N^{N+J}(z)$ generated from a Stieltjes function is monotonically increasing when J is odd and monotonically decreasing when J is even⁸. This generalization directly implies the equivalent convergence relation for the superdiagonal sequence as follows

$$\lim_{N \rightarrow \infty} P_N^{N+1}(z) \leq f(z) \leq \lim_{N \rightarrow \infty} P_N^N(z). \quad (2.17)$$

Moreover, since diagonal and near-diagonal Padé sequences $P_N^N(z)$ and $P_{N \pm 1}^N(z)$ converge to the original function, and this Stieltjes functions is analytic in the cut- z plane, we can ensure that above mentioned PAs satisfy Stieljes properties and are also analytic in the cut complex plane $|\arg z| < \pi$, hence all their poles must be located on the negative real axis, excluding the possibility of defects in the range of convergence. This is very useful because allow us to reconstruct some hadronic functions, like the vacuum polarization, in the whole cut complex plane as we will see in Chapter 4.

When dealing with functions that are both Stieltjes and meromorphic, choosing the appropriate convergence theorem depends on the specific needs of the analysis. Montessus' theorem guarantees uniform convergence within a disk, while the Stieltjes-convergence theorem provides boundary constraints for the approximation. For meromorphic functions that are not Stieltjes, Montessus' theorem does not offer boundary constraints, so the accuracy of the Padé sequence is typically assessed by examining the differences between consecutive approximants, like following references [61, 64, 67, 70].

⁸The behaviour of convergence is not guarantee for the P_1^N sequence as one can prove they do not need to be Stieltjes even though they are built from a Stieltjes function [52].

2.1.4 Extensions of Padé approximants

So far, we have discussed Padé approximants without prior knowledge of the poles, but it can be beneficial to include information about certain resonances and positions further from the origin. Montessus's and Pommerenke's theorems suggest that the poles and residues of the underlying function are eventually reproduced by the approximants. Incorporating this information before their construction, when this is known, can enhance accuracy. This can be achieved through Padé type and partial Padé approximants, which allow the incorporation of known pole positions, such as the lowest states in QCD Green's functions.

Partial Padé approximants

Knowing the positions of the poles $z = z_1, z_2, \dots, z_K$ of the original function, at least those nearest to the origin, lets us use this information in a straightforward way with the Partial Padé approximants (PPAs), defined as

$$\mathbb{P}_{M,K}^N(z) = \frac{Q_N(z)}{R_M(z)T_K(z)}, \quad (2.18)$$

where $Q_N(z)$, $R_M(z)$ and $T_K(z)$ are polynomials of order N , M and K (respectively) in the variable z . What is interesting here is that the polynomial $T_K(z)$ is defined by having K zeros precisely at the location of the first K -poles of the original function⁹

$$T_K(z) = (z - z_1)(z - z_2) \cdots (z - z_K). \quad (2.19)$$

The approximant is generated in the same way as for the usual PAs, matching exactly the first $M + N + 1$ terms in the expansion around $z = 0$, and taking $R_M(0) = 1$

$$|f(z) - \mathbb{P}_{M,K}^N(z)| = \mathcal{O}(z^{N+M+1}). \quad (2.20)$$

As occurs with PAs, it is also possible to obtain *defects* in the PPAs for general meromorphic functions.

Padé Type approximants

Padé Type approximants (PTAs) is another kind of rational approximant, defined by:

$$\mathbb{T}_M^N(z) = \frac{Q_N(z)}{T_M(z)} \quad (2.21)$$

⁹We can consider for simplicity that the zeros of T_K are of multiplicity 1.

where $T_M(z)$ is also given by the polynomial in Eq. (2.19). But in this case, all the M poles of the approximant are fixed in advance to the lowest-lying poles of the original function, and just the polynomial $Q_N(z)$ of order N can increase the order so that the approximant matches the first $M + 1$ terms of the expansion of function $f(z)$,

$$|f(z) - \mathbb{T}_M^N(z)| = \mathcal{O}(z^{M+1}). \quad (2.22)$$

As can be noted, $\mathbb{T}_M^N(z)$ is a special case of PPAs where $\mathbb{T}_M^N(z) = \mathbb{P}_{0,M}^N(z)$ ¹⁰. Since all the poles of the approximant are already fixed no *defects* will appear in the PTAs. It is important to remark that Padé Type sequence converge to the limit function only when both $M, N \rightarrow \infty$.

2.2 D-log Padé approximants

In the field of Classical and Numerical Analysis, particularly within approximation methods, effectively approximating functions with branch points and branch cuts remains a significant challenge [76]. The D-Log Padé approximants, which has been rigorously studied in this thesis, provide a promising approach to overcoming this difficulty.

Before going into a more formal description, the basic concept of D-Log Padé approximants (D-Logs from now) involve manipulating a function with one or more branch cuts in the complex plane into a format that is more amenable to Padé approximation¹¹. By addressing the logarithmic derivative (hence its notation as D-Log), the method simplifies the approximation process, allowing for a more accurate representation of the original function's behavior near its singularities. This occurs because, after taking the logarithmic derivative, a branch cut is transformed into a simple pole. The residue of this pole provides information about the multiplicity of the cut. Similarly, this method can be used to reproduce the analytical structure of any branch point [52, Sec. 2.2].

Since a D-Log requires only two coefficients to get the branch cut information, it can often achieve faster convergence compared to Padé approximants, which rely on an infinite succession of poles and zeros to determine the location of the cut and definitely cannot provide information about its multiplicity.

¹⁰This kind of approximants coincide with what has been called the Hadronic Approximation to large- N_c QCD in the literature [71–75]

¹¹The concept of using Padé approximants to the logarithmic derivative of a function to extract information about its singularities was first introduced by G.A. Baker in 1961 while investigating certain magnetic properties of the Ising model [77]. Other relevant works that introduced this concept are presented in the references [78–80].

It is important to note that D-Log approximants are not rational functions like PAs; rather, they represent a distinct type of approximant. This distinction is crucial because it highlights the unique ability of D-Logs to handle singularities with non-integer multiplicities. This capability allows the approximation to extend into the complex plane and provides access to the imaginary part of the original function –something that is not possible with PAs constructed from real Taylor coefficients–.

Recent and relevant studies where D-logs have already been used can be found in references [81–84].

Now, for a formal definition, let us consider we are interested in the following function

$$f(z) = f_1(z) \frac{1}{(\mu - z)^\gamma} + f_2(z), \quad (2.23)$$

where $f_1(z)$ and $f_2(z)$ are functions with little structure and analytic at $z = \mu$. We are primarily interested in the case in which $f(z)$ has a branch point at $z = \mu$ and, accordingly, γ is a non-integer number, but in reality, this condition is not essential for what follows. Instead of working directly with $f(z)$, we will use a new function $F(z)$ near $z = \mu$ as [52]

$$F(z) = \frac{d}{dz} \ln f(z) = \frac{\gamma f_1(\mu - z)^{-(\gamma+1)} + f_1'(\mu - z)^{-\gamma} + f_2'}{f_1(\mu - z)^{-\gamma} + f_2} \quad (2.24)$$

$$= \left(\frac{\gamma}{(\mu - z)} + \frac{f_1'}{f_1} + \frac{f_2'}{f_1} (\mu - z)^\gamma \right) \left[\frac{1}{1 + \frac{f_2}{f_1} (\mu - z)^\gamma} \right] \quad (2.25)$$

$$F(z) \approx \frac{\gamma}{(\mu - z)} + \frac{f_1'}{f_1}. \quad (2.26)$$

Since we are looking the function near $z = \mu$, the right factor in Eq. (2.25) goes to 1 and the third term of left factor goes to zero. As you can see in Eq. (2.26), the exponent of the branch cut γ is now the residue of the simple pole μ of $F(z)$ –even if γ is not an integer–, which can be determined using a Padé sequence to $F(z)$ ¹², denoted here as $\bar{P}_M^N(z)$. By reversing this process, the original function $f(z)$ can be approximated by a non-rational function known as the D-Log Padé approximant; $\text{Dlog}_M^N(z)$ or simply $D_M^N(z)$ approximant, given by the expression below [52, 83, 84]

¹²It is safe to say that the function $F(z)$ is meromorphic in a vicinity of $z = \mu$, so the convergence theorems of Section 2.1.2 can be applied under this condition.

$$\text{Dlog}_M^N(z) = f(0) \exp \left\{ \left[\int dz \bar{P}_M^N(z) \right] \right\}. \quad (2.27)$$

Because of the derivative in Eq. (2.26), the $f(0)$ term is lost and must be reintroduced to correctly normalize the D-Log. The Dlog_M^N then reproduces exactly the first $M + N + 2$ coefficients of $f(z)$ (one order more than the usual P_M^N) and can be used to predict the $(M + N + 3)$ -th coefficient and higher.

In principle, this type of approximant offers a way to determine the branch point and the exponent of the cut of the original function $f(z)$ from the study of the PA to $F(z)$ around its pole. Since no assumption about μ or γ is made, their estimates are exclusively obtained from the series coefficients, so we can consider it as an unbiased estimate.

In practice, the D-Log approximant $D_M^N(z)$ can yield a rich analytical structure, in particular the presence of several branch cuts is to be expected. If the function $f(z)$ has a branch cut, the D-Log will extract its location and multiplicity ever more accurately as both $M, N \rightarrow \infty$, even more, all the singularities of $f(z)$ would be located. However, not all singularities generated by a D-Log approximant necessarily correspond to branch points or cuts in the original function $f(z)$. These "extra" singularities aim to replicate the analytical structure across the entire complex plane, they often have a very small multiplicity which represents a very small contribution in their first two terms of its Taylor expansion. Finally, they don't exhibit any consistent pattern as N and M increase.

2.2.1 Canonical construction of D-Logs

As an example of how to construct the D-log approximant and see how it behaves, we will consider again the example used in the case of the PAs, Eq. (2.4).

1. As a first step, we get the logarithm derivative:

$$F(z) = \frac{d}{dz} \ln \left[\frac{\ln(z+1)}{z} \left(\frac{z-2}{\sqrt{z+5}} \right) \right] \quad (2.28)$$

$$F(z) = \frac{1}{\ln(z+1)(z+1)} - \frac{1}{z} + \frac{1}{(z-2)} - \frac{1}{2(z+5)} \quad (2.29)$$

2. secondly, we will take the diagonal sequence P_N^N apply to the resultant function:

$$\begin{aligned}
P_1^1[F(z)] &= \frac{-1.1 - 2.78x}{1 + 2.7x} \\
P_2^2[F(z)] &= \frac{-1.1 - 0.237x + 0.115x^2}{1 + 0.385x - 0.498x^2} \\
P_3^3[F(z)] &= \frac{-1.1 - 0.830x - 0.031x^2 + 0.015x^3}{1 + 0.924x - 0.273x^2 - 0.223x^3} \\
P_4^4[F(z)] &= \frac{-1.1 - 1.426x - 0.415x^2 + 0.013x^3 + 0.001x^4}{1 + 1.466x + 0.168x^2 - 0.394x^3 - 0.091x^4} \\
&\vdots
\end{aligned}$$

3. unfolding the process to get the D-Log approximant, we apply Eq. (2.27)

$$\begin{aligned}
D_2^2 &= \frac{-0.57 e^{-0.232x} (1.85608 - x)^{0.78105}}{(x + 1.0826)^{0.4845}} \\
D_3^3 &= \frac{-0.62 e^{-0.068x} (1.99065 - x)^{0.98000}}{(x + 1.0321)^{0.3775} (x + 2.1851)^{0.3801}} \\
D_4^4 &= \frac{-1.06 e^{-0.014x} (1.99965 - x)^{0.99906}}{(x + 1.0152)^{0.3173} (x + 1.3731)^{0.1714} (x + 3.9485)^{0.5880}} \\
D_5^5 &= \frac{-1.37 e^{-0.004x} (1.99999 - x)^{0.99996}}{(x + 1.0087)^{0.2823} (x + 1.2046)^{0.1347} (x + 1.8343)^{0.1304} (x + 4.8322)^{0.6440}} \\
D_6^6 &= \frac{-1.47 e^{-0.002x} (2 - x)^{1.0}}{(x + 1.0058)^{0.261} (x + 1.14)^{0.117} (x + 1.51)^{0.108} (x + 2.52)^{0.118} (x + 5.2513)^{0.616}} \\
&\vdots
\end{aligned}$$

As shown in previous equations and Table 2.1, the branch point closest to the origin, $z = -1$, which corresponds to the logarithmic term in Eq. (2.4), can be effectively reproduced by the second D-Log in the sequence, D_N^N . This approximation achieves a precision comparable to the Padé approximant P_4^3 , indicating that this D-Log requires two fewer degrees of freedom to attain the same accuracy for locating this branch point. Furthermore, the multiplicity of this singularity becomes smoother as we rise through the Padé sequence, which aligns with the behavior expected for a logarithmic function, which doesn't have a well-defined multiplicity.

In the case of the branch cut at $z = -5$, its location is not directly identified by the initial approximants. In deed, a reliable estimate with sufficient precision is only obtained starting from D_5^5 . This can be explained by the fact that the D-Logs are constructed around the origin, and their convergence extends further into the domain as the order of the D-Logs

increases. However, a clear convergence pattern can be observed in Table 2.1, suggesting a possible branch cut at $z = -5$ with a multiplicity of approximately 0.61 (compared with the true value: 0.5). This result represents a significant improvement over PAs, as they fail to provide any information about a potential cut at $z = -5$; not even a pole is detected at this location, at least not within the first 10 approximants of the P_N^N sequence.

On the other hand, the zero at $z = 2$ is quickly identified by the PAs starting from P_2^2 (see Fig. 2.2). For D-Logs, the same precision for this singularity is achieved with D_3^3 . Higher orders of D-Logs provide even greater accuracy for both the zero's location and its multiplicity. In summary, all singularities of the example function can be identified with a good approximation for their locations and corresponding multiplicities from D_5^4 . Any branch cuts that appear in higher-order D-Logs but are not present in the original function have very small exponents (< 0.15) and decrease as N increases. This behavior is expected, as the Taylor expansion around zero for these terms contributes minimally: $(\mu + x)^\epsilon \approx 1 + \frac{\epsilon}{\mu}x + \mathcal{O}(\epsilon^2 x^2)$.

Table 2.1: Singularities reproduction of Eq. (2.4) using D-Logs sequences D_N^{N-1} and D_N^N , where μ_k is the location and γ_k is the multiplicity

	μ_1	γ_1	μ_2	γ_2	μ_3	γ_3
$f(z)$	-1	-	2	1	-5	0.5
D_2^1	-1.1496	0.5901	2.2546	1.3222	-	-
D_2^2	-1.0826	0.4845	1.8561	0.7811	-	-
D_3^2	-1.0424	0.4030	2.0131	1.0228	-3.0284	0.6201
D_3^3	-1.0321	0.3775	1.9907	0.9800	-2.1851	0.3801
D_4^3	-1.0184	0.3300	2.0005	1.0011	-4.6735	0.6991
D_4^4	-1.0152	0.3173	1.9997	0.9991	-3.9485	0.5880
D_5^4	-1.0108	0.2900	2.0000	1.0001	-5.4301	0.6549
D_5^5	-1.0087	0.2823	2.0000	1.0000	-4.8322	0.6440
D_6^6	-1.0058	0.2611	2.0000	1.0000	-5.2513	0.6155

In Fig. 2.4 we can compare the analytical behaviour of the original function and the approximant D_6^6 . As we can see the D-Logs try to reproduce not only the real part of the function, also the imaginary part with successive cuts as increase the order. This is precisely where the success of the D-log approximation for a function in the complex plane comes from. This feature represents a significant advantage since PAs built from a Taylor series around the origin cannot access to the imaginary part of the function, above the

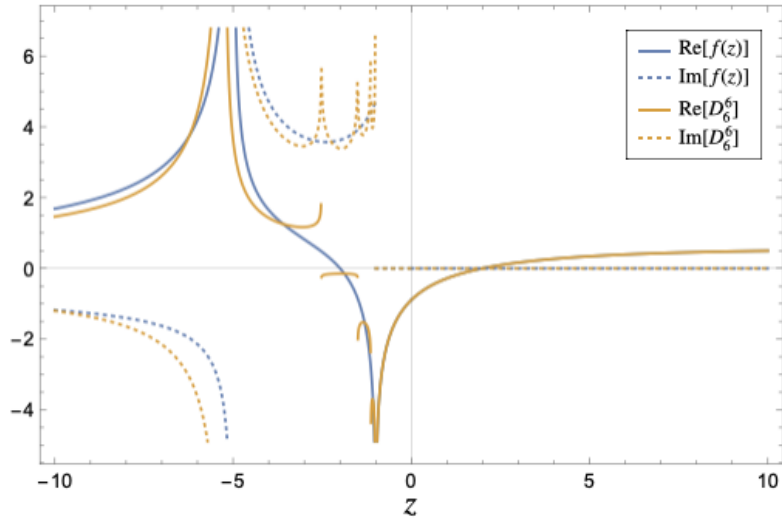


Figure 2.4: approximant D_6^6 behaviour in comparative with example function Eq. (2.4), where dotted line is the imaginary part and solid line is the real part of the complex function $f(z)$.

branch cut, but D-Logs can.

A comparative and detailed analysis of convergence between PAs and D-Logs will be shown later in Chapters 4 and 5 where PAs and D-Logs will be used in a very active field of research in a context of QCD.

2.2.2 Extensions of D-Log approximants

In cases where the branch point or the location of the singularity is known in advance, one can construct a variant of a D-Log approximant. Taking $(\nu - z)^\beta$, where ν is the notation now for branch cuts location that we already know, the corresponding multiplicity β can be found using the following expression:

$$G(z) = (\nu - z) \frac{d}{dz} \ln [(f(z))] \sim \beta, \quad (2.30)$$

where approximation to function $G(z)$ could provide us a biased estimate of β . We can then use a PPA $\mathbb{P}_{M,1}^N$ to approximate $\tilde{G}(z) = G(z)/(\nu - z)$ and thereby get an approximation for $f(z)$:

$$f(z) \approx f(0) \exp \left\{ \left[\int dz \mathbb{P}_{M,1}^N[\tilde{G}(z)] \right] \right\} \quad (2.31)$$

The above method can be generalized if more singularities are known, i.e. $\nu_i \mid \{i = 1, 2, \dots, K\}$. In that case we can use what we define as a Partial D-Log $\mathbb{PD}_{M,K}^N$:

$$\mathbb{PD}_{M,K}^N[f(z)] = f(0) \exp \left\{ \left[\int dz \mathbb{P}_{M,K}^N[\tilde{G}(z)] \right] \right\} \quad (2.32)$$

If both the location and the multiplicity of the singularities are known, we can use an alternative form of Partial D-Logs defining $H(z) = \frac{d}{dz} \ln [(f(z)) \prod_i (\nu_i - z)^{-\beta_i}]$ and using the following expression:

$$\widetilde{\mathbb{PD}}_{M,K}^N[f(z)] = f(0) \exp \left\{ \left[\int dz \left(\sum_i^K \frac{\beta_i}{(\nu_i - z)} + P_M^N[H(z)] \right) \right] \right\} \quad (2.33)$$

where a pattern of convergence can be observed for $N \geq M + K - 1$. An example of this type of approximant will be shown in Chapters 4 and 5.

2.3 Recap of convergence techniques

Padé approximants (PAs) provide excellent convergence, even across an extended range in the domain compared to Taylor expansions. They can be considered a completely model-independent method since all poles are left free. However, they may require a large number of coefficients to achieve sufficient precision in convergence. This can be improved by incorporating external information about the singularities of the original function and applying Partial Padé approximants (PPAs) or Padé-Type approximants (PTAs) instead of PAs.

Other interesting and promising technique are the D-Log Padé approximants, as they can reproduce multipoles, branch points, and branch cuts using less coefficients than PAs. D-Logs have a richer analytical structure that allows them to extend the approximation to the imaginary part of the original function. However, a disadvantage of D-Logs is the loss of the original function's scale in the derivative, and there are no convergence theorems that apply directly to D-Logs. If we have knowledge of a singularity and its multiplicity, Partial D-Logs can be employed, but this approach is no longer unbiased.

Ultimately, for each case of interest, the researcher must determine the best strategy. As we will demonstrate in the following chapters (Ch. 4, 5), a sequential study using the various aforementioned approximations is the optimal way to extract information about unknown Taylor coefficients or the singular structure of the target function.

These techniques will be particularly useful when the approximants are employed to

fit data to a function that may be meromorphic or of Stieltjes type. This is because we can impose additional constraints during the fitting process based on the analytical properties of the fitting functions, while still maintaining a model-independent approach. PAs have been widely used as fitting functions in various studies within the context of QCD, where the convergence theorems appear to be satisfied [20, 40, 85–88]. Recent studies have also employed D-Logs as fitting functions, demonstrating convergence in these cases as well [81–84].

About convergence in D-Log Padé approximants

As we mention before, there are no known convergence theorems in the literature that can be directly applied to D-Log type functions. This is precisely, the main drawback of this type of approximants. In order to identify a convergence pattern, we must ensure that the ratio f'/f exhibits a meromorphic or Stieltjes-type analytic structure. Furthermore, this structure must also be preserved in the original function f , which is not always straightforward to demonstrate or generalize. In the following sections, we will examine the convergence properties in cases where the logarithmic derivative results in a function $F(z)$ displaying meromorphic behavior (see Section 3.1). Additionally, we will propose a conjecture on convergence for Stieltjes-type functions in Section 3.2.

3.1 Convergence for the Taylor expansion

While it is not possible to directly discuss convergence for the original function, we can instead consider its Taylor series expansion around the origin and apply the logarithmic derivative. In this context, we assume the function $F(z)$ to be meromorphic within the radius of convergence of the expansion, allowing us to analyze convergence using the theorems presented in Section 2.1.2. Although the resulting D-Log indicates convergence beyond the radius of convergence of the Taylor series, we can only guarantee the convergence pattern within the region confined by the Taylor expansion.

Using the fundamental theorem of algebra we can express the Taylor expansion of order K as a product of their K -complex roots

$$f(z) \approx \sum_{n=0}^K f_n z^n = a_0 \prod_{k=1}^K (z - \mu_k) \quad (3.1)$$

applying the logarithm derivative we get the ratio of two polynomials

$$F(z) = \frac{\sum_{m=0}^{K-1} c_m z^m}{\sum_{n=0}^K f_n z^n} \quad (3.2)$$

The above expression suggests that the optimal approximant for constructing the D-log of this Taylor series is the subdiagonal Padé sequence \bar{P}_N^{N-1} . In the specific case where $N = K$, we can exactly reproduce the function $F(z)$ —which comes from the first K -terms of the expansion—. While this case is straightforward, our focus is on more complex functions that exhibit branch cuts. Specifically, we are interested in functions where the roots in Eq. (3.1) do not necessarily have simple or integer multiplicities—functions that can be expressed as

$$f(z) = e^{g_\ell(z)} \prod_{k=1}^K (z - \mu_k)^{\gamma_k} \quad (3.3)$$

where $g_\ell(z)$ is a polynomial of order ℓ , and γ_k is the corresponding multiplicity ($\gamma_k \in \mathbb{R}$) for each singularity point μ_k . This expansion is clearly not anymore the fundamental theorem of algebra¹, but a possible extension that tries to include poles and branch cuts.

Now then, if we apply the logarithm derivative to Eq. (3.3) we obtain:

$$F(z) = g'(z) + \sum_{k=1}^K \frac{\gamma_k}{z - \mu_k} \quad (3.4)$$

$$F(z) = g'(z) + \frac{\sum_{m=0}^{K-1} d_m z^m}{\sum_{n=0}^K e_n z^n} \quad (3.5)$$

Here, $g'(z)$ denotes the derivative of $g(z)$, which is a polynomial of degree $\ell - 1$. In this case, we also obtain a term that involves the ratio of two polynomials: one in the numerator of degree $K - 1$, and the other in the denominator of degree K , even if γ is not an integer,

¹The expression in Eq. (3.3) is not a particular case of the Weierstrass Factorization Theorem either. Although we include an exponential factor to ensure convergence of the product, the elementary factors account only for simple multiplicities at each zero of the function. As a result, Weierstrass Factorization extends the Fundamental Theorem of Algebra for the representation of entire functions [89, 90]. Since we introduce real exponents, the proposed expansion is more similar to a Puiseux series expansion [89, 91]

this information is now embedded in the coefficients of the numerator polynomial.

As a result, we obtain a meromorphic function, specifically a rational function that can be determined using PAs and convergence theorems for meromorphic functions (recall Section 2.1.2). By constructing a PA with upper index N for the numerator and lower index M for the denominator, we can apply Eq. (2.27) to the PA \bar{P}_M^N , yielding the following expression:

$$D_M^N[f(z)] = e^{g^{N-M+1}(z)} \prod_{m=1}^M (z - \mu_m)^{\gamma_m}. \quad (3.6)$$

This result is consistent with functions that satisfy Eq. (3.3), where $M = K$ and $N = \ell + K - 1$. The degree of the polynomial $g(z)$ can only increase with the upper index of the PA (N). Therefore, the lower index of the PA, and consequently of the D-Log, always reflects the number of branch points or cuts that the approximation is addressing.

It is important to note that not all functions with branch points and cuts can be expressed in the form given by equation 3.3. For example, in Section 5.2.2, we discuss D-logs with a different structure that includes transcendental functions within the exponential factor.

In the following section, we will present a convergence conjecture that states: If the function $f(z)$ is a Stieltjes function, then its logarithmic derivative $F(z)$ will also be of Stieltjes kind, allowing us to apply the theorem discussed in Section 2.1.3.

3.2 Conjecture of convergence for Stieltjes functions

We will show in this section that D-Log convergence to Stieltjes functions can be obtained using the same convergence theorems for PAs to Stieltjes functions. The rationale is the following. Since D-Logs are built from the exponentiation and integration over a Padé sequence $\bar{P}_M^N(z)$ to $F(z)$, if $F(z)$ is a Stieltjes function, then the diagonal sequence $\bar{P}_N^N(z)$ and near-diagonal $\bar{P}_N^{N\pm 1}(z)$ will bound $F(z)$. Integrating and exponentiating do not disturb the hierarchy of the sequences yielding the bounds for the D-Logs exploited in this work.

The question to answer now is whether the logarithmic derivative of a Stieltjes function is a Stieltjes function as well. A necessary and sufficient condition for a function $f(z)$ to be Stieltjes is that all determinants $\mathcal{D}_{m,n}^{(f)}$, made out of the moments f_n , are positive (Eq. (2.12)). Then, to prove that $F(z)$ is of a Stieltjes kind, we need to verify that its determinants $\mathcal{D}_{m,n}^{(F)}$ are all positive. Since they are not known, this may seem an impossible task. We know, however, that the determinants $\mathcal{D}_{m,n}^{(f)}$ of $f(z)$ are all positive. By relating the determinants of $F(z)$ to those of $f(z)$, and using the positivity condition of the latter, we can deduce the positivity condition of the former.

Taking account that the definition of a Stieltjes function gives us the moments f_n (see Eq. (2.10)), the distance between consecutive coefficients f_n and f_{n+1} can only be a function of n (regardless of whether the distance is increasing or decreasing):

$$f_n - f_{n+1} = \int_0^{\infty} u^n (1-u) d\phi(u). \quad (3.7)$$

This implies that either $f_n > f_{n+1}$ or $f_n < f_{n+1}$. The determinants of $f(z)$ are informative. In particular, the $\mathcal{D}_{n,0}^{(f)} > 0$ imply all $f_n > 0$ and Eq. 3.7 implies $\mathcal{D}_{n,1}^{(f)} = f_n f_{n+2} - f_{n+1}^2 > 0$. Similarly, combinations such as $f_n f_{n+3} - f_{n+1} f_{n+2}$ or $f_0 f_{n-1} - f_1 f_{n-2}$ are positive for all n . The reason is the following. We focus on the case where $f_n > f_{n+1}$ and, as stated, the distance between two consecutive f_n is $\sim 1/n$. The product $f_n f_{n+3} - f_{n+1} f_{n+2}$ represents the difference between the surface of two rectangles. Comparing sizes, f_n is larger than f_{n+1} by $1/n$ while $f_{n+2} - f_{n+3} \sim 1/(n+2)$. The surface of the first rectangle is then larger and the difference of surfaces is positive. If f_n coefficients grow with n , the argument is essentially the same.

We show now how the determinants of $F(z)$ can be built from the determinants of $f(z)$. Notice that $F(z)$ is the logarithm derivative of $f(z)$ and so we can express it as the ratio of two power series in z , according to Eq. (2.11).

$$F(z) = \frac{f'(z)}{f(z)} = \sum_{n=0}^{\infty} F_n z^n = \frac{\sum_{n=1}^{\infty} n f_n z^{n-1}}{\sum_{n=0}^{\infty} f_n z^n}. \quad (3.8)$$

The coefficients F_n are built from the Taylor coefficients of the product of two functions: $f'(z)$ and $1/f(z)$. The Taylor expansion around $z = 0$ of the product of two generic analytic functions $g(z)$ and $h(z)$ can be written in the compact form:

$$g(z)h(z) = \sum_{n=0}^{\infty} \frac{z^n}{n!} \sum_{i=0}^n \binom{n}{i} g_i h_{n-i}. \quad (3.9)$$

This expansion shows that the n -th coefficient of the product of two functions contains $n+1$ terms. A closer look at them reveals a hierarchy:

$$F_n = \sum_{i=0}^n (n+1-i) f_{n+1-i} \left(\frac{1}{f(z)} \right)_i, \quad (3.10)$$

where $\left(\frac{1}{f(z)} \right)_i$ refers to the i -th Taylor coefficient of $1/f(z)$. The $i=0$ term of $1/f(z)$ is simply $1/f_0$.

The terms in F_n from Eq. 3.10 have alternate sign as the $\left(\frac{1}{f(z)}\right)_i$ contributes with $(-1)^{i+1}$ (since all $f_n > 0$). In order to left $F_n > 0$ we absorb the sign in the variable in the power series, i.e. $F(z) = \sum F_n(-z)^n$. One can group them in terms of determinants of $f(z)$ for which the sign is known. The value of the coefficient F_n is dominated by the combination

$$F_n \approx \frac{(n+1)(f_0 f_{n+1} - f_n f_1) f_0^{n-1} + f_1^{n+1}}{f_0^{(n+1)}}, \quad (3.11)$$

which does not belong to any determinant and is positive. This particular combination arises from the $i = 0, 1$ and $i = n$ terms defining dominant term of F_n . The rest of $i = 2, \dots, n-1$ coefficients can be factorized in terms of $\mathcal{D}_{m,1}^{(f)}$. Since the determinants are very small, numerically, compared to coefficients f_n , terms proportional to a determinant are sub-leading. Since the dominant contribution is positive, $F_n > 0, \forall n$.

For the calculation of the determinants $\mathcal{D}_{n,m}^{(F)}$ of $F(z)$, we keep the dominant terms. The $i = 0$ coefficient of F_n is proportional to $(n+1)f_{n+1}$. This coefficient dominates as it is the biggest one, and positive, which ensures the determinants $\mathcal{D}_{n,1}^{(F)}$ are positive (using arguments similar to $\mathcal{D}_{n+1}^{(f)}$). In detail, the dominant term in $\mathcal{D}_{n,1}^{(F)}$ reads

$$\begin{aligned} \mathcal{D}_{n,1}^{(F)} = & \frac{(n+1)(f_{n+1}f_0 - f_n f_1)}{f_0^2} \frac{(n+3)(f_{n+3}f_0 - f_{n+2}f_1)}{f_0^2} \\ & - \frac{(n+2)^2(f_{n+2}f_0 - f_{n+1}f_1)^2}{f_0^4} + \dots \end{aligned} \quad (3.12)$$

Since $(n+1)(n+3) = (n+2)^2 - 1$, we can argue $(n+1)(n+3) \sim (n+2)^2$, group the first two terms of the $\mathcal{D}_{n,1}(F)$, and factorize the terms proportional to f_0^2, f_1^2 and $f_0 f_1$:

$$\begin{aligned} \mathcal{D}_{n,1}(F) \left(\frac{f_0^4}{(n+2)^2} \right) \approx & f_0^2(f_{n+1}f_{n+3} - f_{n+2}^2) \\ & + f_1^2(f_n f_{n+2} - f_{n+1}^2) \\ & - f_0 f_1(f_{n+3}f_n - f_{n+1}f_{n+2}). \end{aligned} \quad (3.13)$$

The coefficient of the term proportional to f_0^2 is the $\mathcal{D}_{n+1,1}^{(f)}$ of $f(z)$ and that of the term proportional to f_1^2 is the $\mathcal{D}_{n,1}^{(f)}$. The coefficient of the term proportional to $f_0 f_1$ is not a determinant. However, using the hierarchy of coefficients deduced from Eq. 3.7 we observe it is positive but smaller than the other two terms. We conclude $\mathcal{D}_{n,1}^{(F)} > 0, \forall n$.

The next step is related to the positivity condition that the higher-order determinants $\mathcal{D}_{n,m}^{(F)}$ must be satisfy. By Cramer's rule, $\mathcal{D}_{n,m}^{(F)}$ can be calculated by a sign-alternating sum of

different contributions as happens with the construction of the $\mathcal{D}_{n,1}(F)$ in Eq. 3.13. Among them, few are $\mathcal{D}_{n,m-1}^{(F)}$ determinants multiplied by the corresponding F_n coefficient, while the others are combinations of coefficients which are numerically smaller than $\mathcal{D}_{n,m-1}^{(F)}$. When applying Cramer's rule, one can always start with the term that contains the coefficient F_n with the smallest n . The subsequent terms compete and are sign alternating. The term with smallest n dominates and defines the sign of $\mathcal{D}_{n,m}^{(F)}$. As an example, $\mathcal{D}_{0,2}^{(F)}$ reads

$$\begin{aligned}\mathcal{D}_{0,2}^{(F)} &= F_0(F_2F_4 - F_3^2) - F_1(F_1F_4 - F_2F_3) + F_2(F_1F_3 - F_2^2) \\ &= F_0\mathcal{D}_{2,1}^{(F)} - F_1(F_1F_4 - F_2F_3) + F_2\mathcal{D}_{1,1}^{(F)} > 0.\end{aligned}\quad (3.14)$$

Since $\mathcal{D}_{n,1}^{(F)} > 0$, $\mathcal{D}_{n,1}^{(F)} > F_nF_{n+3} - F_{n+1}F_{n+2} > 0$ by virtue of Eq. 3.7 as argued before, and $F_n > F_{n+1}$, $\mathcal{D}_{n,m}^{(F)} > 0$, for all n , as we wanted to prove and we can then ensure that $F(z)$ is Stieltjes.

3.2.1 Example 1. "Stieltjes logarithm"

We illustrate the proof sketched above with the same example used in Section 2.1.3. It is $f(z) = \frac{\ln[1+z]}{z}$, cf. Eq. (2.13), whose corresponding moments are $f_n = \frac{1}{n+1}$, as was shown in Eq. (2.15). In this case:

- $\mathcal{D}_{n,0}^{(f)} > 0$ as $f_n = \frac{1}{n+1} > 0 \forall n$.
- $\mathcal{D}_{n,1}^{(f)} = f_n f_{n+2} - f_{n+1}^2 = \frac{1}{(n+1)(n+2)^2(n+3)} \sim \frac{1}{(n+2)^4} > 0 \forall n$. Notice $\mathcal{D}_{n,0}^{(f)} \gg \mathcal{D}_{n,1}^{(f)}$.
- $f_n - f_{n+1} = \int_0^1 u^n(1-u)du = \frac{1}{n^2+3n+2} > 0 \forall n$.
- $f'_n = \frac{n}{n+1} > 0, n \geq 1$.
- $(1/f)_n < 0 \forall n$.

With this at hand, the Taylor coefficients F_n of the function $F(z) = \frac{f'(z)}{f(z)}$ read

- $F_0 = \frac{f_1}{f_0} = \frac{1}{2}$,
- $F_1 = \frac{2f_0f_2 - f_1^2}{f_0^2} = \frac{f_0f_2 + (f_0f_2 - f_1^2)}{f_0^2} = \frac{1}{3} + \left(\frac{1}{3} - \frac{1}{2^2}\right) = \frac{1}{3} + \frac{1}{12} = \frac{5}{12}$,
- $F_2 = \frac{3(f_3f_0 - f_2f_1)f_0 + f_1^3}{f_0^3} = 3\left(\frac{1}{4} - \frac{1}{3} \frac{1}{2}\right) + \frac{1}{2^3} = \frac{2}{8} + \frac{1}{8} = \frac{3}{8}$,

- $F_3 = \frac{4(f_4f_0 - f_3f_1)f_0^2 + 2f_0f_2(f_1^2 - f_0f_2) - f_1(f_1^3 - 2f_0f_1f_2)}{f_0^4} = \frac{4(f_4f_0 - f_3f_1)f_0^2 - 2(f_1^2 - f_0f_2)^2 + f_1^4}{f_0^4} = \frac{3}{10} - \frac{2}{144} + \frac{1}{16} = \frac{251}{720},$
- $F_4 = \frac{5(f_5f_0 - f_4f_1)f_0^3 + 5f_3f_0^2(f_1^2 - f_0f_2) - 5f_2f_1f_0(f_1^2 - f_0f_2) + f_1^5}{f_0^5} = \frac{5(f_5f_0 - f_4f_1)f_0^3 + 5f_0(f_3f_0 - f_2f_1)(f_1^2 - f_0f_2) + f_1^5}{f_0^5} = \frac{1}{3} - \frac{5}{144} + \frac{1}{32} = \frac{95}{288},$
- $F_5 = \frac{6(f_6f_0 - f_5f_1)f_0^4 + [6f_0^2(f_4f_0 - f_3f_1) - 6f_0f_1(f_3f_0 - f_2f_1)](f_1^2 - f_0f_2)}{f_0^6} + \frac{-2(f_1^2 - f_0f_2)^3 + 3f_0(f_3f_0 - f_2f_1)(f_1^3 + f_1(f_1^2 - f_0f_2) - f_0^2f_3) + f_1^6}{f_0^6} = \frac{19087}{60480}.$

The recurrence pattern is clear: each F_n ($n > 2$) has a term $(n+1)(f_0f_{n+1} - f_1f_n)f_0^{n-1} = \frac{n}{2(n+2)} > 0$ that dominates over the negative terms which, in their turn, are proportional to $\mathcal{D}_{n,1}^{(f)}$. Since $\mathcal{D}_{n,1}^{(f)} \sim \frac{1}{(n+2)^4} \ll 1$, all the terms proportional to the determinants appearing in the construction of the F_n coefficients are negligible.

For the $\mathcal{D}_{n,1}^{(F)}$ determinants built for $F(z)$, we exploit the same hierarchy. Take the F_n coefficients, neglect the terms within them proportional to the determinants from $f(z)$ and also the one proportional to f_1^{n+1} . Then immediately one recognizes that $\mathcal{D}_{n,1}^{(F)} > 0 \forall n$. For example for $n = 1, 2$ we have:

$$\mathcal{D}_{n=1,1}^{(F)} = F_1F_3 - F_2^2 \sim \frac{1}{3} \frac{n+2}{2(n+4)} - \left(\frac{n+1}{2(n+3)} \right)^2 \Big|_{n=1} = \frac{3}{80},$$

$$\mathcal{D}_{n=2,1}^{(F)} = F_2F_4 - F_3^2 \sim \frac{3}{8} \frac{95}{288} - \left(\frac{251}{720} \right)^2 = \frac{281}{129600} \sim \frac{3}{8} \frac{1}{3} - \left(\frac{3}{10} \right)^2 = \frac{7}{200}$$

. We can explicitly calculate Eq. (3.13) for arbitrary n . Take now $n = 3$:

$$\mathcal{D}_{3,1}^{(F)} = \frac{(3+2)^2}{1} \left[1^2 \left(\frac{1}{5} \frac{1}{7} - \frac{1}{6^2} \right) + \frac{1}{2^2} \left(\frac{1}{4} \frac{1}{6} - \frac{1}{5^2} \right) + 1 \frac{1}{2} \left(\frac{1}{5} \frac{1}{6} - \frac{1}{7} \frac{1}{4} \right) \right] = \frac{1}{2016} \quad (3.15)$$

For $n > 4$, the dominant terms for each F_n allow a compact expression for the determinant:

$$\mathcal{D}_{n,1}^{(F)} = F_nF_{n+2} - F_{n+1}^2 = \frac{n-4}{4(n+3)(n+4)} > 0.$$

Higher-order determinants $\mathcal{D}_{m,n}^{(F)}$ can be constructed following the results from the lowest ones using the aforementioned Cramer's rule method, thus returning them all positive. As an example, $\mathcal{D}_{0,2}^{(F)}$ reads

$$\mathcal{D}_{0,2}^{(F)} = F_0\mathcal{D}_{2,1}^{(F)} - F_1(F_1F_4 - F_2F_3) + F_2\mathcal{D}_{1,1}^{(F)} = \frac{7}{400} - \frac{29}{10368} + \frac{9}{640} > 0. \quad (3.16)$$

We can conclude that $F(z)$ is a Stieltjes function since all its determinants are positive, as we wanted to demonstrate.

3.2.2 Example 2: "Stieltjes Exponential Integral"

For a second example we want to consider the following function:

$$f(z) = z^{-1} e^{z^{-1}} \operatorname{Ei}(-z^{-1}) \quad (3.17)$$

where $\operatorname{Ei}(z)$ is the exponential integral function defined by

$$\operatorname{Ei}(z) = - \int_{-z}^{\infty} \frac{e^{-t}}{t} dt. \quad (3.18)$$

This function (Eq. (3.17)) can be expressed as a Stieltjes integral (see, Eq. (2.9)), considering the weight function $\phi(u) = -e^{-u}$ for $u \in [0, \infty)$, therefore we have the Stieltjes function:

$$f(z) = \int_0^{\infty} \frac{e^{-u}}{1+zu} du \quad \operatorname{Re}(z) > 0. \quad (3.19)$$

Since, the measure corresponds to $d\phi(u) = e^{-u} du$, the f_n moments correspond to:

$$f_n = \int_0^{\infty} u^n e^{-u} du. \quad (3.20)$$

This integral is precisely the definition of the **Gamma function** $\Gamma(n+1)$, which is an analytical extension of factorial function in the complex plane. Thus, in case $n \in \mathbb{Z}$, we have:

$$f_n = n! \quad \text{for all } n \geq 0. \quad (3.21)$$

Indeed, computing the Taylor series for the example function Eq. (3.17) we get:

$$-1 + z - 2z^2 + 6z^3 - 24z^4 + 120z^5 - 720z^6 + 5040z^7 + \mathcal{O}(z^8) \quad (3.22)$$

which is in total agreement with Stieltjes series, Eq. (2.11), and clearly the Taylor coefficients corresponds to the factorial sequence. Now, to determine if the logarithm derivative is a Stieltjes functions we apply the conjecture and we need to verify at least the first moments of function $F(z)$, for that we need:

- $\mathcal{D}_{n,0}^{(f)} > 0$ as $f_n = n! > 0 \quad \forall n$.
- $\mathcal{D}_{n,1}^{(f)} = f_n f_{n+2} - f_{n+1}^2 = n! (n+2)! - (n+1)!^2 = n!^2 (n+1) > 0 \quad \forall n$.
- $f_{n+1} - f_n = \int_0^{\infty} u^n (u-1) e^{-u} du = n n! \geq 0 \quad \forall n$ (In this case we have the increasing hierarchy for the distance between consecutive moments, noting that distance is null

only for $n = 0$ i.e. $f_1 - f_0 = 0$).

- $f'_n = n n! > 0 \quad \forall n \geq 1$.
- $(1/f)_n < 0 \quad \forall n \geq 1$.

Now, knowing the moments of the example function f_n , the corresponding moments for the its logarithm derivative F_n can be calculated using Eq. (3.10) as follows:

- $F_0 = \frac{f_1}{f_0} = \frac{1!}{0!} = 1$,
- $F_1 = \frac{2f_0f_2 - f_1^2}{f_0^2} = 2(2!) - (1!)^2 = 3$,
- $F_2 = \frac{3f_0(f_0f_3 - f_2f_1) + f_1^3}{f_0^3} = 3((3!) - (2!)) + 1 = 13$,
- $F_3 = \frac{4f_0^2(f_0f_4 - f_3f_1) - f_1^4}{f_0^4} + \frac{2f_0f_2(2f_1^2 - f_0f_2)}{f_0^4} = 4((4!) - (3!)) - 1 + 2(2!)(2 - 2!) = 71$,
- $F_4 = \frac{5f_0^3(f_0f_5 - f_1f_4) + f_1^5}{f_0^5} + \frac{5(f_0f_1^2 - f_0^2f_2)(f_0f_3 - f_1f_2)}{f_0^5} = 5(5! - 4!) + 1 + 5(1 - 2!)(3! - 2!) = 481 - 20 = 471$.

For each moment there is a dominant term; it is $(n+1)((n+1)! - n!) = n(n+1)!$, which corresponds precisely to the first two terms of the approximation in Eq. (3.11). Until here we can ensure with this pattern that $F_n > 0$ for all n and the hierarchy $F_{n+1} > F_n$. To obtain determinants we can use the same procedure as the previous example, for instance $\mathcal{D}_{n=0,1}^{(F)} = F_0F_2 - F_1^2 = 4$, for this computation we used the exactly values for F_n , this determinant in particular ($\mathcal{D}_{0,1}^{(F)}$) is the smallest one and the approximation of Eq. 3.13 doesn't work, thus we must to consider the exact calculation for F_0, F_1, F_2 . Then, for $n \geq 1$ we can use Eq. 3.13, which in this case reads: $\mathcal{D}_{n,1}^{(F)} \approx (n^2 + n - 1)(n+1)(n+2)^2n!^2$. Some additional terms of order $m = 1$ are:

- $\mathcal{D}_{n=1,1}^{(F)} = F_1F_3 - F_2^2 = 44$
- $\mathcal{D}_{n=2,1}^{(F)} = F_2F_4 - F_3^2 = 952$
- $\mathcal{D}_{n=3,1}^{(F)} = F_3F_5 - F_4^2 = 32216$

All of them are positive and exhibit a factorial growing. Using the Cramer's rule the higher-order determinants can be constructed, as an example we can compute the first determinant of second order $\mathcal{D}_{0,2}^{(F)}$

$$\begin{aligned} \mathcal{D}_{0,2}^{(F)} &= F_0\mathcal{D}_{2,1}^{(F)} - F_1(F_1F_4 - F_2F_3) + F_2\mathcal{D}_{1,1}^{(F)} \\ &= 1(952) - 3(1383 - 923) + 13(44) \\ &= 144 \end{aligned}$$

Determinants of high-order are larger as n and m increase, therefore we can ensure that logarithm derivative of $f(z)$ (Eq. (3.17)) is also an Stieltjes function and we can apply convergence theorem exposed in Section 2.1.3.

Extrapolation MUonE data to find a_μ

The MUonE experiment aims to determine the leading-order of the Hadronic Vacuum Polarization (HVP) contribution to the anomalous magnetic moment of the muon, $a_\mu^{\text{HVP,LO}}$, by measuring the electron-muon scattering cross-section in the space-like region. However, to accurately extract $a_\mu^{\text{HVP,LO}}$, it is essential to determine the hadronic contribution to the electromagnetic coupling ($\Delta\alpha_{\text{had}}$) across the entire kinematic range. Since experimental data alone cannot fully provide this information, extrapolation methods are required.

In this chapter, which is based on a joint work in collaboration with researchers at the Instituto de Física de São Carlos (IFSC), see Ref. [81], we propose to use PAs and D-Logs as a systematic and model-independent method to fit and reliably extrapolate the future MUonE experimental data, extracting $a_\mu^{\text{HVP,LO}}$ with a conservative but competitive uncertainty, without using external information or very limited information. The method relies on fundamental analytic properties of the two-point correlator underlying $a_\mu^{\text{HVP,LO}}$ and provides lower and upper bounds for the result for $a_\mu^{\text{HVP,LO}}$. We demonstrate the reliability of the method using toy data sets generated from a model for $\Delta\alpha_{\text{had}}(t)$ whose integral over the entire kinematic range is directly proportional to $a_\mu^{\text{HVP,LO}}$. These toy data sets can reflect the expected statistics of the MUonE experiment.

The recent measurements of the anomalous magnetic moment of the muon, $a_\mu = (g - 2)/2$, by the FNAL E989 experiment at Fermilab, in 2021 and 2023 [42, 43], are in good agreement with the previous experimental result from the Brookhaven National Lab BNL E821 experiment of 2006 [44]. The combination of the results leads to an experimental determination of a_μ with an impressive uncertainty of only 0.19 ppm. As is well known, the

2020 $g - 2$ Theory Initiative White Paper [41] recommended result for a_μ in the Standard Model (based on the results of Refs. [38–40, 92–112]) is 5.1σ lower than the new, combined, experimental number — a tension that has attracted enormous attention in the past few years (since the experimental result was published, it has received 114 citations in less than a year). This result relies on the dispersive description of HVP contribution to a_μ^{HVP} based on e^+e^- data. If one employs instead the recent lattice QCD results for a_μ^{HVP} obtained by the BMW Collaboration [113], the discrepancy between theory and experiment would be reduced to 2.0σ , which is more in agreement with recent computations based on tau decay data for HVP contribution to muon $g-2$ leading in less than 2.5σ discrepancy [114].

Understanding the origin of the tension between the dispersive-based result and the lattice-based determination of a_μ^{HVP} is of crucial importance. The detailed comparison is not completely straightforward [82, 115, 116] since in lattice QCD one has access to the Euclidean HVP, while the dispersive approach relies on data for $e^+e^- \rightarrow (\text{hadrons})$ in the whole Minkowski domain. Independent information from other related processes may be crucial to fully resolve the persistent discrepancies. A prominent example is the use of τ decay data, which requires a non-trivial treatment of isospin corrections [114, 117]. In this context, the recently proposed MUonE experiment [118–120] would also be very welcomed. The proposal is to extract the HVP in the Euclidean domain, directly from data, from the measurement of the elastic $e\mu$ cross-section using the 150-GeV muon beam from CERN’s M2 beamline scattered off atomic electrons of a low- Z target. The experiment could yield competitive results after three years of data taking and would be able to cover approximately 86% [121, 122] of the integration interval required for the computation of a_μ^{HVP} at leading order, $a_\mu^{\text{HVP, LO}}$.

An important question is how to treat the remaining 14% of the $a_\mu^{\text{HVP, LO}}$ integral not directly accessible to the MUonE experiment. In principle, one could simply resort to external information and use the dispersive approach, perturbative QCD, and/or lattice QCD results. Another option, arguably more interesting, is to extract $a_\mu^{\text{HVP, LO}}$ exclusively from the MUonE data, which requires some form of extrapolation of the experimental results beyond the kinematically accessible region. This problem is, however, non-trivial since the experiment would have access to a narrow window in the Euclidean t variable, between $-0.153 \text{ GeV}^2 \leq t \leq -0.001 \text{ GeV}^2$. In Ref. [122], a model inspired by one-loop QED is put forward as a fitting function to fit and extrapolate the MUonE data. A disadvantage of this approach is a potential model dependency that could bias the final results. An alternate strategy suggested in Ref. [121] relies on the extraction of derivatives of the hadronic contribution to the running of the electromagnetic coupling, supplemented

with information from perturbative QCD and $R(s)$ data. Another recent proposal, closer in spirit to the analysis presented in this chapter, consists of using transfer theorems to build so-called *reconstruction approximants* which allow for a partial reconstruction of the HVP function to compute a_μ^{HVP} [123]. With all this motivation, we propose the use of PAs and D-Logs, as a systematic, simple, and model-independent way of fitting and extrapolating the MUonE results to compute $a_\mu^{\text{HVP,LO}}$ from MUonE data.

The extrapolation of the HVP results in the Euclidean domain using PAs has been explored previously in the context of heavy-quark physics [61] and lattice-QCD results [124]. The use of PAs in this problem is predicated on the fact that the HVP is a Stieltjes function [61]. In this case, we can use the convergence theorem exposed in section 2.1.3, where the diagonal and near-diagonal sequences of PAs guarantee the approximation from below while others do so from above, cf. Eqs. (2.16) and (2.17), providing a systematic way to bound the value of the function of interest.

By construction, the usual PAs are not able to explore the Minkowski region coming from the Euclidean domain as they contain *only* poles and zeros, and the branch cuts can be, at best, emulated by the accumulation of singularities –recall that in section 2.1.3 we stated that convergence for Stieltjes functions can be guaranteed *only* in the complex cut plane [52, 61, 125]–. Therefore, an excellent idea is to accompany the PAs study with the use of D-Logs, which contain, by construction, not only poles and zeros but also branch cuts. A systematic method for bounding the value of the function using D-Logs can be achieved by applying the convergence conjecture presented in Section 3.2. This can pave the way for future explorations where one could have a glimpse of the Minkowski region from fits in the Euclidean region in a model-independent and systematic way.

To assess the reliability and viability of our proposal we adopt a simple but sufficiently realistic model for the HVP function introduced in Ref. [123]. We then build the approximants first to the exact Taylor expansion of the model function and later to pseudo-data generated from the model. In this first step, we do not include uncertainties, as a proof of concept. We then generate realistic pseudo-data following the expected uncertainties and kinematic range accessible to the MUonE experiment [118–120, 122, 126–128]. With these data sets, we perform a systematic study of the use of PAs and D-Logs, as a way to fit and extrapolate MUonE data.

As we already mentioned, obtaining a_μ^{HVP} solely from MUonE data is a non-trivial problem. Therefore, we perform a systematic study where we enlarge in each step the window in which we rely on extrapolated results. In our systematic investigation, we show that there is a trade-off in precision. It is possible to perform a reliable, robust, and

model-independent extraction of $a_\mu^{\text{HVP,LO}}$ using approximants solely from MUonE data, but with a somewhat larger error. An advantage of the method is that both PAs and D-Logs allow for a reliable estimate of the systematic error. If the window in which one uses the extrapolated results is reduced, the error diminishes, as could be expected.

This chapter is organized as follows. In Sec. 4.1, we introduce the basic elements to describe the HVP contribution to the $(g-2)_\mu$ related to the running of the electromagnetic coupling constant. Also we discuss the analytical properties of the latter that can be considered as an Stieltjes function. In Sec. 4.2, we present the model of Ref. [123] that we use to generate our toy data sets for the Euclidean HVP, while an example of the power of the convergence theorems is presented in Sec. 4.3, where PAs and D-Logs are built from the exactly known Taylor series given by the model of Sec. 4.2. In Sec. 4.4, we employ our method in the idealized scenario where the data points have zero error. Sec. 4.5 illustrates the application of our method to realistic data sets, following the expectations of the MUonE experiment. Our conclusions are given in Sec. 4.6.

4.1 Hadronic Vacuum Polarization of a_μ

The Standard Model computation of a_μ can be divided into four different contributions, namely, from Quantum Electrodynamics (QED), electroweak effects, HVP, and hadronic light-by-light scattering. The dominant uncertainty arises from the HVP contribution [41], more specifically from its leading order $a_\mu^{\text{HVP,LO}}$. In the computation of a_μ^{HVP} the main object is the polarization function associated with the electromagnetic current two-point correlator, $\Pi(q^2)$, defined as

$$(q_\mu q_\nu - q^2 g_{\mu\nu})\Pi(q^2) = i \int d^4x \langle 0|T(j_\mu^{\text{EM}}(x)j_\nu^{\text{EM}}(0)|0\rangle, \quad (4.1)$$

where the electromagnetic current is

$$j_\mu^{\text{EM}} = \frac{2}{3}\bar{u}\gamma_\mu u - \frac{1}{3}\bar{d}\gamma_\mu d - \frac{1}{3}\bar{s}\gamma_\mu s + \frac{2}{3}\bar{c}\gamma_\mu c + \dots \quad (4.2)$$

We define $\bar{\Pi}(q^2) = \Pi(q^2) - \Pi(0)$, and the function $\bar{\Pi}(q^2)$ obeys the usual once-subtracted dispersion relation

$$\bar{\Pi}(q^2) = q^2 \int_{m_\pi^2}^{\infty} ds \frac{\text{Im } \Pi(s)}{s(s - q^2 + i\epsilon)}. \quad (4.3)$$

In the dispersive approach, $a_\mu^{\text{HVP,LO}}$ is obtained from the inclusive hadronic electropro-

duction cross-section defined, with $s = q^2$, as

$$R(s) = \left(\frac{3s}{4\pi\alpha^2} \right) \sigma_{e^+e^- \rightarrow \text{hadrons}}(s) = 12\pi \text{Im}\Pi(s), \quad (4.4)$$

through the following weighted integral

$$a_\mu^{\text{HVP, LO}} = \frac{\alpha^2}{3\pi^2} \int_{m_\pi^2}^{\infty} \frac{ds}{s} K(s)R(s), \quad (4.5)$$

where α is the electromagnetic fine-structure constant and $K(s)$ is the QED kernel function [129–131]

$$K(s) = \int_0^1 \frac{x^2(1-x)}{x^2 + (1-x)\frac{s}{m_\mu^2}} dx. \quad (4.6)$$

The analytical result for $K(s)$ is given explicitly in Ref. [41].

An alternate representation for $a_\mu^{\text{HVP, LO}}$ in terms of the correlator in the Euclidean, $\Pi(Q^2)$ with $Q^2 = -q^2 > 0$, can be obtained interchanging the order of the integrals in s and x in Eq. (4.5) [132]. Using the analytical properties of $\Pi(q^2)$ one can then write

$$a_\mu^{\text{HVP, LO}} = \frac{\alpha^2}{\pi} \int_0^1 dx (1-x) \Delta\alpha_{\text{had}}[t(x)], \quad (4.7)$$

where, following the notation employed by Bernecker and Meyer in Ref. [133], we defined

$$\Delta\alpha_{\text{had}}(t) = -4\pi \text{Re}[\bar{\Pi}_{\text{had}}(t)] \quad (4.8)$$

as the hadronic contribution to the running of the electromagnetic coupling α and t is the space-like variable given by

$$t = -\frac{x^2 m_\mu^2}{1-x}. \quad (4.9)$$

The MUonE experiment is designed to extract $\Delta\alpha_{\text{had}}(t)$ from $e\mu$ scattering data using 150 GeV muons scattered off atomic electrons. This allows, in principle, for a completely independent determination of $a_\mu^{\text{HVP, LO}}$. However, the experiment would be restricted approximately to the window $x \in [0.2, 0.93]$ [118–120, 122, 126–128], which corresponds to $-0.15 \text{ GeV}^2 \lesssim t \lesssim -0.001 \text{ GeV}^2$. To obtain $a_\mu^{\text{HVP, LO}}$ from MUonE data without requiring external information, it is imperative to have a reliable method to extrapolate the MUonE data way outside the experimentally accessible window. With this purpose in mind, we will use a set of approximants as fitting functions to toy data sets for $\Delta\alpha_{\text{had}}(t)$ simulating the expected results of the MUonE experiment.

Finally, uncertainty assessment is crucial and we want to keep track of the goodness of our extrapolation beyond the fit region. The extrapolation for $0 \leq x < 0.2$ is safe, since it involves a small interval in t , not too far from the origin, namely $0 \leq t \lesssim 0.001 \text{ GeV}^2$. The extrapolation for $0.93 < x < 1$, on the other hand, corresponding to $0.15 \text{ GeV}^2 \lesssim t < \infty$, is non-trivial and, in order to assess it carefully, we define $a_\mu^{\text{HVP,LO}}(x_{\text{max}})$ as the partial contribution from $x = 0$ up to $x = x_{\text{max}}$ to $a_\mu^{\text{HVP,LO}}$, expressed as

$$a_\mu^{\text{HVP,LO}}(x_{\text{max}}) = \frac{\alpha^2}{\pi} \int_0^{x_{\text{max}}} dx (1-x) \Delta\alpha_{\text{had}}[t(x)]. \quad (4.10)$$

The method we present not only in this chapter, but also in the rest of the thesis has several advantages. Fundamentally, the fitting functions based on the PAs and D-Logs do not rely on any particular model, instead, they rely only on the analytical properties of the function to approximate. In this case, this function is $\Delta\alpha_{\text{had}}(t)$, which will be explained in the next section. Besides that, the PAs are easily derived and simple to employ as fitting and extrapolating functions.

4.1.1 $\Delta\alpha_{\text{had}}(t)$ Analytic Properties

It is possible to prove that the hadronic contribution to the running of α , $\Delta\alpha_{\text{had}}$ (Eq. (4.8)), which is related to the inclusive hadronic electroproduction cross-section, is a Stieltjes function defined in the region $-\infty < t \leq 0$ [61, 134]. Thus, Padé theory concerning to Stieltjes functions (see Sections 2.1.3 and 3.2) can be applied. In particular, we know that the poles of approximants of the type P_N^{N+k} with $k \geq -1$, as well as the branch points and cuts of D-Logs of the type D_N^{N+k} with $k \geq -1$ that approximate to $\Delta\alpha_{\text{had}}$, are always real and located on the positive real axis of t with positive residues. Furthermore, since $\Delta\alpha_{\text{had}}$ scales as $\mathcal{O}(t^1)$ for small t , the PA sequences P_N^N and both P_N^{N+1} and P_{N+1}^N bound the original function. In our case, the fastest convergence is obtained with the super-diagonal sequence P_N^{N+1} , then the theorem reads

$$P_1^1(t) \leq P_2^2(t) \leq \dots \leq \Delta\alpha_{\text{had}} \leq \dots \leq P_2^3(t) \leq P_1^2(t). \quad (4.11)$$

For the D-Logs case, a similar pattern is found. The sequence D_N^N together with D_{N+1}^N and D_N^{N+1} bound the original function. In our case of study, we found the fastest convergence with the sub-diagonal sequence D_{N+1}^N , which renders the theorem as

$$D_1^1(t) \leq D_2^2(t) \leq \dots \leq \Delta\alpha_{\text{had}} \leq \dots \leq D_3^2(t) \leq D_2^1(t). \quad (4.12)$$

Besides being model-independent, this method takes advantage of the convergence theorems of Padé Theory. To construct the functions that will be used to fit the MUonE toy data in a form that makes contact with the convergence theorems, we will first compute the PAs and D-Logs to the (unknown) Taylor series of $\Delta\alpha_{\text{had}}(t)$, i.e., we will build canonical approximants to

$$\Delta\alpha_{\text{had}}(t) = a_1 t + a_2 t^2 + a_3 t^3 + \dots, \quad (4.13)$$

where the coefficients a_n are unknown. However, it is important to note that we already have information on the origin; $\Delta\alpha_{\text{had}}(0) = 0$, implying that $a_0 = 0$ and suggesting a zero in $t = 0$. Then, after a change of variable from t to x using Eq. (4.9), we finally get our fitting functions as a function of x . With this technique, we can use our knowledge of Stieltjes functions in full to analyze the fit quality and provide constraints to the fit parameters.

In particular, from Carleman's condition [52, 135], the Taylor coefficients of a Stieltjes series cannot change sign and, in this case, they have to be negative. Moreover, the determinant condition imposes the following hierarchy for the coefficients

$$0 > a_i > a_{i+1}, \quad i \in \mathbb{N}. \quad (4.14)$$

All these constraints will be used in the fit procedure and it is important to mention that they are model-independent, relying only on $\Delta\alpha_{\text{had}}(t)$ being a Stieltjes function. Finally, since $\Delta\alpha_{\text{had}}(t)$ has $a_0 = 0$, the $P_M^N(t)$ will match $N + M$ coefficients instead of $N + M + 1$, and D-Log $D_M^N(t)$ also match $N + M$ instead of $N + M + 2$. In a more rigorous way in this case we are talking of a Partial D-logs $\text{PD}_{M,1}^N(t)$, since we know about singularity position at $t = 0$ with multiplicity 1. Since we can divide the original function by t we will going to apply D-Logs and not Partial D-Logs for simplicity.

4.2 A model for the Euclidean correlator

To test our method, we need to generate toy data sets based on a sufficiently realistic model. We will use the phenomenological model for the function $\text{Im } \Pi_{\text{had}}(s)$ inspired by chiral perturbation theory and perturbative QCD introduced by Greynat and de Rafael in Ref. [123] to obtain $\Delta\alpha_{\text{had}}$ through the dispersion relation in Eq. (4.3) and Eq. (4.8). The model is given by

$$\text{Im } \Pi_{\text{had}}(s) = \frac{1}{4\pi} \left(1 - \frac{4m_\pi^2}{s}\right)^{3/2} \left(\frac{|F(s)|^2}{12} + \sum_f Q_f^2 \Theta(s, s_c, \Delta) \right) \theta(s - 4m_\pi^2), \quad (4.15)$$

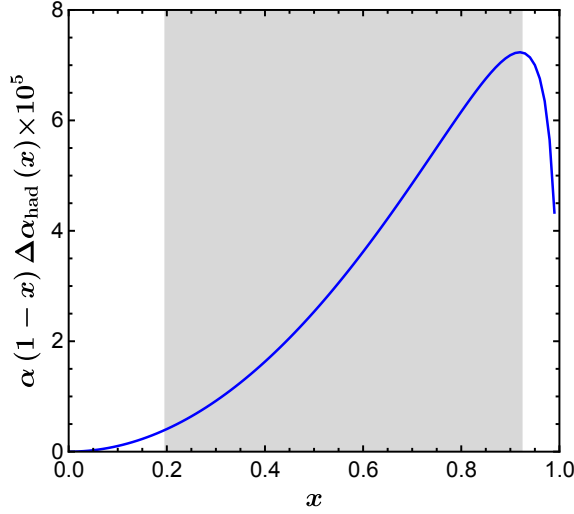


Figure 4.1: The integrand to obtain $a_\mu^{\text{HVP,LO}}$, given in Eq. (4.7), calculated from the model of Greynart and de Rafael of Eq. (4.15). The gray area is the expected region that the MUonE experiment will cover.

with Q_f being the electric charge of the quark of flavor f and $\theta(x)$ the Heaviside theta function. The function $|F(s)|^2$ is the pion vector form factor, which is modeled simply by the $\rho(770)$ contribution as

$$|F(s)|^2 = \frac{m_\rho^4}{(m_\rho^2 - s)^2 + m_\rho^2 \Gamma(s)^2}, \quad (4.16)$$

where the running width is

$$\Gamma(s) = \frac{m_\rho s}{96\pi f_\pi^2} \left[\left(1 - \frac{4m_\pi^2}{s}\right)^{3/2} \theta(s - 4m_\pi^2) + \frac{1}{2} \left(1 - \frac{4m_K^2}{s}\right)^{3/2} \theta(s - 4m_K^2) \right], \quad (4.17)$$

with $f_\pi = 93.3 \text{ MeV}$ being the pion decay constant and $m_{\{\pi, K, \rho\}}$ the meson masses. The function $\Theta(s, s_c, \Delta)$ is defined as

$$\Theta(s, s_c, \Delta) = \left[\frac{\arctan\left(\frac{s-s_c}{\Delta}\right) - \arctan\left(\frac{4m_\pi^2-s_c}{\Delta}\right)}{\frac{\pi}{2} - \arctan\left(\frac{4m_\pi^2-s_c}{\Delta}\right)} \right]. \quad (4.18)$$

The parameters s_c and Δ will assume the same values employed in Ref. [123]: $s_c = 1 \text{ GeV}^2$ and $\Delta = 0.5 \text{ GeV}^2$. We show in Fig. 4.1 the line shape of the integrand of Eq. (4.7) obtained from the use of this model where the gray band represents the experimentally accessible region with the designed MUonE experiment [118–120, 122, 126–128].

We consider this simple model to be sufficiently realistic because it leads to a representation of $\Delta\alpha_{\text{had}}$ which is a Stieltjes function, as expected in QCD. Hence, the theorems given in Sec. 2.1.3 and the coefficient constraints of Eq. (4.14) are all valid.

Computing the integral of Eq. (4.7) using the model in Eq. (4.15) we determine the value of $a_{\mu}^{\text{HVP,LO}}$ from this model as

$$a_{\mu, \text{model}}^{\text{HVP,LO}} = 6992.4 \times 10^{-11}. \quad (4.19)$$

This result will serve as a guide for us to compare the values of $a_{\mu}^{\text{HVP,LO}}$ obtained from our PA and D-Log approximants.

4.3 approximants to the Taylor series

In this section, we will canonically build PAs and D-Logs with the assumption of knowing the original function; in the case of PAs this is achieved by matching the Taylor series of each approximant to the Taylor series of $\Delta\alpha_{\text{had}}(t)$ —this procedure corresponds precisely to the one described in Eq. (2.3)—, in the case of D-Logs the procedure was established in Section 2.2.1 where $f(z)$ corresponds to the Taylor series of $\Delta\alpha_{\text{had}}(t)$, defined in Eq. (4.13), which will be computed from the model of Eq. (4.15). Recall that convergence theorems to Stieltjes functions apply in this case. Thus, convergence to the $a_{\mu}^{\text{HVP,LO}}$ value of the model, Eq. (4.19), is guaranteed and must respect the pattern determined in Eq. (4.11) and (4.12). The Taylor series of $\Delta\alpha_{\text{had}}$ as a function of t according to the model in Eq. (4.2) is.

$$\alpha \Delta\alpha_{\text{had}}(t) \times 10^5 = -918 t - 1752 t^2 - 6066 t^3 - 31589 t^4 - 214058 t^5 + \mathcal{O}(t^6). \quad (4.20)$$

4.3.1 Convergence of PAs results

Results from the sequences $P_N^N(t)$ and $P_N^{N+1}(t)$ are shown in Fig. 4.2a, in the range $0 \leq x \leq 0.997$, which corresponds to $-4 \text{ GeV}^2 \leq t \leq 0 \text{ GeV}^2$. The value from the model for $\Delta\alpha_{\text{had}}$ is represented by the black line in Fig. 4.2a. One can notice that both sequences approach consistently the true value of the model when the order of the PAs is increased and they also bound the model value as expected by the convergence theorem of Eq. (4.11): the PAs of the sequence P_N^N approach the function from below while the ones belonging to the sequence P_N^{N+1} do so from above. Additionally, it is possible to observe that for large values of $|t|$, the discrepancy between the approximants and the model is much more noticeable. Since the PAs are constructed from the Taylor series coefficients of $\Delta\alpha_{\text{had}}(t)$,

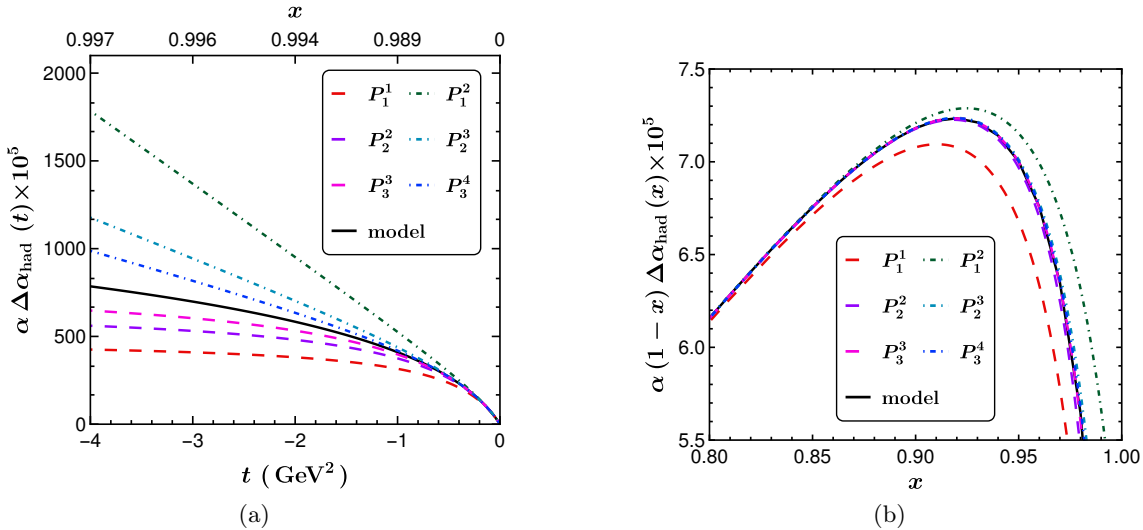


Figure 4.2: PAs of the sequences $P_N^N(t)$ (dashed line) and $P_N^{N+1}(t)$ (dot-dashed line) built from the Taylor series of $\Delta\alpha_{\text{had}}(t)$ given in Eq. (4.20), together with the model results (black line) for (a) $\alpha\Delta\alpha_{\text{had}}(t)$ and (b) $\alpha(1-x)\Delta\alpha_{\text{had}}(x)$ used to compute $a_\mu^{\text{HVP,LO}}$ with Eq. (4.7).

i.e. in the region of t close to zero, it is to be expected that far from this region the PAs start to deviate from the true model value. Notice, however, that the PA convergence is dramatically faster compared with that of the Taylor expansion, which breaks off outside a radius of convergence around $|t|=4m_\pi^2 \sim 0.1\text{GeV}^2$. The deviation of our approximants at large t is mitigated in the case of the integrand that appears in the calculation of $a_\mu^{\text{HVP,LO}}$, which can be seen in Fig. 4.2b as a function of x . Since the integrand goes to zero as x goes to 1, differences in the deep Euclidean region are suppressed, although still noticeable for lower-order PAs. One should also note that the change of variables from t to x maps the entire infinite interval $t \in (-\infty, -4 \text{ GeV}^2]$ into the small interval $x \in [0.997, 1]$.

We know from Padé Theory that the approximants can mimic branch cuts by accumulating interleaved poles and zeros along the cut (see Section 2.1). For higher-order PAs the mimicking of the cut originated by the term $(1 - 4m_\pi^2/t)^{3/2}$ in the model of Eq. (4.15), and whose branch point is located at $t = 0.078 \text{ GeV}^2$, have a good estimation. Consider the PA $P_3^4(t)$ as an example. This approximant must exhibit three poles, located at $t = 0.103 \text{ GeV}^2$, $t = 0.204 \text{ GeV}^2$, and $t = 0.637 \text{ GeV}^2$. Additionally, there are three zeros, apart from the one at $t = 0$, positioned at $t = 0.105 \text{ GeV}^2$, $t = 0.228 \text{ GeV}^2$, and $t = 3.329 \text{ GeV}^2$. This suggests the presence of a possible branch point or cut at approximately $t \approx 1.01 \text{ GeV}^2$, with a relative error of 32%. When considering PAs of even higher orders, this feature becomes more pronounced. For example, with $P_5^6(t)$, there

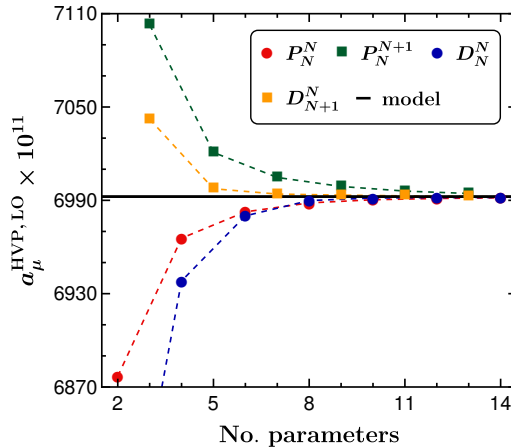


Figure 4.3: Comparison between PA and D-Log estimates of $a_\mu^{\text{HVP, LO}}$ and the value predicted by the model given in Eq. (4.19) (black solid line). ‘No. parameters’ refers to the value of $N + M$ used for each approximant.

are five poles at $t = \{0.089, 0.116, 0.187, 0.426, 1.192\} \text{ GeV}^2$, interleaved with zeros at $t = \{0.089, 0.118, 0.198, 0.620, 7.951\} \text{ GeV}^2$. Thus, the cut location for this approximant appears to be around $t \approx 0.089 \text{ GeV}^2$, with relative error of 14.1%. It is crucial to note that the latter estimate should not be mistaken for a "defect", as the PAs are constructed for a Stieltjes function. The positivity condition for the Hankel determinants of their moments, as shown in Eq. (2.12), ensures that no defect effects occur for Stieltjes functions under canonical construction. However, due to limited precision concerning this "pole-zero" pair at $t = 0.089 \text{ GeV}^2$, the confidence in the exact cut location remains low.

After building the PAs we can turn to the estimate of the value for $a_\mu^{\text{HVP, LO}}$. The results can be seen in Fig. 4.3, with the black solid line representing the model’s value given in Eq. (4.19). Again, the pattern stated by the theorem in Eq. (4.11) is obeyed, with the PAs sequence $P_N^N(t)$ (illustrated by the dashed red line) reaching the model result from below and sequence $P_N^{N+1}(t)$ (dashed green line) approaching from above. The convergence to the true value, which is guaranteed by theorems, can also be observed.

4.3.2 Convergence of D-Logs and comparison with PAs results

As discussed in Section 2.2.1, the D-Logs are built from the logarithm derivative of the original function (In this case, we use the Taylor series of $\Delta\alpha_{\text{had}}$), hence we first need to calculate $\frac{d}{dt} \ln(\Delta\alpha_{\text{had}}(t))$ and then we canonically construct a PA to it, i.e. by matching coefficients. After that, employing Eq. (2.27), we can obtain our D-Log approximant to

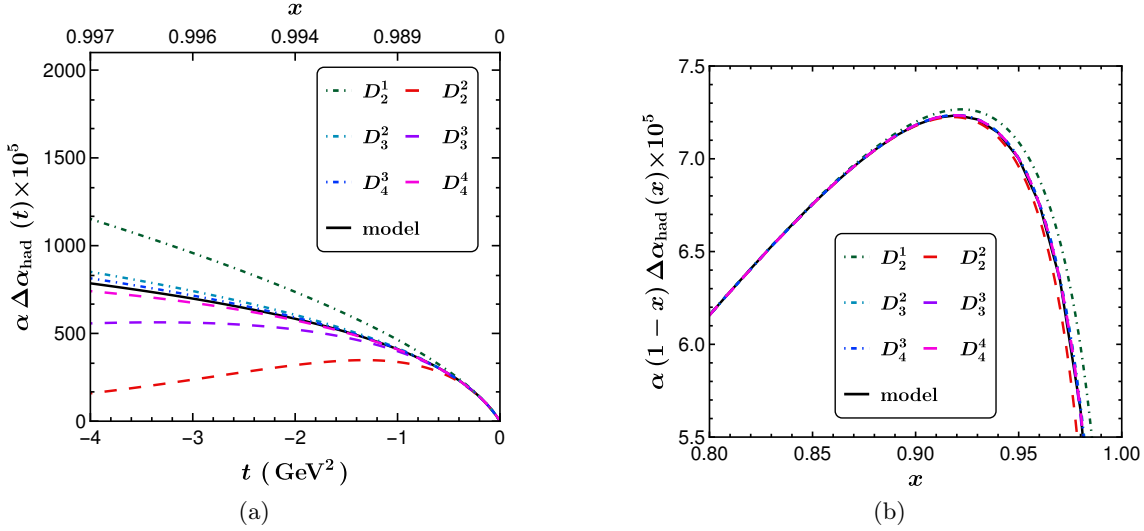


Figure 4.4: D-Logs of the sequences $D_N^N(t)$ (dashed line) and $D_{N+1}^N(t)$ (dot-dashed line) built from the Taylor series of $\Delta\alpha_{\text{had}}(t)$ given by Eq. (4.20) together with the model results (black line) for (a) $\alpha\Delta\alpha_{\text{had}}(t)$ and (b) $\alpha(1-x)\Delta\alpha_{\text{had}}(x)$. Both plots are in the same scale as the PA ones, Figs. 4.2a and 4.2b respectively, to facilitate the comparison.

$\Delta\alpha_{\text{had}}(t)$. As stated by the convergence theorems, specific sequences of D-Logs to $\Delta\alpha_{\text{had}}(t)$ bound the function from above (D_{N+1}^N) and from below (D_N^N), as can be seen in Fig. 4.4, in complete analogy to the convergence pattern of PAs shown in Figs. 4.2a and 4.2b.

Compared to PAs, D-Logs contain built-in branch cuts. For example, $D_5^5(t)$ has four branch cuts and one exponential factor. The onset of the first branch cut for each D-Log approaches the two-pion production threshold of the model, and this is done hierarchically: the D-Log $D_6^5(t)$ predicts the production threshold to be at $t = 0.083 \text{ GeV}^2$ and the D-Log $D_9^9(t)$ at $t = 0.0798 \text{ GeV}^2$. With this value, we can predict the charged pion mass to be 0.141 GeV , to compare with 0.140 GeV used in the model of Eq. (4.15), it means 1.9% of relative error, which is much better than what was obtained in the PAs case. In the other hand, the model suppresses this cut with the effect of other branch points and cuts present in the function and therefore the multiplicity of this cut decreases as the order of D-Logs increases, establishing in 0.005 for D_9^9 as an effective multiplicity for this cut. We also noticed all D-Logs have a branch cut that tends to be a square root with the singularity around $\sim 0.49 \text{ GeV}^2$. This branch cut can be interpreted as a signal of the ρ meson mass and an attempt to replicate the Breit-Wigner distribution used by the model in Eq. (4.16).

Finally, in Fig. 4.3 we compare the performance of both PAs and D-Logs provided the same amount of coefficients of the Taylor expansion are used. Subdiagonal D_{N+1}^N performs better than P_N^{N+1} when approaching from above for all orders, while diagonal PAs do

better than diagonal D-Logs when approaching from below. Notice however that the latter comparison holds up only to the number of parameters up to 6, above which the diagonal D-Logs surpass PAs as they converge faster. Not only Cauchy convergence is observed in both sequences but absolute convergence as well. Both methods are useful when bounding the function. For a large number of parameters, D-Logs would converge faster but for lower orders, none of the methods is systematically superior. We shall keep both methods for our fitting function study.

4.4 approximants to data with no error

In the previous section we built PA and D-logs in a canonical way, however, both approaches could be used as a fitting tool. To introduce us in to this technique, let us consider now an idealized case, where the data points represent exactly what is expected from the model of Eq. (4.15), with zero error. It is convenient to work with data for $\alpha \Delta\alpha_{\text{had}}(x) \times 10^5$ such that the Taylor coefficients a_n are of a natural size, which makes the fit simpler. The values of x were calculated as follows: the interval $0.2 \leq x \leq 0.93$ was divided into 30 equally spaced bins and we take the center of each bin, without any error, as the representative values of x where we will generate the data points to be fitted with our approximants.

To obtain our fitting functions, we construct both PAs and D-Logs using arbitrary Taylor series coefficients of $\Delta\alpha_{\text{had}}(t)$. These approximants are then transformed to the x variable using Eq. (4.9). By simplifying, we express the approximants in terms of the new coefficients but keeping the same degrees of freedom. These functions will then be used to perform the fits to the toy data sets where the fit parameters can be written in terms of the Taylor coefficients of $\Delta\alpha_{\text{had}}(t)$. PAs used as fitting functions were already applied in similar contexts and the convergence theorems are apparently satisfied in these cases [20, 40, 85–88]. It is important to emphasize, however, that the theorems presented in Sections 2.1.2 and 2.1.3 are demonstrated in the case of canonical PAs, i.e. those built to the Taylor series coefficients. Strictly speaking, in the case of a fit to data points in a given interval, we conscientiously slightly depart from the conditions of the theorem as a fit to data can be interpreted as imposing one matching condition for each datum instead of $N + M$ conditions at the same point. Therefore, we expect convergence theorems to be, as we will see, satisfied in this case as well but the convergence velocity may be smaller.

To show in detail a concrete case of our procedure, we start by examining the PA $P_1^1(t)$. To construct the fitting function, we first compute $P_1^1(t)$ as a function of the arbitrary

(unknown) Taylor series coefficients a_n of $\Delta\alpha_{\text{had}}(t)$ given by Eq. (4.13). We Taylor-expand the PA and $\Delta\alpha_{\text{had}}(t)$ and match the coefficients of both order by order. We then perform the change of variables using Eq. (4.9) which leads to the fitting function in terms of x . It is important to mention here that we will use the same notation $P_M^N(x)$ to refer to the fitting functions derived from the PA $P_M^N(t)$ even though they are not a PA of order $N + M$ in the variable x .

$$P_1^1(t(x)) \equiv P_1^1(x) = -\frac{a_1^2 m_\mu^2 x^2}{a_1 - a_1 x + a_2 m_\mu^2 x^2} = -\frac{b_1 m_\mu^2 x^2}{1 - x + b_2 m_\mu^2 x^2}, \quad (4.21)$$

where the fit parameters are $b_1 = a_1$ and $b_2 = a_2/a_1$. Due to the hierarchy of the Taylor coefficients of $\Delta\alpha_{\text{had}}(t)$, given by Eq. (4.14), we can conclude that b_1 and b_2 have to obey the following relations: $b_1 < 0$ and $b_2 > 1$, which will be imposed in the fit.

To obtain the parameters of the PAs and D-Logs from these fits to this zero-error data, we will perform the minimization of the fit quality \mathcal{Q}^2 given simply by

$$\mathcal{Q}^2 = \sum_{i=1}^{30} [\alpha \Delta\alpha_{\text{had}}(x_i) \times 10^5 - \mathcal{P}_M^N(x_i)]^2, \quad (4.22)$$

where $\mathcal{P}_M^N(x)$ refers, generically, to a PA $P_M^N(x)$ or to a D-Log $D_M^N(x)$. In reasonable fits, we expect very small values for \mathcal{Q}^2 . For $P_1^1(x)$, after the minimization we get $\mathcal{Q}^2 = 1.18 \times 10^{-3}$ and the values of the fit parameters b_1 and b_2 lead to the following Taylor series coefficients

$$a_1 = -912 \text{ GeV}^{-2} \quad \text{and} \quad a_2 = -1489 \text{ GeV}^{-4}, \quad (4.23)$$

which differ from the true values by only 0.7% and 15%, respectively. Furthermore, the pole of this PA in t is at $t_{\text{pole}} = 0.61 \text{ GeV}^2$. As stated by the convergence theorems, the pole is located on the positive real axis of t .

The PA can then be used to estimate the value of $a_\mu^{\text{HVP,LO}}$. By employing the resulting $P_1^1(x)$ in Eq. (4.7) we get

$$a_{\mu, P_1^1}^{\text{HVP,LO}} = 6933 \times 10^{-11}, \quad (4.24)$$

with a relative error of 0.9% compared to Eq. (4.19), the expected value within our model.

The same analysis can be made for the other PAs of the sequences $P_N^N(t)$ and $P_N^{N+1}(t)$, that will be resumed in Table 4.1.¹ We will employ only these two sequences since they are expected to bound the real function in the theorem presented in Section 2.1.3. We will

¹The fitting functions obtained from these approximants are constructed explicitly in Appendix B.

Table 4.1: Fitting functions constructed as PAs in variable x with free parameters b_i .

$P_M^N(x)$	Fitting function in x
P_1^1	$-\frac{b_1 m_\mu^2 x^2}{1-x+b_2 m_\mu^2 x^2}$
P_1^2	$-\frac{b_1 m_\mu^2 x^2 (1-x)+(b_1 b_3-b_2) m_\mu^4 x^4}{(1-x)^2+b_3 m_\mu^2 x^2 (1-x)}$
P_2^2	$\frac{b_1 m_\mu^2 x^2 (x-1)+(b_2-b_1 b_3) m_\mu^4 x^4}{(1-x)^2+b_3 m_\mu^2 x^2 (1-x)+b_4 m_\mu^4 x^4}$
P_2^3	$-\frac{b_1 m_\mu^2 x^2 (1-x)^2-(b_2+b_1 b_4) m_\mu^4 x^4 (1-x)+(b_3+b_1 b_5+b_2 b_4) m_\mu^6 x^6}{(1-x)^3-b_4 m_\mu^2 x^2 (1-x)^2+b_5 m_\mu^4 x^4 (1-x)}$

build several approximants from each sequence, in order to study the convergence pattern, but the final estimate of $a_\mu^{\text{HVP,LO}}$ will not include all results, as we detail below. Fig. 4.5a shows the values predicted by the PAs of the sequences P_N^N and P_{N+1}^N for $a_\mu^{\text{HVP,LO}}$. It is possible to notice that the pattern of convergence of Eq. (4.11), where the P_N^N bound the true value from below and the ones of P_{N+1}^N from above, is satisfied in this case. One can note in Fig. 4.5a that in some cases when the order of the PA is increased there is no real improvement in the estimate of $a_\mu^{\text{HVP,LO}}$. This can be explained by the appearance of a *defect*, which consists of a pole partially canceled by a nearby zero, effectively reducing the order of the PA, very similar to what happened with the PA P_3^3 in the example of Section 2.1.1. It is known from PA theory that approximants applied canonically to Stieltjes functions, i.e. to their Taylor series, cannot have Froissart doublets, see Section 2.1.3. Nonetheless, the theorem does not prevent the PA to have numerical defects, which are almost exact cancellations between poles and zeros, arising from the fitted parameters. Adding more coefficients into a fitting function also introduces larger correlations among them. As such, fitted coefficients will have errors and within their allowed fitted regions, cancellations may emerge. We note, however, that the important fact that the two sequences of PAs bound the true value remains true.

A final estimate for $a_\mu^{\text{HVP,LO}}$ from the PAs can then be obtained. For that, we will limit the analysis to the first two approximants in each sequence, i.e. P_1^1 , P_2^2 , P_1^2 and P_2^3 . This choice is motivated by the fact that we do not expect to be able to fit much more than 5 parameters in more realistic scenarios, with a limited number of data points and with the errors expected by the MUonE experiment. Computing the central value of the prediction as the mean between the four approximants we get $a_{\mu, \text{PAs}}^{\text{HVP,LO}} = 6990 \times 10^{-11}$, which differs from the expected value given in Eq. (4.19) by 0.04%. This can be improved if we take

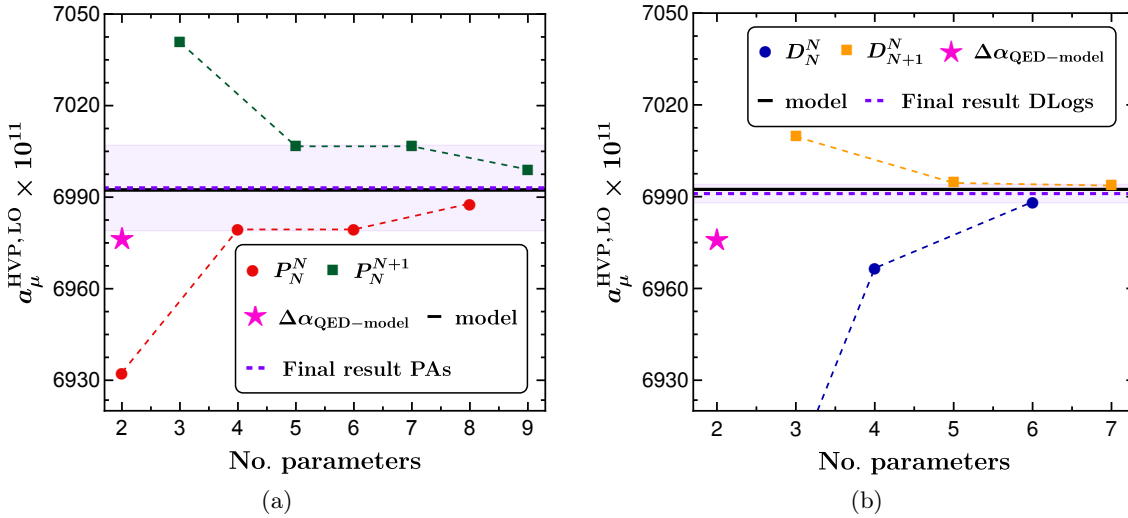


Figure 4.5: Estimated values for $a_\mu^{\text{HVP,LO}}$ from (a) PAs and (b) D-Logs fitted to a data set with zero error. The pink star is the value obtained from the model of Eq. (4.27) and the purple dashed line is the final result coming from the (a) PAs and (b) D-Logs with the light purple band representing the systematic error of the result. The black line indicates the true value of the model given in Eq. (4.19).

advantage of the expected convergence of the PA sequences dictated by Eq. (4.11). It is expected that the higher-order PAs will be closer to the true value. We can then take the average of the highest-order approximants of each sequence only, i.e. P_2^2 and P_2^3 , since from the convergence behavior of Eq. (4.11), we expect the true value to lie between these two PAs estimates. Thus, computing this mean we get $a_{\mu, \text{PAs}}^{\text{HVP,LO}} = 6993 \times 10^{-11}$, that presents an error of less than 0.01% with respect to the model value. This result can be seen in Fig. 4.5a as the purple dashed line.

One can also estimate a theoretical uncertainty due to the truncation of the PAs sequences. Taking the convergence pattern of Eq. (4.11) into consideration, the error will be defined as half of the distance between the two highest-order PAs (P_2^2 and P_2^3 in this case), which gives us a relative error of 0.19% represented in Fig. 4.5a by the light-purple band. This systematic error has to be added to our final numbers in the spirit of a conservative estimate.

A similar analysis can be performed with D-Logs. As argued in the previous section, they introduce branch cuts thus speeding the convergence, a key factor when dealing with a small number of parameters. In this case, we will use the approximants of the sequences D_N^N and D_{N+1}^N , since these are the sequences expected to bound the original function, as indicated in Eq. (4.12). To construct fitting functions for D-Logs, we start with an arbitrary

Table 4.2: D-Log fitting functions in terms of t or x variable.

	$D_M^N(t)$	$D_M^N(x)$
D_2^1	$\frac{-f_0 t}{(r_1-t)^{\gamma_1}}$	$\frac{f_0 m_\mu^2 x^2 (1-x)^{-1+\gamma_1}}{(r_1-r_1x+m_\mu^2 x^2)^{\gamma_1}}$
D_2^2	$\frac{-f_0 t e^{\beta t}}{(r_1-t)^{\gamma_1}}$	$\frac{f_0 m_\mu^2 x^2 (1-x)^{-1+\gamma_1}}{(r_1-r_1x+m_\mu^2 x^2)^{\gamma_1}} e^{\beta \frac{m_\mu^2 x^2}{(x-1)}}$
D_3^2	$\frac{-f_0 t}{(r_1-t)^{\gamma_1} (r_2-t)^{\gamma_2}}$	$\frac{f_0 m_\mu^2 x^2 (1-x)^{-1+\gamma_1+\gamma_2}}{(r_1-r_1x+m_\mu^2 x^2)^{\gamma_1} (r_2-r_2x+m_\mu^2 x^2)^{\gamma_2}}$
D_3^3	$\frac{-f_0 t e^{\beta t}}{(r_1-t)^{\gamma_1} (r_2-t)^{\gamma_2}}$	$\frac{f_0 m_\mu^2 x^2 (1-x)^{-1+\gamma_1+\gamma_2}}{(r_1-r_1x+m_\mu^2 x^2)^{\gamma_1} (r_2-r_2x+m_\mu^2 x^2)^{\gamma_2}} e^{\beta \frac{m_\mu^2 x^2}{(x-1)}}$

Taylor series in the t variable up to order $N + M$, compute its logarithm derivative, as indicated in Eq. (2.26) –recall that it is equivalent to taking the ratio f'/f –. After that, we construct a PA, \bar{P}_M^N , and then we unfold this process using Eq. (2.27), thus obtaining the D-Log expression in terms of t . Finally, we perform the change of variables of Eq. (4.9) and write the generic fitting function in terms of x . For instance, the simplest D-Log is $D_2^1(t)$ that before and after the change of variables reads

$$D_2^1(t) = \frac{-f_0 t}{(r_1-t)^{\gamma_1}} \rightarrow D_2^1(x) = \frac{f_0 m_\mu^2 x^2 (1-x)^{-1+\gamma_1}}{(r_1-r_1x+m_\mu^2 x^2)^{\gamma_1}}, \quad (4.25)$$

with fit parameters f_0, r_1 , and γ_1 . We recall D_M^N requires $N + M$ fitted parameters. The next approximant is the $D_2^2(t)$

$$D_2^2(t) = \frac{-f_0 t e^{\beta t}}{(r_1-t)^{\gamma_1}} \rightarrow D_2^2(x) = \frac{f_0 m_\mu^2 x^2 (1-x)^{-1+\gamma_1}}{(r_1-r_1x+m_\mu^2 x^2)^{\gamma_1}} e^{\beta \frac{m_\mu^2 x^2}{(x-1)}}, \quad (4.26)$$

with fit parameters f_0, r_1, γ_1 , and β . The fitting functions used in this analysis adhere to the structure proposed in Eq. (3.6), making it advantageous to reparameterize them using new coefficients rather than the original Taylor series coefficients. All sequences of D-Logs employed to fit the data are presented in Table 4.2. The table provides a comprehensive overview of the functions used for fitting, including their respective parameters: r_n , which denotes the branch point in the t -variable; γ_n , which specifies the multiplicity of the corresponding cut; β , an exponential factor exclusive to the diagonal sequence; and f_0 , a normalization factor.

A comparison of the results for $a_\mu^{\text{HVP, LO}}$ obtained from the D-Log approximants is found in Fig. 4.5b where we show both sequences, D_N^N and D_{N+1}^N as a function of the number,

$N + M$, of fitted coefficients. Convergence for D-Logs is faster than PAs, especially for the subdiagonal sequence. In line with the criteria used for PAs, we employ D_3^2 and D_3^3 to obtain a final prediction for $a_\mu^{\text{HVP,LO}}$ from the D-Logs. Computing the mean of these values, we obtain $a_{\mu, \text{DLogs}}^{\text{HVP,LO}} = 6991.4 \times 10^{-11}$, which exhibits an error of less than 0.02% compared to the model value and a theoretical uncertainty band of less than 0.05% (light-purple band in Fig. 4.5b).

An important outcome of analyzing data with no errors is to provide an estimate of the theoretical uncertainty for other models proposed in the literature to fit and extrapolate the MUonE data. Let us take a closer look at the model proposed by Abbiendi in the Letter of intent of the MUonE experiment, Ref. [120], motivated by the one-loop QED calculation of the vacuum polarization. This fitting function is

$$\Delta\alpha_{\text{QED-model}}(t) = KM \left[-\frac{5}{9} - \frac{4M}{3t} + \left(\frac{4M^2}{3t^2} + \frac{M}{3t} - \frac{1}{6} \right) \frac{2}{\sqrt{1 - \frac{4M}{t}}} \log \left| \frac{1 - \sqrt{1 - \frac{4M}{t}}}{1 + \sqrt{1 - \frac{4M}{t}}} \right| \right], \quad (4.27)$$

where the parameters K and M are determined by the fit.

After the \mathcal{Q}^2 minimization we obtain $\mathcal{Q}^2 = 1.84 \times 10^{-4}$ and the parameters determined by the fit are: $K = 6865.36 \text{ GeV}^{-2}$ and $M = 0.06 \text{ GeV}^2$. The $a_\mu^{\text{HVP,LO}}$ value can be predicted by this model employing the expression above in Eq. (4.7), which in this scenario gives us $a_{\mu, \text{QED-model}}^{\text{HVP,LO}} = 6976 \times 10^{-11}$. Even though this function has only two parameters, as in the case of $P_1^1(x)$, this model implements the logarithmic dependency expected at large $|t|$, which facilitates a better approximation to the exact result. Thus, it is expected that $\Delta\alpha_{\text{QED-model}}(t)$ has a more accurate result than $P_1^1(x)$, which can be verified in Fig. 4.5a where the pink star represents the prediction of $\Delta\alpha_{\text{QED-model}}$. Regarding the D-Logs, $D_1^1(t)$, which contains only two parameters, is unable to reproduce any type of singularity, whether poles or cuts. Therefore one would not expect that its estimate of $a_\mu^{\text{HVP,LO}}$ be more precise than the one provided by the QED-inspired model, which is corroborated by Fig. 4.5b. The next D-Log, $D_2^1(t)$, with three parameters, contains a branch cut and achieves a relative error of 0.24% when compared to the true value of our model, Eq. (4.19), an error very similar to one obtained from $\Delta\alpha_{\text{QED-model}}$, but using our model-independent method. When comparing it, however, to our final estimate from the PAs or D-Logs given in Figs. 4.5a and 4.5b, respectively, the result from the use of $\Delta\alpha_{\text{QED-model}}$ differs significantly more from the true model value of Eq. (4.19). A priori knowledge of the function has been used when defining the QED-model in Eq. (4.27). Even though the logarithmic dependence is captured, the value of the fitted parameter M departs from the true one, $m_\pi^2 \sim 0.02 \text{ GeV}^2$. The accuracy of the result is thus model-dependent and the systematic error is difficult to quantify. Whether the QED-model in Eq. (4.27) would perform similarly with real data

cannot be answered with guarantees.

As mentioned above, we can estimate the theoretical uncertainty in using $\Delta\alpha_{\text{QED-model}}$ as the relative difference between the fitted value and the true model value given in Eq. (4.19). This gives us 0.24%, which is slightly larger than, but of the same order of, the one obtained with our PA method. The systematic error from the use of $\Delta\alpha_{\text{QED-model}}$ is, however, significantly larger than that of the D-Log approach. As already stated, these systematic uncertainties have to be considered in the final estimates of $a_\mu^{\text{HVP,LO}}$ regardless of the fitting function used.

4.5 approximants to data with realistic errors

We can now move to more realistic data sets, with fluctuations and uncertainties of the same order as those expected to be obtained in the MUonE experiment [118–120, 122, 126–128]. We built 1000 toy data sets for the function $\alpha \Delta\alpha_{\text{had}}(x) \times 10^5$ employing the model of Eq. (4.15) with 30 data points each, corresponding to the expected MUonE bin sizes. The 30 values of x are computed in the same way as in the previous section. The data sets were generated assuming a Gaussian distribution around the value of $\alpha \Delta\alpha_{\text{had}}(x) \times 10^5$ given by the model of Eq. (4.15) with an error ranging from 0.7%, for larger values of x , up to 6.7% for $x \approx 0.2$.² Additionally, the $a_\mu^{\text{HVP,LO}}$ of each data set was calculated: the data was used in the region $x \in [0.2, 0.93]$, and the model of Section 4.2, used in the data generation, was employed outside this interval. Calculating the median and the 68% confidence level (CL) of this distribution we get

$$a_\mu^{\text{HVP,LO}} = (6991_{-20}^{+22}) \times 10^{-11} \quad (\text{model value}). \quad (4.28)$$

Since in this case the extrapolation outside the data region is exact, this value gives an idea of the best possible result that we can expect from our PA or D-Log predictions given the available information in the data sets.

For each data set, the parameters b_n of the PAs and $f_0, \beta, r_n, \gamma_n$ of the D-Logs are determined by a χ^2 minimization. We apply penalizations if the result for the Taylor series coefficients a_n of $\Delta\alpha_{\text{had}}$ do not follow the expected hierarchy given in Eq. (4.14) or the determinant condition discussed in Section 2.1.3. This is done by employing a modified χ^2

²Members of MUonE team; Giovanni Abbiendi, Carlo Carloni Calame, and Graziano Venanzoni provide us with the values of the expected uncertainties of the MUonE experiment.

function given by

$$\chi^2 = \sum_{i,j=1}^{30} [\alpha \Delta\alpha_{\text{had}}(x_i) \times 10^5 - \mathcal{P}_N^M(x_i)] (C^{-1})_{ij} [\alpha \Delta\alpha_{\text{had}}(x_j) \times 10^5 - \mathcal{P}_N^M(x_j)] \\ + n_{\text{dof}} \left[\sum_{i=2}^{N+M} \theta(a_i - a_{i-1}) + \sum_{i=3}^{N+M} \theta(\mathcal{D}_{i-1,1}) + \sum_{i=5}^{N+M} \theta(-\mathcal{D}_{i-2,2}) \right], \quad (4.29)$$

where C is the data covariance matrix, n_{dof} is the number of degrees of freedom, $\theta(x)$ is the Heaviside theta function and $\mathcal{D}_{m,n}$ is the determinant given in Eq. (2.12). The χ^2 penalties are scaled by n_{dof} to be of a natural size. Hence, if the hierarchy of a_i coefficients or the determinant conditions are not satisfied, the χ^2 has a steep increase which forces the minimization algorithm to search for minima respecting the conditions expected for Stieltjes functions. The arguments inside $\theta(x)$ are always written in terms of the fit parameters of each approximant. Alternatively, one could neglect the second line from Eq. (4.29) and turn the aforementioned penalization into limits for the fit parameters. Both strategies lead to equivalent results.

For each fit, the approximant written as a function of the variable t is examined for the appearance of defects. As already explained in Sec. 4.4, there is no guarantee that numerical defects will not occur when approximants are used as fitting functions to real data. In PAs, defects are manifest in a nearly exact cancellation between a pole and a zero of the approximant. Their presence effectively decreases the order of the PA, which spoils the systematic study of the convergence of a given sequence. For the D-Logs, a similar effective reduction in the order of the approximants can happen in several circumstances. If the exponent of a cut, γ_n , is compatible with zero, this reduces the number of fitted coefficients by two (This case corresponds precisely to the defects that occur in the intermediate PA \bar{P}_M^N). Other defects, more of a numerical nature could occur in D-Logs as fitting functions; for example, if two branch points are equal, i.e. $r_i = r_j$ ($i \neq j$), the two cuts are merged, again lowering the number of coefficients by two. In the case of the diagonal D-Logs, the exponential coefficient, β , may be compatible with zero within errors, reducing in practice the approximant by one order (see Table 4.2 for the explicit D-Log expressions). Finally, if $\sum_n \gamma_n = 1$, the pole at $x = 1$, resulting from the change of variable described in Eq. (4.9), is lost.

In summary, those approximants with numerical defects are discarded because they are redundant with lower order ones. For instance, for the PA P_2^2 approximately 30% of the fits have to be disregarded due to the presence of defects, and for P_2^3 this number is 56%.

In the case of D-Logs, 0.7% of fits for D_3^2 and 4% for D_3^3 are not considered³.

A related issue appears in fits where one of the parameters turns out to be almost zero without numerical cancellation. In our fits, this happens when using the PA P_2^2 as a fitting function for several of the data sets.⁴ This may be problematic since, with one of the parameters in the denominator equal to zero, this approximant is effectively reduced to P_1^2 . To circumvent this issue, in our results for P_2^2 , we impose that none of the parameters are zero, even if this leads to a larger χ^2 , which guarantees that we do not mix results from different approximants in the final statistical distributions.

After fitting, we use the resulting approximant to calculate $a_\mu^{\text{HVP,LO}}$ for each of the accepted fits using Eq. (4.7) (or with Eq. (4.10), for the partial contributions). It is also possible to use the approximants only to extrapolate the data, i.e. use the data points to obtain $a_\mu^{\text{HVP,LO}}$ in the region $x \in [0.2, 0.93]$ and then apply the approximants only outside this interval. The results from both procedures are in very good agreement, since the fit quality is almost always excellent, which is confirmed by Fig. 4.6 and the χ^2 values of Tab. 4.3. The results from each \mathcal{P}_M^N are then obtained as follows: the central value for $a_\mu^{\text{HVP,LO}}$ is the median of the distribution of the results and the uncertainty is obtained within a 68% confidence level (CL).

Given the size of the errors present in the data sets, now we are only able to obtain meaningful results from approximants with at most 6 fit parameters, which corresponds to the PAs $P_1^1(x)$, $P_1^2(x)$, $P_2^2(x)$, and $P_2^3(x)$, and the D-Logs $D_2^1(x)$, $D_2^2(x)$, $D_3^2(x)$, and $D_3^3(x)$. Higher-order approximants have an excessive number of parameters to fit which leads to gigantic uncertainties and unstable results. As an example of typical fit outcomes, for one of the 1000 data sets, we compare in Fig. 4.6 the data and the four PAs obtained after fitting to these data. We can notice that all approximants fit the data very well and no significant deviation between the approximants is present in the region where data is available. Similar results are found for D-Logs. Discrepancies in the region where extrapolation is necessary are, however, non-negligible. As discussed in Secs. 4.1 and 4.3, the change of variable from t to x masks the fact that there is a significant extrapolation being performed and the integration from $x \approx 0.93$, where the data ends, to $x = 1$ still gives an important contribution to $a_\mu^{\text{HVP,LO}}$.

Before turning to our final numbers, it is instructive to examine the results from each

³When we inspect the approximants for the appearance of these defects, we employ a numerical tolerance of 10^{-4} . This number is somewhat arbitrary, and we have checked that varying it by one order of magnitude does not alter the results significantly.

⁴This only happens for P_2^2 and this is not observed when fitting the data without fluctuations, which indicates that this is an artifact related to the statistical errors.

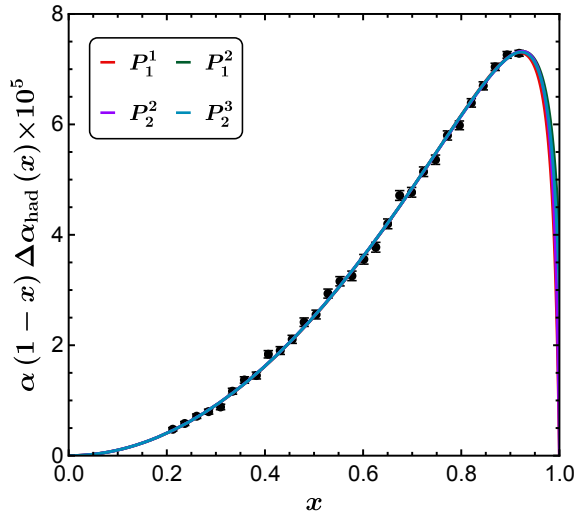


Figure 4.6: Fitted PAs to the integrand $\alpha(1-x)\Delta\alpha_{\text{had}}(x)$ from Eq. (4.7). Black points show one toy data set used in the current exercise.

approximant separately. We give in Tab. 4.3 the values for $a_\mu^{\text{HVP,LO}}$ obtained after fitting each PA and D-Log to the 1000 toy data sets, together with the median of the reduced χ^2 (and its 68% CL). One can notice that the pattern of convergence of Eqs. (4.11) and (4.12) is obeyed for the central values obtained from the PAs and D-Logs, as already happened in the idealized case of Sec. 4.4. It is also possible to note from Tab. 4.3 that the uncertainty of $a_\mu^{\text{HVP,LO}}$ from P_1^2 is much larger than the other PA's predictions. This can be understood by the fact that this approximant is not a Stieltjes function, as discussed in Sec. 2.1.3. Results from P_1^2 can, therefore, be safely discarded when confronted with the others. Finally, we observe that the uncertainty of $a_\mu^{\text{HVP,LO}}$ increases from P_2^2 to P_2^3 as well as from D_3^2 to D_3^3 and we could not obtain meaningful fits for P_3^3 and D_4^3 . These are indications that we are at the limit of what can be done with the toy data sets given the size of the errors expected by the MUonE experiment.

The results from Tab. 4.3 show a somewhat large uncertainty. This uncertainty stems mostly from the extrapolation, i.e. deviations of different approximants outside the data region, corresponding to $t \in (-\infty, -0.138] \text{ GeV}^2$. To quantify the error from this extrapolation, we calculated the partial contributions $a_\mu^{\text{HVP,LO}}(x_{\text{max}})$ up to x_{max} , defined in Eq. (4.10), with $x_{\text{max}} \in [0.990, 1]$. It is expected that by restricting the extrapolation to a smaller interval, the final errors will be smaller. For example, with $x_{\text{max}} = 0.990$ one can cover 99.1% of the value of $a_\mu^{\text{HVP,LO}}$, which may be an acceptable trade-off if the uncertainties are significantly reduced. The remaining 0.9% would have to be obtained

Table 4.3: Results for $a_\mu^{\text{HVP,LO}}$ from the PAs and D-Logs used as fitting functions to toy data sets together with the final values for χ^2/n_{dof} of the respective approximants. Final results for both methods are also presented.

	$a_\mu^{\text{HVP,LO}} \times 10^{11}$	χ^2/n_{dof}		$a_\mu^{\text{HVP,LO}} \times 10^{11}$	χ^2/n_{dof}
P_1^1	6938 ± 21	$1.01^{+0.27}_{-0.25}$	D_2^1	7052^{+66}_{-71}	$1.01^{+0.26}_{-0.26}$
P_1^2	7042^{+114}_{-104}	$1.01^{+0.28}_{-0.26}$	D_2^2	6956^{+96}_{-65}	$1.05^{+0.28}_{-0.27}$
P_2^2	6980^{+46}_{-34}	$1.05^{+0.29}_{-0.27}$	D_3^2	6999^{+48}_{-39}	$1.10^{+0.29}_{-0.28}$
P_2^3	6994^{+85}_{-49}	$1.11^{+0.29}_{-0.31}$	D_3^3	6977^{+72}_{-53}	$1.14^{+0.30}_{-0.29}$
Final result	6987^{+46}_{-34}	—	Final result	6988^{+48}_{-39}	—

externally by matching to perturbative QCD or lattice data if available at similar precision, for example.

The $a_\mu^{\text{HVP,LO}}(x_{\text{max}})$ values estimated for $x_{\text{max}} = \{0.990, 0.995, 0.997, 1\}$ are illustrated for the PAs in Fig. 4.7 and for the D-Logs in Fig. 4.8. The pattern of convergence is evident for all x_{max} in Figs. 4.7 and 4.8, where the gray band is the expected model value of $a_\mu^{\text{HVP,LO}}(x_{\text{max}})$ given by Eq. (4.15). The red points in Fig. 4.7 represent the P_N^N sequence and the green ones P_N^{N+1} . In Fig. 4.8, the blue points show the D_N^N sequence while results for D_{N+1}^N appear in yellow. One can observe in the results of these figures that the uncertainty steadily increases with x_{max} , which reflects the dispersion due to extrapolation outside the data region.

We can then obtain a final value for $a_\mu^{\text{HVP,LO}}(x_{\text{max}})$. Since with both PA and D-Logs the approximants from the two sequences are expected to bound the true value, it is natural to use the average of the highest-order approximants, in this case P_2^2 and P_2^3 , on the one hand, and D_3^2 and D_3^3 on the other, as the central value for the final estimate. We will consider the final statistical uncertainty to be the smallest between each pair of approximants. This can be considered conservative since we do not reduce the final error, as would be done in a weighted average, due to the expected strong correlations between the two results. It is important to mention that we book the error stemming from the extrapolation –which is the dominant source of error– as part of the statistical uncertainty since, ultimately, this error is rooted in the statistical fluctuations of the data. Finally, for the systematic uncertainty we use half the interval spanned by the central values from the two highest-order approximants. Our final estimates for PAs and D-Logs for the different values of x_{max} are collected in Tab. 4.4 –second and third columns, respectively– where “stat” and “sys” refer

Table 4.4: Final results for $a_\mu^{\text{HVP, LO}}(\pm\text{stat})(\pm\text{sys})$ in units of 10^{11} for PAs, D-Logs and the QED-model. “stat” and “sys” refer to the statistical and systematic uncertainties, respectively.

x_{max}	$a_{\mu, \text{PAs}}^{\text{HVP, LO}}$	$a_{\mu, \text{Dlogs}}^{\text{HVP, LO}}$	$a_{\mu, \text{QED-model}}^{\text{HVP, LO}}$	$a_{\mu, \text{data-sets}}^{\text{HVP, LO}}$
0.990	6927 $\begin{pmatrix} +33 \\ -27 \end{pmatrix} (\pm 4)$	6928 $\begin{pmatrix} +36 \\ -31 \end{pmatrix} (\pm 4)$	6918 $\begin{pmatrix} +21 \\ -20 \end{pmatrix} (\pm 4)$	6926 $\begin{pmatrix} +22 \\ -20 \end{pmatrix}$
0.995	6967 $\begin{pmatrix} +40 \\ -31 \end{pmatrix} (\pm 5)$	6970 $\begin{pmatrix} +42 \\ -34 \end{pmatrix} (\pm 7)$	6959 $(\pm 21)(\pm 17)$	6969 $\begin{pmatrix} +22 \\ -20 \end{pmatrix}$
0.997	6978 $\begin{pmatrix} +43 \\ -33 \end{pmatrix} (\pm 5)$	6981 $\begin{pmatrix} +43 \\ -38 \end{pmatrix} (\pm 9)$	6971 $(\pm 21)(\pm 17)$	6982 $\begin{pmatrix} +22 \\ -20 \end{pmatrix}$
1.000	6987 $\begin{pmatrix} +46 \\ -34 \end{pmatrix} (\pm 7)$	6988 $\begin{pmatrix} +48 \\ -39 \end{pmatrix} (\pm 11)$	6980 $(\pm 21)(\pm 17)$	6991 $\begin{pmatrix} +22 \\ -20 \end{pmatrix}$

to the statistical (in the sense explained above) and systematic uncertainties. These final estimates are also illustrated in Figs. 4.7 and 4.8 by the black dots.

As one can notice, our final results are in excellent agreement with the expectation from the model we used (fifth column of Tab. 4.4), with the central values for $a_\mu^{\text{HVP, LO}}$ off by at most 0.06% in the case of PAs and 0.05% in the case of D-Logs. Uncertainties are dominated by statistics and the extrapolation (which we book as “stat”). A reduction in the uncertainty of about 25% in both methods is achieved by computing the integral up to $x = 0.990$, which covers 99.1% of $a_\mu^{\text{HVP, LO}}$. This is very likely an acceptable compromise since estimating the remaining 0.9% from e^+e^- data or perturbative QCD would not increase the uncertainties in any significant way. Finally, we observe that the systematic uncertainties, which are small, do not change significantly with x_{max} .

For comparison, we also employ the QED-inspired model of Eq. (4.27) to perform the fits to the toy data sets. For every data set a value for the parameters K and M is determined as well as a prediction for $a_\mu^{\text{HVP, LO}}(x_{\text{max}})$, obtained by using the fitting function to compute the integral of Eq. (4.10). We again quote the median as the central value with an uncertainty obtained within its 68% CL. The predictions for the different x_{max} are indicated in Tab. 4.4, where the systematic error is determined as 0.24% of the central value, as explained in Sec. 4.4. These values can be seen in Figs. 4.7 and 4.8 represented by the pink star with the inner error band representing solely the statistical uncertainty and the larger error band representing the total uncertainty, from the sum in quadrature of the two error sources in Tab. 4.4. The QED-inspired model, which has only two free parameters, clearly outperforms P_1^1 , which also has only two free parameters. This is certainly a result of the additional structure of the model, that contains, for example, a logarithmic cut. On the other hand, the result from the model underestimates the true value, which reflects a

systematic uncertainty associated with the model dependency, something already observed in Sec. 4.4. The model dependency can be inferred from the fitted values of K and M which read $6871_{-38}^{+43} \text{ GeV}^{-2}$ and $0.060_{-0.003}^{+0.004} \text{ GeV}^2$, respectively. In particular, the value of M is incompatible with m_π^2 , as would be expected from the model in Eq. (4.15). In comparison with the final result from the PAs and D-Logs, the model displays a smaller uncertainty, which stems from the fact that it has only two free parameters, but is further away from the true value. In this respect, the use of PAs and D-Logs helps reducing the final systematic uncertainty, being, in addition, completely model independent.

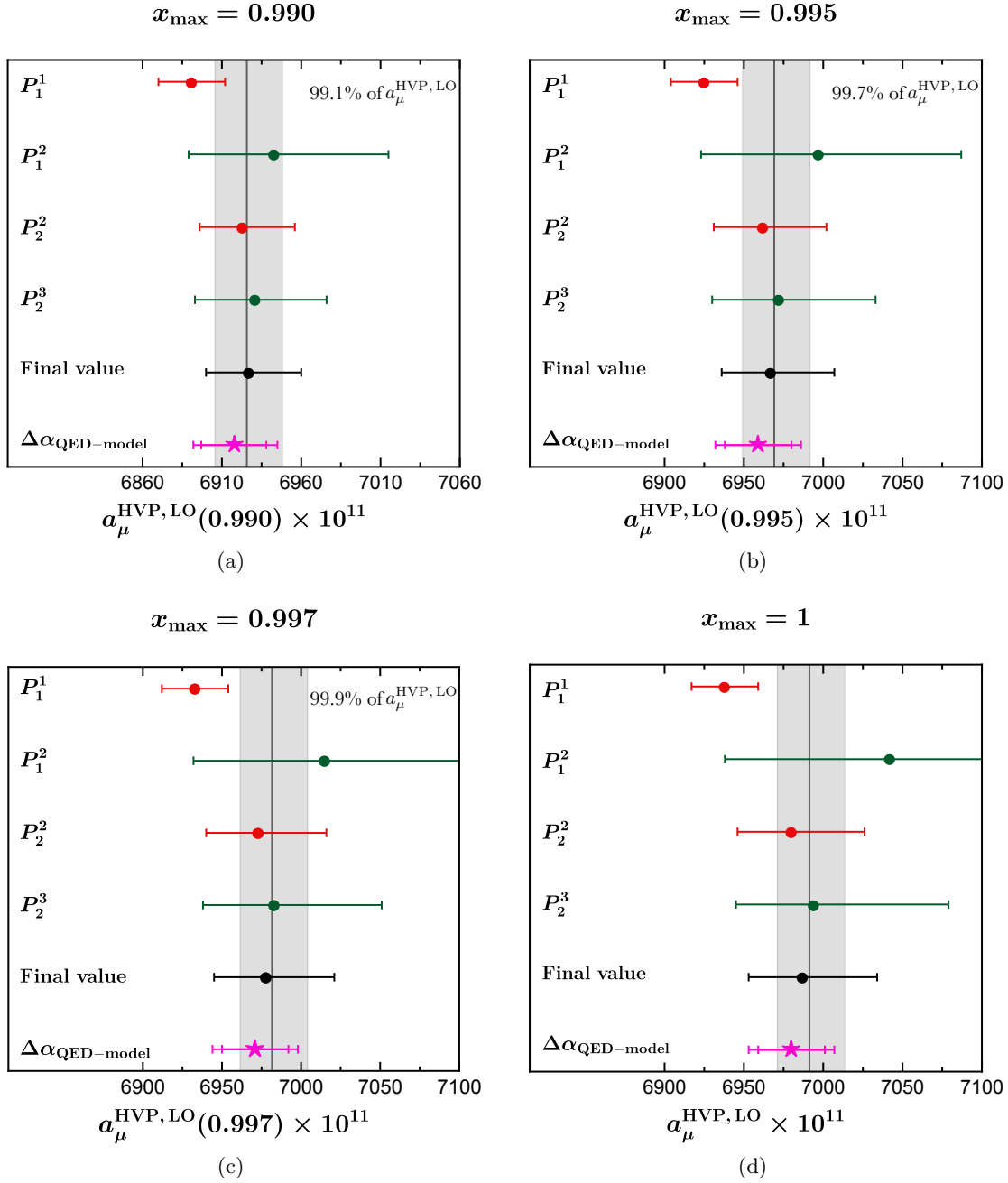


Figure 4.7: $a_\mu^{\text{HVP,LO}}(x_{\text{max}})$ from PAs fitted to the toy data sets for four different values of x_{max} : (a) $x_{\text{max}} = 0.990$ ($t_{\text{max}} = -1.1 \text{ GeV}^2$), (b) $x_{\text{max}} = 0.995$ ($t_{\text{max}} = -2.2 \text{ GeV}^2$), (c) $x_{\text{max}} = 0.997$ ($t_{\text{max}} = -3.7 \text{ GeV}^2$) and (d) $x_{\text{max}} = 1$. The PAs P_N^N are shown in red while P_N^{N+1} appear in green. Final results obtained from the approximants appear as a black dot and results from the QED-inspired model of Eq. (4.27) as a pink star. The inner error bar in the QED model result represents the statistical uncertainty. The gray band gives $a_\mu^{\text{HVP,LO}}(x_{\text{max}})$ with exact extrapolation using the model of Eq. (4.15).

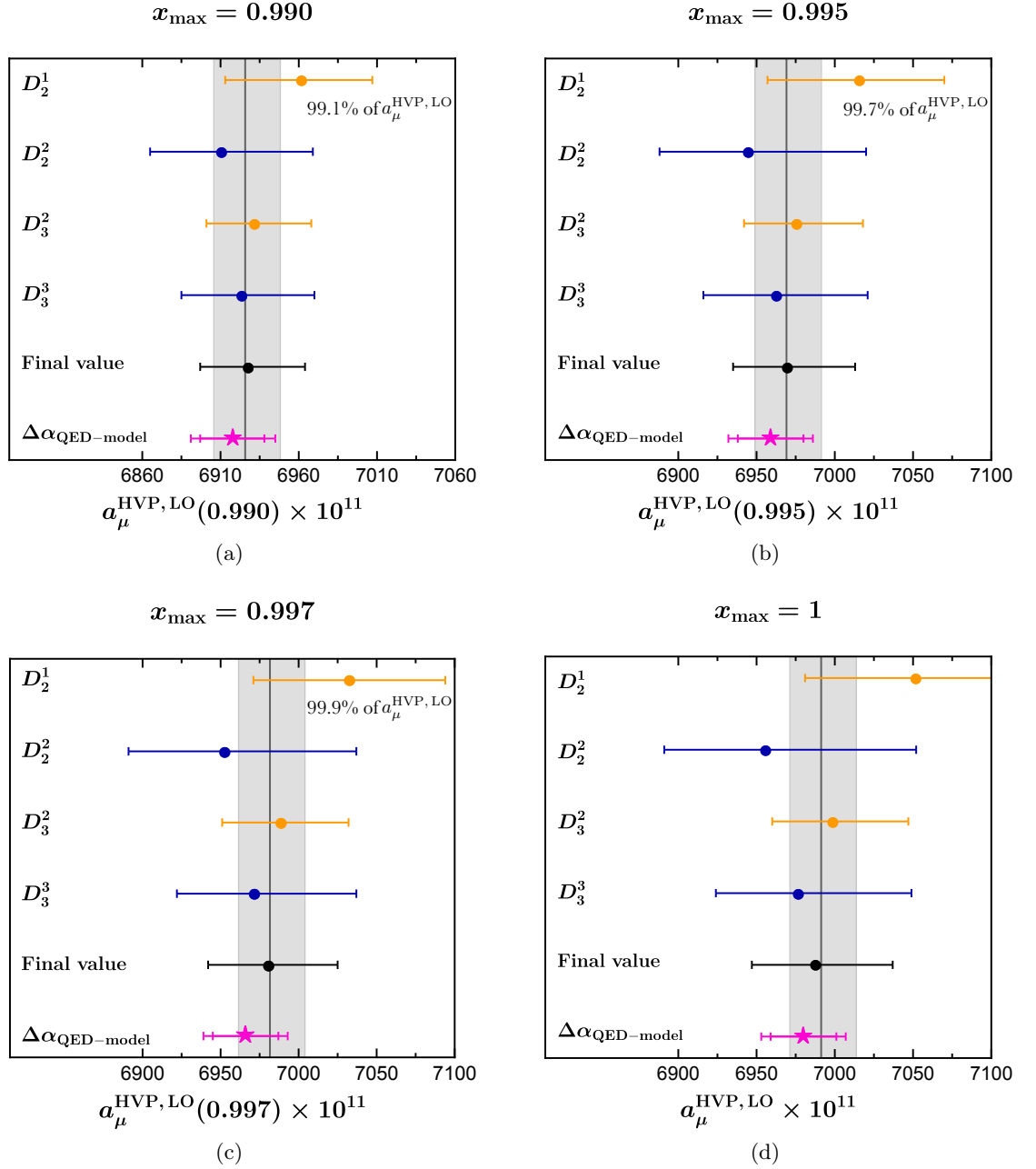


Figure 4.8: $a_\mu^{\text{HVP, LO}}(x_{\text{max}})$ from D-Logs fitted to the toy data sets for four different values of x_{max} : (a) $x_{\text{max}} = 0.990$ ($t_{\text{max}} = -1.1 \text{ GeV}^2$), (b) $x_{\text{max}} = 0.995$ ($t_{\text{max}} = -2.2 \text{ GeV}^2$), (c) $x_{\text{max}} = 0.997$ ($t_{\text{max}} = -3.7 \text{ GeV}^2$) and (d) $x_{\text{max}} = 1$. The D-Logs D_N^N are shown in blue while D_{N+1}^N appear in yellow. Final results obtained from the approximants appear as a black dot and results from the QED-inspired model of Eq. (4.27) as a pink star. The inner error bar in the QED model result represents the statistical uncertainty. The gray band gives $a_\mu^{\text{HVP, LO}}(x_{\text{max}})$ with exact extrapolation using the model of Eq. (4.15).

4.6 Summary & highlights

In all this chapter, we described the use of PAs and D-Logs to fit and extrapolate toy data reflecting the expected results of the future MUonE experiment. This is a model-independent strategy to extract $a_\mu^{\text{HVP,LO}}$ that relies on general knowledge about the fundamental properties of the hadronic contribution to the running of the fine-structure constant, which is a Stieltjes function in the variable t [134]. These type of functions are ruled by a determinant condition, given in Eq. (2.12), which generates constraints for their Taylor series coefficients. This is a key factor, since the convergence of rational approximants built from the Taylor series of Stieltjes functions is guaranteed by theorems in a very specific pattern (see Section 2.1.3), where the PAs and D-Logs belonging to the diagonal sequence approach $\Delta\alpha_{\text{had}}(t)$ from below while the PAs of the sequence $P_N^{N+1}(t)$ and the D-Logs of the sequence $D_{N+1}^N(t)$ do so from above, as indicated in Eqs. (4.11) and (4.12).

In our case, the approximants are used as fitting functions that would be employed to fit the future MUonE data. Our fitting functions were constructed as follows. First, the approximants were formally built with the canonical procedure, i.e. by matching to the Taylor series of $\Delta\alpha_{\text{had}}(t)$ around $t = 0$, with generic Taylor coefficients that would be fixed by the data. Then, the function in the variable x , which is more suited for fits in the MUonE framework, was obtained by the change of variables of Eq. (4.9). These new functions in x are then used to fit the toy data sets in order to determine $a_\mu^{\text{HVP,LO}}$, by employing the results from the approximant in the integral of Eq. (4.7) and, as a by product, to estimate the Taylor coefficients of $\Delta\alpha_{\text{had}}(t)$. The toy data sets used in this work were generated from the model for the Euclidean correlator proposed by Greynat and de Rafael in Ref. [123], briefly motivated in Sec. 4.2. We believe this simple model to be sufficient for our purposes since it captures the main features of $\Delta\alpha_{\text{had}}(t)$ and is a Stieltjes function.

First we showed, as proof of concept, how sequences of approximants bound the true value of $a_\mu^{\text{HVP,LO}}$ in idealized scenarios with no fluctuations in the data sets. We then turned to tests of our method in the realistic case, where the toy data sets are generated from the model with fluctuations that reflect the expected uncertainties to be obtained from the MUonE experiment. We produced 1000 data sets and fitted them with the PAs P_1^1, P_1^2, P_2^2 , and P_2^3 , and the D-Logs D_2^1, D_2^2, D_3^2 , and D_3^3 . The constraints imposed on the Taylor series coefficients, derived from the determinant condition of Eq. (2.12) and given in Eq. (4.14), were imposed on the fits. We analyzed then the estimate of $a_\mu^{\text{HVP,LO}}(x_{\text{max}})$ for each approximant up to $x_{\text{max}} = 0.990, 0.995, 0.997$ and 1. Taking advantage of the expected convergence pattern, i.e. the fact that different sequences bound the true value

as in Eqs. (4.11) and (4.12), we obtained the final estimate of $a_\mu^{\text{HVP,LO}}(x_{\text{max}})$. Our final results are obtained from the average between the two highest-order approximants of each sequence, in concrete, the PAs P_2^2 and P_2^3 and the D-Logs D_3^2 and D_3^3 . The systematic uncertainty of our final prediction can be estimated and it was calculated as half of the difference between these two approximants while the statistical error was taken as the smallest error among the highest-order approximants of each sequence.

For all the values of x_{max} employed, our final estimates are fully compatible with what was expected from the underlying model, as one can see in Figs. 4.7 and 4.8 for the PAs and D-Logs respectively. Our final central values differ from the expected ones by less than 0.06% in the PAs case and 0.05% for D-Logs. The final uncertainty is, in all cases, dominated by the uncertainty stemming from the extrapolation. We observe, however, that when the region in which we extrapolate the results is expanded, the dispersion between different fits grows, leading to larger final uncertainties. This can certainly be expected since the extrapolation that is performed is far from trivial and relies on data in a very limited region of the variable t . In this respect, an extrapolation in a somewhat limited interval, with $x_{\text{max}} = 0.990$ for example, which covers 99.1% of the $a_\mu^{\text{HVP,LO}}$ integrand, significantly reduces the final uncertainty. Of course, in this case one needs to resort to external information to complete the determination of $a_\mu^{\text{HVP,LO}}$.

We also compared our final prediction with the ones obtained from the QED-inspired model of Eq. (4.27) used in preliminary studies of the MUonE proposal [120]. This model leads to smaller uncertainties than those obtained from our procedure, in part because it has only two parameters, but its central value is further away from the true value, as seen in Figs. 4.7 and 4.8. This larger systematic uncertainty reflects a model dependency that can hardly be avoided with functions of this type.

V_{ub} determination

Within the frame of the Standard Model (SM), the electroweak gauge symmetry $SU(2)_L \times U(1)_Y$ is in charge of flavour physics phenomena for quarks and leptons. This research field is crucial for understanding the dynamics of all particles under the weak force. A significant focus of flavour physics is the study of hadrons, their properties, and their decays into other particles. These decays are not only sensitive to the parameters of the SM but also to potential new physics beyond the SM (BSM). By examining these processes with high precision, it is possible to reveal subtle discrepancies between SM predictions and experimental results, which may indicate the presence of new particles or interactions.

A cornerstone for understanding flavour-changing processes is the Cabibbo-Kobayashi-Maskawa (CKM) matrix [32, 33], which encodes the probabilities of transitions between different types of quarks. Indeed, this mixing-matrix correspond to a 3×3 complex matrix whose elements are denoted by V_{ij} for a transition of a j -down-type quark (d, s, b) to a i -up-type quark (u, c, t). The precise determination of CKM matrix elements, is essential not only for testing the internal consistency of the SM but also for exploring the potential existence of physics beyond it [136–138]. For instance, CKM matrix must satisfy unitarity, *i.e.* $\sum_i V_{ij} V_{ik}^* = \delta_{jk}$ and $\sum_j V_{ij} V_{kj}^* = \delta_{ik}$, therefore violations of unitarity condition are evidence of physics BSM.

There are many processes where to test the CKM matrix and extract its elements. Among them, purely leptonic weak decays, *e.g.* $P^- \rightarrow \ell^- \bar{\nu}_\ell$ with $P = \{\pi, K, D, B\}$, offer (in general) a theoretically clean environment for the determination of the CKM elements

more advantageous than the semileptonic ones,¹ where the decay rates depend on hadronic information that is encoded in form factors. In addition, both leptonic and semileptonic decays offer an opportunity to test lepton flavor universality as ℓ can be e, μ or τ . The current status of the magnitude of the CKM matrix elements and future prospects for improving their determination can be found in the Particle Data Group [140] as well in the Flavour Lattice Averaging Group (FLAG) report [139] (see also Ref. [141]).

$$|V_{ud}| = 0.97367 \pm 0.00032 \quad , \quad |V_{us}| = 0.22431 \pm 0.00085 \quad , \quad |V_{ub}| = (3.82 \pm 0.20) \times 10^{-3}.$$

The recent reduction in the value of $|V_{ud}|$ has introduced a 2.3σ tension with the unitarity condition of the first row ($|V_{ud}|^2 + |V_{us}|^2 + |V_{ub}|^2$), resulting in a weaker consistency with the Standard Model fit [5, ch. 12].

The element V_{ub} , which governs the transition from a bottom quark (b) to an up quark (u), is particularly challenging to measure due to its small magnitude (compared to the other CKM matrix elements) and the complexity of distinguishing its contributions from background processes. High precision in determining $|V_{ub}|$ is critical for a reliable determination of the unitary condition. This precision is achieved through advanced parameterisation techniques, such as those that we are proposing in this thesis. In particular, we are going to explore in this chapter the accuracy that can be achieved using PAs and D-Logs [142].

Each particular matrix element can be determined from multiple processes. Since we are focus in $|V_{ub}|$ we will consider the B -meson channels and we are going to consider only exclusive processes. Among the three possible B -meson leptonic channels to obtain exclusive determinations of $|V_{ub}|$, the only available experimental input comes from $B \rightarrow \tau \nu_\tau$, since the partial decay rates to e and μ have not been measured yet [143]. However, the averaged experimental measurements [139] from BaBar, $BR(B \rightarrow \tau \nu_\tau) = 1.79(48) \times 10^{-4}$, and Belle, $BR(B \rightarrow \tau \nu_\tau) = 0.91(22) \times 10^{-4}$, both coming from averaging different τ -reconstruction channels, do not agree well and have large errors (about 25%). These measurements yield $|V_{ub}|f_B = 0.72(9)$ MeV and $|V_{ub}|f_B = 1.01(14)$ MeV [139], respectively, which can be used to extract $|V_{ub}|$ when combined with Lattice-QCD predictions of the B -meson decay constant f_B . As an example, using $f_B = 192.0(4.3)$ MeV from a $N_f = 2 + 1$ flavor gauge-field ensemble [139], one gets $|V_{ub}| = 5.26(12)(73) \times 10^{-3}$, from the BaBar measurement, and $|V_{ub}| = 3.75(8)(47) \times 10^{-3}$, from the Belle one, where the first uncertainty comes from the

¹The only hadronic input required in leptonic decays are the decay constants of the decaying mesons, which are well calculated in Lattice QCD [139].

error in f_B and the second one from experimental considerations. The discrepancy between these two results stands at approximately 2σ , indicating that higher precision from leptonic decays is necessary for a more reliable determination of $|V_{ub}|$. Therefore, new and more accurate data are anticipated from the Belle-II experiment [144].

Currently, the most precise determination of $|V_{ub}|$ comes from charmless semileptonic B -meson decays, using exclusive or inclusive methods². Inclusive determinations rely on the operator product expansion and perturbative QCD applied to $B \rightarrow X_u \ell \bar{\nu}_\ell$ observables, while the exclusive one require knowledge of the participating form factors. The most competitive exclusive determination of $|V_{ub}|$ is obtained from the decay channel $B \rightarrow \pi \ell \nu_\ell$, which has generally exhibited a tension with inclusive determinations (see [141] for a history of the comparison). More specifically, the experimental $B \rightarrow \pi \ell \nu_\ell$ observable depends upon known quantities, $|V_{ub}|$ -that we would like to determine- and the $B \rightarrow \pi$ form factors, that we need to describe and extrapolate to $q^2 = 0$ to obtain that $|V_{ub}|$. While QCD light-cone sum rules have been used to calculate the value of the vector form factor at $q^2 = 0$ with certain error [145], precise Lattice-QCD simulations are available in the energy region close to the maximum momentum transfer to the leptons, $17 \text{ GeV}^2 < q^2 < 26 \text{ GeV}^2$, from the HPQC Collaboration [146], the RBC and UKQCD (RBC/UKQCD) Collaborations [147], and the Fermilab Lattice and MILC (FNAL/MILC) Collaborations [148]. Several representations have been proposed for the form factor interpolation between these two regimes, including dipole-like functions [149, 150], the so called z -expansion parameterisations [151, 152], and more recently PAs [70, 142]. These parameterisations can be used to obtain $|V_{ub}|$ via a simultaneous fit of the Lattice-QCD form factor calculations and the partial branching ratios experimental data [153–157]. The q^2 dependence of the form factor is thus fixed at small q^2 by data, which due to phase-space suppression have poor access to the large- q^2 region, and at large q^2 by the Lattice simulations, The theoretical uncertainties on the form factors were the dominant source error in $|V_{ub}|$ until the 2015 FNAL/MILC results [148], which brought the QCD error to the same level as the experimental one. In the intermediate energy region around $q^2 \sim 20 \text{ GeV}^2$, both the experimental and Lattice-QCD errors are similar in size. This region is decisive for determining $|V_{ub}|$ with precision, and can be

²In the study of meson decays, inclusive and exclusive decay channels offer different perspectives. Inclusive decays consider all possible hadronic final states resulting from a transition, providing a comprehensive view with generally lower statistical uncertainty but complex theoretical interpretation. Exclusive decays focus on specific final states, offering precise information on particular processes and parameters, though they come with higher statistical uncertainty due to fewer observable events. Both approaches complement each other, balancing broad coverage and detailed precision.

employed to estimate the individual contributions from experimental and Lattice data.

The semileptonic $B_s \rightarrow K\ell\nu_\ell$ also depends on the CKM element $|V_{ub}|$. The only difference with respect to the decay $B \rightarrow \pi\ell\nu_\ell$ is that in $B_s \rightarrow K\ell\nu_\ell$ the light spectator quark is a strange quark (s) instead of an up or down quark as in the former process. The $B_s \rightarrow K$ form factors have been simulated on the Lattice by the HPQCD Collaboration [158], the RBC/UKQCD Collaborations [147], the ALPHA Collaboration [159], and more recently by the FNAL/MILC Collaborations [160]. As in the $B \rightarrow \pi\ell\nu_\ell$ case, these calculations can be used to extract $|V_{ub}|$ when combined with experimental measurements for $B_s \rightarrow K\mu\nu_\mu$, which can play an important role in reassessing the result and addressing the current exclusive versus inclusive $|V_{ub}|$ puzzle. Recently, the first experimental data on $B_s \rightarrow K\mu\nu_\mu$ became available by the LHCb Collaboration, which measured the partial branching ratio distribution in two regions of q^2 [161]. In this chapter, which is based on a recent work referenced in [142], we will use these data to determine $|V_{ub}|$ and illustrate the potential of a combined analysis of the decays $B \rightarrow \pi\ell\nu_\ell$ and $B_s \rightarrow K\mu\nu_\mu$. The decay $B_s \rightarrow K\ell\nu_\ell$ is also expected to be studied at the Belle-II experiment [144], where the e^+e^- collisions would yield a cleaner environment than the LHC. Other processes offering interesting information on $|V_{ub}|$, but not considered in this analysis, include the $B_{\ell 4}$ [162] and the baryonic $\Lambda_b \rightarrow p\ell\bar{\nu}_\ell$ decays [163, 164].

The present chapter is structured as follows. The hadronic matrix element and the participating vector and scalar form factors are defined in Sec. 5.1, where the differential decay distribution in terms of the latter is also given. In Sec. 5.2 we will use the Z-parameterisation as a model for the vector and scalar form factor so that we can observe the structure and convergence of PAs and D-Logs. In Sections 5.3 and 5.4, we determine $|V_{ub}|$ and the corresponding form factor parameters from fits to the $B \rightarrow \pi\ell\nu_\ell$ and $B_s \rightarrow K\mu\nu_\mu$ experimental measurements on the differential branching ratio distribution combined with the Lattice-QCD theoretical information on the form factors, using both PAs and D-logs. After that, in Sec. 5.5 we perform a simultaneous analysis including all available experimental and theoretical information on both exclusive decays. The outputs of our fits are then used in Sec. 5.6 to calculate some interesting phenomenological observables such as total decay rates, τ -to- μ ratio of differential decay rates and the forward-backward asymmetry. We close the chapter with an outlook in Sec. 5.7.

5.1 Lagrangian - Decay Amplitude and Form Factors

In the SM, the amplitude for the exclusive semileptonic decays $B \rightarrow \pi \ell \nu_\ell$ is given by:

$$i\mathcal{M} = \frac{G_F V_{ub}}{\sqrt{2}} L_\mu H^\mu, \quad (5.1)$$

where G_F is the Fermi constant and V_{ub} is the participating element of the CKM matrix. In Eq. (5.1), the leptonic current have the structure

$$L_\mu = \bar{u}(p_\nu) \gamma_\mu (1 - \gamma^5) v(p_\ell), \quad (5.2)$$

while the hadronic matrix element can be decomposed in terms of allowed Lorentz structures and two form factors encoding the hadronic information:

$$\begin{aligned} H_\mu &= \langle \pi(p_\pi) | \bar{u} \gamma_\mu b | B(p_B) \rangle \\ &= \left(p_B + p_\pi - q \frac{m_B^2 - m_\pi^2}{q^2} \right)_\mu f_+(q^2) + \frac{m_B^2 - m_\pi^2}{q^2} q_\mu f_0(q^2), \end{aligned} \quad (5.3)$$

where $q_\mu = (p_B - p_\pi)_\mu = (p_\ell + p_{\nu_\ell})_\mu$ is the transferred momentum to the dilepton pair. The q^2 functions $f_+(q^2)$ and $f_0(q^2)$ are, respectively, the vector and scalar form factors corresponding to the exchange of $J^P = 1^-$ and 0^+ particles in case there is non-resonant background. These two form factors satisfy a kinematical constraint,

$$f_+(0) = f_0(0), \quad (5.4)$$

which eliminates the (spurious) pole at $q^2 = 0$ in Eq. (5.3).

In terms of these form factors, the dilepton mass squared distribution reads:

$$\begin{aligned} \frac{d\Gamma(B \rightarrow \pi \ell \nu_\ell)}{dq^2} &= \frac{G_F^2 |V_{ub}|^2 \lambda^{1/2}(m_B^2, m_\pi^2, q^2)}{128 m_B^3 \pi^3 q^2} \left(1 - \frac{m_\ell^2}{q^2} \right)^2 \\ &\times \left\{ m_\ell^2 (m_B^2 - m_\pi^2)^2 |f_0(q^2)|^2 + \frac{2q^2}{3} \lambda(m_B^2, m_\pi^2, q^2) \left(1 + \frac{m_\ell^2}{2q^2} \right) |f_+(q^2)|^2 \right\} \end{aligned} \quad (5.5)$$

where $\lambda(x, y, z) = (x + y - z)^2 - 4xy$ is the Källén function. For the decay $B_s \rightarrow K \ell \nu_\ell$, the distribution is that of Eq. (5.5) but replacing $m_B \rightarrow m_{B_s}$, $m_\pi \rightarrow m_K$ and the respective $B \rightarrow \pi$ form factors by the $B_s \rightarrow K$ ones.

The present best knowledge of the vector and scalar $B \rightarrow \pi$ and $B_s \rightarrow K$ form factors are

obtained from Lattice-QCD calculations in the large- q^2 region, which are then extrapolated to the full kinematic range, *i.e.* $0 < q^2 < (m_B - m_\pi)^2$, using parameterisations based on resonance-exchange ideas [165–168] or the z -expansion [169] that we will explain and discuss in Sec. 5.2. As shown in [70], these parameterisations are in one form or another some kind of PA, which we will use in this chapter.

In our case, the key point is to realize that the form factors $f_{+,0}(q^2)$ are Stieltjes functions, those that satisfy Eq. (2.9), in our case we establish

$$f(q^2) = \int_0^{1/R} \frac{d\phi(u)}{1 - uq^2}, \quad (5.6)$$

where $f(q^2)$ satisfy Stieltjes properties in the range of $q^2 < 0$. In order to show how this "Stieltjes" notation corresponds to the dispersion relation for the form factor we set $R = s_{\text{th}} = (m_B + m_\pi)^2$, or $(m_{B_s} + m_K)^2$ for $B_s \rightarrow K\mu\nu mu$, then we can identify $d\phi(u) = \frac{1}{\pi} \frac{\text{Im}f(1/u)}{u} du$, and making the change of variables $u \rightarrow 1/s$, Eq. (5.6) returns a dispersive form factor representation.

$$f(q^2) = \frac{1}{\pi} \int_{s_{\text{th}}}^{\infty} ds' \frac{\text{Im}f(s')}{s' - q^2 - i\varepsilon}, \quad (5.7)$$

where q^2 is the invariant mass of the lepton pair. Since $f(q^2)$, and its imaginary part, is created by the vector current, $\text{Im}f(s)$ is a positive function ($\text{Im}f(s) = \pi\rho(s)$, and $\rho(s)$ the spectral function), the requirement of $\phi(u)$ to be non-decreasing is fulfilled and the convergence of PA and D-Logs to $f(q^2)$ is guaranteed.

Whenever information on resonance contributions to those form factors is available, for example the position of the resonance in the complex q^2 plane, it can be easily included in our analysis using the Partial/Type-PAs or Partial D-Logs defined in Sections 2.1.4 and 2.2.2 correspondingly. It could be done by forcing the poles or cuts of the approximant to lie exactly at the position of the resonance. In the present case where $B^*(1^-)$ resonance is known and can be nicely parameterised with the narrow-width approximation, we will also consider such extensions of PAs and D-Logs.

We will extensively apply Padé and D-Log theory to parameterize the vector and scalar form factors for both $B \rightarrow \pi$ and $B_s \rightarrow K$ decays. This approach will allow us to extrapolate lattice-QCD data from the large- q^2 region to the full kinematic range, specifically at $q^2 = 0$. An advantage of the Padé method in front of other parameterisations is the monitoring of

unitary violations. While the unitary constraint in z -parameterisations is rather vague, with PA it is crystal clear [60, 61, 70]: PA to Stieltjes functions are also Stieltjes functions. Since convergence is guaranteed in the cut plane all singularities from approximants must be real. The presence of complex-conjugated poles and/or zeros or cuts when approximating Stieltjes functions is a notorious violation of convergence, possible only if unitary violation is present in data (which is a non-Stieltjes property). We will explore this property in this chapter which extends a previous analysis in the same channel ($B \rightarrow \pi\ell\nu_\ell$) where PAs were studied [70].

5.2 PAs and D-Logs apply to z-parameterisation

In this section, we consider a model that parameterizes the semileptonic form factors as functions of q^2 , taking into account their analytic properties. Specifically, the model must satisfy causality and unitarity [170]. This requirement implies that the semileptonic form factors of B -mesons must be real analytic functions on the real q^2 -axis. In other words, these functions must be infinitely differentiable and can be locally represented by a convergent power series, except at points of discontinuity. If there is a branch cut in the function, for example in the interval $[q_0^2, \infty)$, the function must remain real for $q^2 < q_0^2$, assuming analyticity in this domain.

Since the z -parameterisation satisfies these analytic properties and has been adopted by various collaborations as the standard parameterisation for form factors in semileptonic decays such as $B \rightarrow \pi\ell\nu_\ell$ and $B_s \rightarrow K\mu\nu_{mu}$ [139, 171, 172], it serves as a promising candidate to test the analytic structure and convergence behaviour of PAs and D-Logs. By using the latest results for the z -parameterisation coefficients provided by FLAG [139], we will construct PAs and D-Logs directly from the resulting function of the z -parameterisation in a canonical manner, similar to the approach used in Section 4.3.

To construct the z -parameterisation, first we need to map the variable q^2 to a new variable z such that $|z| \leq 1$. We can then use the z expansion to obtain a model-independent parameterisation of our form factors valid over the entire kinematic range. Thus, we define the new variable z via the conformal mapping [151]:

$$z(q^2, t_0) = \frac{\sqrt{t_{\text{cut}} - q^2} - \sqrt{t_{\text{cut}} - t_0}}{\sqrt{t_{\text{cut}} - q^2} + \sqrt{t_{\text{cut}} - t_0}} \quad (5.8)$$

where the parameter t_{cut} is the particle-pair production threshold, which in our case

corresponds to

$$\sqrt{t_{\text{cut}}} = \begin{cases} M_{B^0} + M_{\pi^+} = 5.419\text{GeV} & \text{for } B \rightarrow \pi \\ M_{B_s^0} + M_{K^+} = 5.86\text{GeV} & \text{for } B \rightarrow K \end{cases} \quad (5.9)$$

and t_0 is a free parameter that can be chosen to minimize $|z|$ for the semileptonic-decay region. In this section we will use³

$$t_0 = t_{\text{cut}} - \sqrt{t_{\text{cut}}(t_{\text{cut}} - t_-)}, \quad (5.10)$$

where t_- is defined as the the maximum momentum transfer allowed in the semileptonic decays: $t_- = (M_{B_s} - M_K)^2$ for the case of $B_s \rightarrow K\ell\nu$ and $t_- = (M_{B^0} - M_\pi)^2$ for $B \rightarrow \pi\ell\nu$ decay. By choosing t_0 as Eq. (5.10) we can map the physical semileptonic decay region onto the symmetric interval $|z| \lesssim 0.28$ (by tanking $z(t_-, t_0)$), minimizing the maximum truncation error in the BCL expansion⁴ [152]. This mapping in z variable introduces a zero in $z(q^2, t_0)$ when $q^2 = t_0$, creating a strong dependence of the form factor on t_0 , with a zero in z that was not present in q^2 . One advantage of this method is that it simplifies the analytic continuation of form factors, especially for large momentum transfers. However, it only accounts for a single cut, and the use of a square root introduces threshold behavior that may not align with the true physical behavior near the threshold.

Using the new variable z , Eq. (5.8), we can present now a z expansion for the form factors. Two commonly used expansions were proposed by Boyd, Grinstein and Lebed (BGL-parameterisation) [151] and by Bourrely, Caprini and Lellouch (BCL-parameterisation) [152, 169]. The latter is the one we will use during this section and is given by

$$f_+(q^2) = \frac{1}{1 - q^2/M_{B^*(1^-)}^2} \sum_{k=0}^{K-1} b_k^+(t_0) \left[z^k - (-1)^{k-K} \frac{k}{K} z^K \right] \quad (5.11)$$

$$f_0(q^2) = \frac{1}{B(q^2)} \sum_{k=0}^{K-1} b_k^0(t_0) z^k \quad (5.12)$$

where the $B(q^2)$ function in the scalar form factor accounts for poles below and near the $B_s \rightarrow K$ production threshold via

$$B(q^2) \equiv \begin{cases} 1 & \text{for } B \rightarrow \pi \\ 1 - q^2/M_{B^*(0^+)}^2 & \text{for } B_s \rightarrow K \end{cases} \quad (5.13)$$

³Other options for t_0 are $t_0 = 0$ or $t_0 = t_-$, depending on the " q^2 " range we want to study.

⁴It can be proven using unitarity constraints to the BCL expansion, considering terms when $K \rightarrow \infty$

Table 5.1: Input meson masses used in the z -parameterisation.

	M_B	M_{B_s}	M_{π^+}	M_{K^+}	$M_{B^*(1^-)}$	$M_{B_s^*(0^+)}$
Value (GeV)	5.2797	5.3669	0.1396	0.4937	5.3246	5.68

Table 5.2: Coefficient results for Z-parameterisation presented by FLAG coll. [139] in $B \rightarrow \pi$ decay, and by FNAL/MILC coll. [160] in the case of $B_s \rightarrow K$ decay.

channel	$V_{ub} \times 10^3$	$b_0^{(+)}$	$b_1^{(+)}$	$b_2^{(+)}$	$b_3^{(+)}$	$b_0^{(0)}$	$b_1^{(0)}$	$b_3^{(0)}$
$B \rightarrow \pi \ell \nu$	3.73	0.414	-0.494	-0.31	—	0.499	-1.426	—
$B_s \rightarrow K \ell \nu$	—	0.362	-0.956	-0.853	0.279	0.198	-0.166	-0.375

In agreement with the values used by FNAL/MILC collaboration in their 2019-review [160], we fix the location of the vector pole B^* to the value $M_{B^*(1^-)} = 5.32456(25)$ GeV. The above threshold scalar pole B_s^* is taken to be $M_{B_s^*(0^+)} = 5.68$ GeV [160]⁵. The Table 5.1 lists the relevant meson masses used in our z -parametrisation [5, 139, 160].

In channel $B \rightarrow \pi$ we will take the results provided by FLAG Review 2019 [139]. Thus, we will use a z -parameterisation where the polynomial degree is given by $K = 3$. Same degree (K) for the vector and scalar form factor provided the best fit found by FLAG. Parameter coefficients were presented in Table 5.2. The last coefficient of the scalar form factor ($b_2^{(0)}$) can be obtained from all other coefficients imposing the $f_+(q^2 = 0) = f_0(q^2 = 0)$ constraint, recall Eq. (5.4). In the case of $B_s \rightarrow K$ decay, neither FLAG nor FNAL/MILC provided an estimate for V_{ub} , however since we only need a model for the form factor function we can use the best fit obtained by FNAL/MILC [160] in this channel. For this case, the polynomial degree is $K = 4$ and we use the constraint in $q^2 = 0$ to determine parameter $b_2^{(0)}$. Values for coefficients in $B_s \rightarrow K$ are also presented in Table 5.2.

Finally we will consider the results from FLAG and FNAL/MILC to build our test model for the vector and scalar form factor so that they satisfy their analyticity properties and allow us to consistently construct PAs and D-Logs. By replacing the values from Table 5.2 into Eqs. (5.11) and (5.12), we will obtain what we will call the z -model, the function we

⁵Different values have been used by different collaborations, for instance HPQCD fixed the value in 5.6794 GeV, while RBC/UKQCD use 5.63 GeV, and FLAG take an average of them.

intend to approximate using PAs and D-Logs. In the case of the $B \rightarrow \pi$ channel, we have:

$$f_+(q^2)\Big|_{z\text{-model}}^{B\pi} = \frac{1}{1 - q^2/M_{B^*(1^-)}^2} \left(b_0^{(+)} + b_1^{(+)}z + b_2^{(+)}z^2 + \frac{2b_2^{(+)} - b_1^{(+)}}{3}z^3 \right), \quad (5.14)$$

$$f_0(q^2)\Big|_{z\text{-model}}^{B\pi} = \left(b_0^{(0)} + b_1^{(0)}z + b_2^{(0)}z^2 \right). \quad (5.15)$$

In the case of $B_s \rightarrow K$ channel, we have:

$$f_+(q^2)\Big|_{z\text{-model}}^{B_s K} = \frac{1}{1 - q^2/M_{B^*(1^-)}^2} \left(b_0^{(+)} + b_1^{(+)}z + b_2^{(+)}z^2 + b_3^{(+)}z^3 + \frac{3b_1^{(+)} + b_1^{(+)} - 2b_2^{(+)}}{4}z^4 \right), \quad (5.16)$$

$$f_0(q^2)\Big|_{z\text{-model}}^{B_s K} = \frac{1}{1 - q^2/M_{B^*(0^+)}^2} \left(b_0^{(0)} + b_1^{(0)}z + b_2^{(0)}z^2 + b_3^{(0)}z^3 \right). \quad (5.17)$$

It is important to note that z -models become rational functions when we apply the variable change $x^2 = t_{\text{cut}} - q^2$ and $a^2 = t_{\text{cut}} - t_0$, revealing their most basic structure. For example, in the case of $f_+|^{B\pi}$, this results in a rational function of order 3 in x for the numerator and order 4 in x for the denominator, considering the pole in $M_{B^*}^2$. Similarly, for $f_0|^{B\pi}$, the function becomes a rational function of order 2 in both the numerator and denominator, which can be easily parameterized using distinct sequences of PAs.

It is also important to clarify that while the model based on the z -expansion satisfies the unitarity of the form factors, it does not meet the condition of being a Stieltjes-type function. This can be easily verified by calculating the first Hankel determinants for $f_{+/0}$, where several are found to be negative (recall the positivity condition in Eq. (2.12)). Although the model lacks this property, both approximations —using PAs and D-Logs— still allow us to identify the expected zeros, poles and branch cuts location when they will be used for the fitting.

5.2.1 Padé Approximation

Having established the z -model for both the vector and scalar form factors, we will first construct the PAs following the procedure presented in Section 2.1.1, using Eqs. (5.14) and (5.15) as the target function with the coefficients from the $B \rightarrow \pi$ channel in Table 5.2. In order to observe any pattern in the poles and zeros of the function, we will construct the first approximants in the diagonal sequence (P_N^N) and the sub-diagonal sequence (P_N^{N-1}) . As an example, we present the PAs obtained up to $N = 5$ for the vector form factor.

sequence $P_N^N[f_+]$:

$$P_1^1 = -\frac{0.094 (q^2 + 64.86)}{q^2 - 24.36} \quad (5.18)$$

$$P_2^2 = -\frac{0.02 (q^2 - 189.04) (q^2 + 106.99)}{(q^2 - 60.69) (q^2 - 27.82)} \quad (5.19)$$

$$P_3^3 = -\frac{0.008 (q^2 - 622.73) (q^2 - 52.96) (q^2 + 115.17)}{(q^2 - 101.99) (q^2 - 43.39) (q^2 - 28.227)} \quad (5.20)$$

$$P_4^4 = -\frac{0.004 (q^2 - 1503.97) (q^2 - 86.22) (q^2 - 40.57) (q^2 + 116.242)}{(q^2 - 154.98) (q^2 - 60.65) (q^2 - 37.70) (q^2 - 28.314)} \quad (5.21)$$

$$P_5^5 = -\frac{0.002 (q^2 - 2982.73) (q^2 - 130.60) (q^2 - 55.61) (q^2 - 36.15) (q^2 + 116.378)}{(q^2 - 219.65) (q^2 - 82.12) (q^2 - 47.85) (q^2 - 34.97) (q^2 - 28.34)} \quad (5.22)$$

sequence $P_N^{N-1}[f_+]$:

$$P_1^0 = -\frac{4.44}{q^2 - 17.70} \quad (5.23)$$

$$P_2^1 = \frac{3.95 (q^2 + 137.67)}{(q^2 - 79.57) (q^2 - 27.29)} \quad (5.24)$$

$$P_3^2 = \frac{6.50 (q^2 - 67.01) (q^2 + 118.45)}{(q^2 - 152.83) (q^2 - 47.94) (q^2 - 28.13)} \quad (5.25)$$

$$P_4^3 = \frac{7.83 (q^2 - 124.32) (q^2 - 44.20) (q^2 + 116.67)}{(q^2 - 249.78) (q^2 - 71.51) (q^2 - 39.63) (q^2 - 28.29)} \quad (5.26)$$

$$P_5^4 = \frac{8.65 (q^2 - 204.62) (q^2 - 64.44) (q^2 - 37.72) (q^2 + 116.44)}{(q^2 - 370.485) (q^2 - 101.28) (q^2 - 52.21) (q^2 - 36.00) (q^2 - 28.33)} \quad (5.27)$$

In the above two sequences it can be seen that there is an accumulation of poles and zeros on the real positive q^2 -axis, densifying around $q^2 \approx 28.34 \text{ GeV}^2$, which corresponds precisely to an approximation to a possible branch cut at the resonance of the B meson with total spin $J = 1$ ($m_{B^*(1-)}^2 = 28.3513 \text{ GeV}^2$), c.f. Table 5.1, indeed this singularity was to be expected as it is explicitly found in the z-parameterization, see Eqs. (5.11) and (5.14). On the other hand, as the order of the approximant increases, the position of a zero around $q^2 \approx -116 \text{ GeV}^2$ becomes evident, suggesting that in the negative q^2 region the function is decreasing and must cross the axis at some point.

In the case of the scalar form factor we obtain the following approximants:

sequence $P_N^N[f_0]$:

$$P_1^1 = \frac{0.21 (q^2 - 19.37)}{q^2 - 15.98} \quad (5.28)$$

$$P_2^2 = \frac{0.60 (q^4 - 54.72 q^2 + 2087.55)}{(q^2 - 152.32) (q^2 - 32.68)} \quad (5.29)$$

$$P_3^3 = \frac{0.59 (q^2 + 32.70) (q^4 - 54.60 q^2 + 2075.88)}{(q^2 - 148.86) (q^2 - 32.74) (q^2 + 32.69)} \quad (5.30)$$

$$P_4^4 = \frac{0.74 (q^2 - 177.38) (q^2 - 32.26) (q^4 - 54.50 q^2 + 2029.7)}{(q^2 - 334.69) (q^2 - 93.30) (q^2 - 35.64) (q^2 - 30.61)} \quad (5.31)$$

$$P_5^5 = \frac{0.59 (q^2 - 138.17) (q^2 - 32.90) (q^2 + 1016.73) (q^4 - 54.53 q^2 + 2029.57)}{(q^2 - 250.45) (q^2 - 86.58) (q^2 - 36.23) (q^2 - 30.84) (q^2 + 904.79)} \quad (5.32)$$

sequence $P_N^{N-1}[f_0]$:

$$P_1^0 = -\frac{22.89}{q^2 - 91.34} \quad (5.33)$$

$$P_2^1 = \frac{11.18 (q^2 - 59.06)}{(q^2 - 26.38) (q^2 + 99.80)} \quad (5.34)$$

$$P_3^2 = \frac{1217.42 (q^4 - 54.76 q^2 + 2068.38)}{(q^2 - 135.55) (q^2 - 32.80) (q^2 + 2259.71)} \quad (5.35)$$

$$P_4^3 = \frac{713.45 (q^2 - 23.43) (q^4 - 54.54 q^2 + 2046.38)}{(q^2 - 124.48) (q^2 - 33.11) (q^2 - 23.39) (q^2 + 1415.66)} \quad (5.36)$$

$$P_5^4 = \frac{3041.52 (q^2 - 133.00) (q^2 - 32.93) (q^4 - 54.53 q^2 + 2029.66)}{(q^2 - 234.72) (q^2 - 85.78) (q^2 - 36.26) (q^2 - 30.85) (q^2 + 4789.29)} \quad (5.37)$$

For the scalar form factor PAs, we also observe an accumulation of poles and zeros along the positive real q^2 -axis. In this case, the distribution suggests the presence of a possible branch cut at $q^2 \approx 30.8 \text{ GeV}^2$ potentially linked to a resonance of the B meson with $J = 0$ ($m_{B^*(0+)}$) around $\sim 5.55 \text{ GeV}$. Unlike the vector form factor, some of the sub-diagonal PAs, as well as diagonal approximants for odd N , display a pole in the negative q^2 region, indicating that z-parameterisation for the scalar form factor (Eq. (5.15)) ceases to be a Stieltjes-kind function, however these poles quickly move away from $q^2 = 0$ placing them far away from the convergence region. On the other hand, it is also observed that the function has a complex-conjugate zero that stabilizes around $q_0^2 \approx 27.26 \pm i 35.86$, though the function remains analytic despite this feature.

To study the convergence pattern of the approximants in the different regions of q^2 we take the ratio between the approximant and the original function ($f_{(+/0)}|_{\text{z-model}}$), which can be expressed as:

$$R_i^{(+/0)} = \frac{\text{PA}_{N=i}[f_{(+/0)}]}{f_{(+/0)}} \quad (5.38)$$

The convergence pattern of the PAs for the vector form factor is illustrated in Fig. 5.1. As

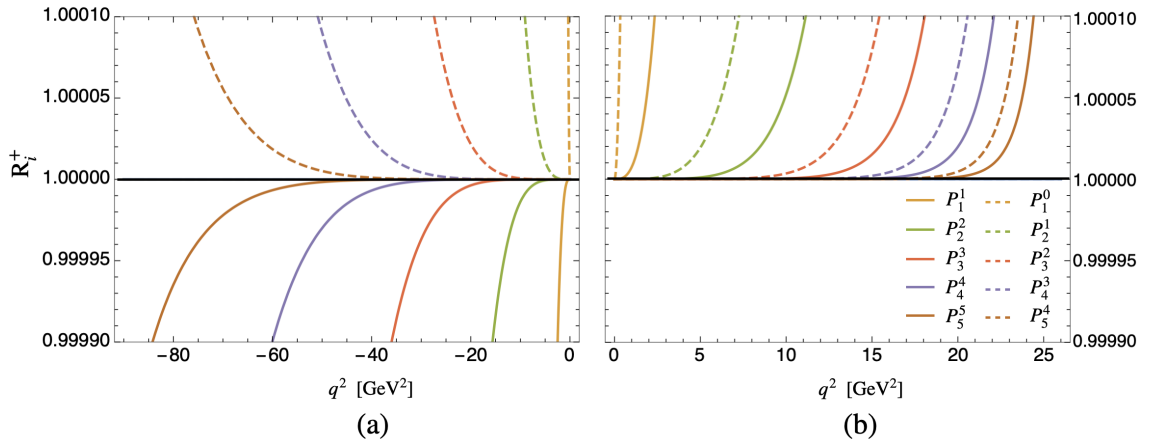


Figure 5.1: Convergence ratio $R_i^{(+)}$, for vector form factor using PAs to z-model for $B \rightarrow \pi$ decay. (a) negative q^2 region, (b) positive q^2 region.

shown, the typical convergence behavior for Stieltjes functions (see Eq. (2.16)) is satisfied in the region $q^2 < 0$, where the diagonal sequence approximates the function from below, and the sub-diagonal sequence from above. However, in the region where data for the differential decay rate of $B \rightarrow \pi$ are available, i.e., for $0 < q^2 < (m_B - m_\pi)^2$, we only have uniform convergence as the order of the approximant increases, it means we can not use the theorem exposed in Eqs. (2.16) and (2.17) but we can use the same sequence to look convergence in this region.

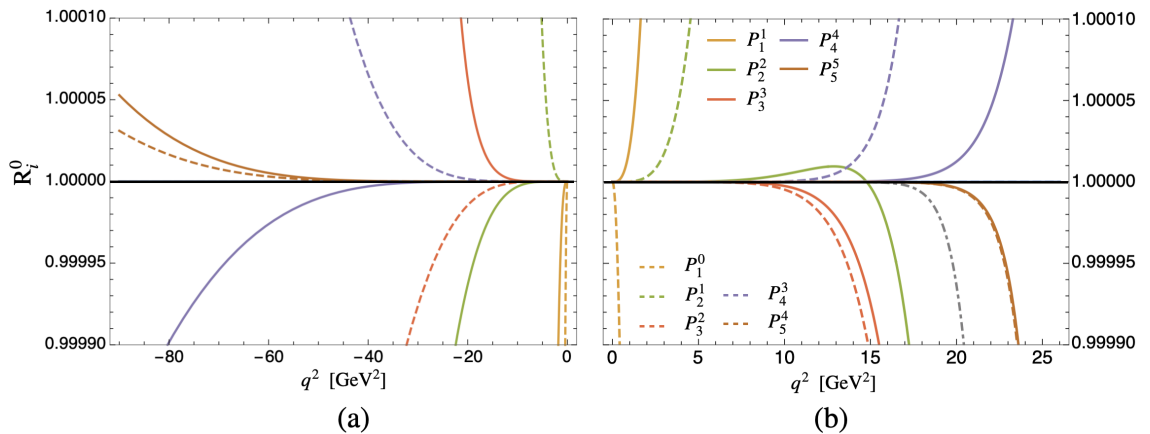


Figure 5.2: Convergence ratio $R_i^{(0)}$, for scalar form factor using PAs to z-model for $B \rightarrow \pi$ decay. (a) negative q^2 region, (b) positive q^2 region

In the case of the scalar form factor, shown in Fig. 5.2, the convergence is not uniform. While the PAs do exhibit convergence as the order increases, it is not systematic. Some

approximants with fewer coefficients provide better approximations than those with more parameters, as seen with P_4^5 performing better than P_5^5 for $q^2 < 0$. Moreover, the convergence is inconsistent in direction: within the same sequence, some approximants converge from above the function, while others converge from below, with no discernible pattern. For example, the PA P_2^2 in the positive q^2 region initially approximates the function from above and loses convergence at $q^2 \sim 7 \text{ GeV}^2$, before approximating again and move away below the function at 16 GeV^2 . Figure 5.2(b) also indicates the radius of convergence of the function's Taylor expansion (dot-dashed gray line) at around 17 GeV^2 , showing that only PAs with $N > 4$ exhibit better convergence than the Taylor expansion.

The decay channel $B_s \rightarrow K$ exhibits the same convergence behavior as the $B \rightarrow \pi$ decay for both the scalar and vector form factors. Therefore, an additional analysis for this channel is unnecessary. It is important to note that, in both cases, the approximants aim to reproduce the resonance points of the B meson.

5.2.2 D-Log Padé Approximation

Before analyzing the structure of the D-Logs, we can first examine the expected behavior of the z -transformation (Eq. (5.8)) when taking the logarithmic derivative with respect to q^2 -variable. As can be seen below a single power of z yields a constant in the numerator and have a multiplicity of 1.5 for q^2 in the denominator, which is not accessible by a PA.

$$\frac{d}{dq^2} \ln [z(q^2, t_0)] = \frac{\sqrt{t_{\text{cut}} - t_0}}{\sqrt{t_{\text{cut}} - q^2}} \left(\frac{1}{q^2 - t_0} \right) \quad (5.39)$$

Instead of using q^2 , we apply the previously mentioned variable change, where $x^2 = t_{\text{cut}} - q^2$ and $a^2 = t_{\text{cut}} - t_0$. The logarithmic derivative can now be easily approximated by $P_2^0(x)$ (dx/dq^2). Thus, for the $B \rightarrow \pi$ channel, the scalar form factor f_0 can be approximated by $P_3^2(x)$, while the vector form factor f_+ requires $P_6^5(x)$. However, we aim to study the convergence behavior in q^2 , which may lead to approximants of the same order, given that $x^2 \sim q^2$.

For the canonical construction of the D-Logs, we will follow the procedure described in Section 2.2.1. Recall that this essentially involves applying the logarithmic derivative to the form factors given by Eqs. (5.14) and (5.15). Afterward, we obtain the desired Padé approximant, and finally, we integrate and exponentiate as indicated in Eq. (2.27). Accordingly, we will analyze the first D-Logs in both the diagonal and sub-diagonal sequences for both form factors (up to $N = 5$). The D-Logs for the vector form factor are:

sequence $D_N^N[f_+]$:

$$D_1^1 = \frac{11.28 e^{0.016 q^2}}{(28.08 - q^2)^{1.14}} \quad (5.40)$$

$$D_2^2 = \frac{11.04 e^{0.011 q^2} (q^2 + 56.41)^{0.12}}{(29.17 - q^2)^{1.26}} \quad (5.41)$$

$$D_3^3 = \frac{0.76 e^{0.002 q^2} (q^2 + 111.03)^{0.85}}{(28.54 - q^2)^{1.11} (48.33 - q^2)^{0.36}} \quad (5.42)$$

$$D_4^4 = \frac{0.69 e^{0.0008 q^2} (q^2 + 115.86)^{0.98}}{(28.42 - q^2)^{1.06} (38.30 - q^2)^{0.24} (76.94 - q^2)^{0.29}} \quad (5.43)$$

$$D_5^5 = \frac{0.97 e^{0.0003 q^2} (q^2 + 116.34)^{1.00}}{(28.38 - q^2)^{1.03} (34.77 - q^2)^{0.18} (51.43 - q^2)^{0.21} (116.59 - q^2)^{0.26}} \quad (5.44)$$

sequence $D_N^{N-1}[f_+]$:

$$D_1^0 = \frac{801.63}{(39.01 - q^2)^{2.20}} \quad (5.45)$$

$$D_2^1 = \frac{0.0002 (q^2 + 185.81)^{2.20}}{(29.51 - q^2)^{1.32}} \quad (5.46)$$

$$D_3^2 = \frac{0.29 (q^2 + 121.57)^{1.12}}{(28.65 - q^2)^{1.14} (56.76 - q^2)^{0.42}} \quad (5.47)$$

$$D_4^3 = \frac{0.97 (q^2 + 117.07)^{1.02}}{(28.45 - q^2)^{1.07} (40.82 - q^2)^{0.27} (103.49 - q^2)^{0.34}} \quad (5.48)$$

$$D_5^4 = \frac{1.69 (q^2 + 116.492)^{1.00}}{(28.39 - q^2)^{1.04} (35.93 - q^2)^{0.20} (58.13 - q^2)^{0.23} (172.72 - q^2)^{0.30}} \quad (5.49)$$

In both sequences we can observe two branch points that stabilize as we increase the order of the D-Log; one of them is a cut located in the denominator with value very close to 28.38 GeV^2 and multiplicity very close to 1, which suggests that it corresponds to the pole of the z-parameterisation in the vector form factor ($m_{B^*(1-)}$). The other stable point also exhibits multiplicity close to 1 but is located in the numerator and in the negative region of q^2 around $\sim 116.4 \text{ GeV}^2$, i.e., exactly the same zero fixed by the PAs. The rest of the cuts in the approximants are located in the denominator and usually have very small exponents (< 0.3) which implies that their contribution is dominated by the first term in their Taylor expansion since it is smaller and smaller from the second term on. Finally we have the exponential function in the diagonal sequence whose coefficient is positive but smaller and smaller, decreasing considerably its contribution. Looking at the structure of these sequences, a general expression can be proposed to parameterize the vector form

factor as:

$$D_N^{N-1} = \frac{f_0 (q^2 + b_2)^{c_2}}{(b_1 - q^2)^{c_1} (b_3 - q^2)^{c_3} \dots (b_{N-1} - q^2)^{c_{N-1}}} \quad (5.50)$$

$$D_N^N = \frac{f_0 (q^2 + b_2)^{c_2} e^{a_1 q^2}}{(b_1 - q^2)^{c_1} (b_3 - q^2)^{c_3} \dots (b_{N-1} - q^2)^{c_{N-1}}} \quad (5.51)$$

where b_i is the position for the different cuts in the approximant, c_i is the associated multiplicity, a_i are the coefficients associated to the exponential function and f_0 is a normalization factor. On the other hand, the first D-Logs approximating the scalar form factor are shown below:

sequence $D_N^N[f_0]$:

$$D_1^1 = \frac{3.67 e^{-0.021 q^2}}{(25.73 - q^2)^{0.83}} \quad (5.52)$$

$$D_2^2 = 0.0005 (q^4 - 100.41 q^2 + 2870.93)^{2.50} e^{0.0249 q^2 + 11.24 \text{ ArcTan}(0.0267(2q^2 - 100.41))} \quad (5.53)$$

$$D_3^3 = \frac{0.012 (q^4 - 52.35 q^2 + 1891.77)^{0.86} e^{0.0020 q^2 + 0.16 \text{ ArcTan}(0.0144(2q^2 - 52.35))}}{(32.25 - q^2)^{0.96}} \quad (5.54)$$

$$D_4^4 = \frac{0.041 (q^4 - 54.69 q^2 + 2051.35)^{1.02} e^{0.0006 q^2 - 0.07 \text{ ArcTan}(0.0138(2q^2 - 54.69))}}{(30.75 - q^2)^{0.65} (53.97 - q^2)^{0.94}} \quad (5.55)$$

$$D_5^5 = \frac{0.093 (q^4 - 54.55 q^2 + 2027.29)^{1.00} e^{0.0003 q^2 + 0.01 \text{ ArcTan}(0.0140(2q^2 - 54.55))}}{(30.20 - q^2)^{0.51} (39.50 - q^2)^{0.56} (97.31 - q^2)^{0.62}} \quad (5.56)$$

sequence $D_N^{N-1}[f_0]$:

$$D_1^0 = \frac{0.31}{(8.76 - q^2)^{0.096}} \quad (5.57)$$

$$D_2^1 = 0.06 (q^4 - 60.09 q^2 + 1320.91)^{0.50} e^{2.167 \text{ ArcTan}(0.0245(2q^2 - 60.09))} \quad (5.58)$$

$$D_3^2 = \frac{0.03 (q^4 - 49.61 q^2 + 1975.53)^{0.80} e^{-0.225 \text{ ArcTan}(0.0136(2q^2 - 49.61))}}{(33.60 - q^2)^{1.19}} \quad (5.59)$$

$$D_4^3 = \frac{0.13 (q^4 - 55.54 q^2 + 2048.79)^{1.07} e^{0.058 \text{ ArcTan}(0.0140(2q^2 - 55.54))}}{(31.16 - q^2)^{0.74} (75.45 - q^2)^{1.13}} \quad (5.60)$$

$$D_5^4 = \frac{0.19 (q^4 - 54.40 q^2 + 2025.28)^{0.97} e^{-0.002 \text{ ArcTan}(0.0139(2q^2 - 54.40))}}{(30.38 - q^2)^{0.56} (43.07 - q^2)^{0.66} (154.90 - q^2)^{0.56}} \quad (5.61)$$

In the case of the D-Logs for the scalar form factor, we obtain a more complicated analytical structure due to the presence of singularities outside the real q^2 -axis. Specifically, these singularities are interpreted as two vertical cuts in the complex plane located around $\{q^2 \mid |\text{Im}(q^2)| \gtrsim 35.8, \forall \text{Re}(q^2) \cong 27.2\}$, as shown in Fig. 5.3. These vertical cuts are generated by the ArcTan function in the exponential factor appearing in the approximants with $N \geq 2$. In general, the D-Logs for the scalar form factor in the sequences D_N^N and

D_N^{N-1} can be expressed as follows:

$$D_N^{N-1} = \frac{f_0 (q^4 - 2 \operatorname{Re}\{b_2\} q^2 + b_2 b_2^*)^{c_2} e^{d_1 \operatorname{ArcTan}(2 d_2 (q^2 - \operatorname{Re}\{b_2\}))}}{(b_1 - q^2)^{c_1} (b_3 - q^2)^{c_3} \dots (b_{N-2} - q^2)^{c_{N-2}}} \quad (5.62)$$

$$= \frac{f_0 (q^4 - 2 \operatorname{Re}\{b_2\} q^2 + b_2 b_2^*)^{c_2} e^{a_1 q^2 + d_1 \operatorname{ArcTan}(2 d_2 (q^2 - \operatorname{Re}\{b_2\}))}}{(b_1 - q^2)^{c_1} (b_3 - q^2)^{c_3} \dots (b_{N-2} - q^2)^{c_{N-2}}} D_N^N \quad (5.63)$$

where b_2 is a complex parameter and d_i are parameters associated to the ArcTan function. It is important to note that the introduction of a singularity outside the real axis implies that the construction of a D-Log D_N^M requires an additional coefficient, i.e. $N + M + 3$ coefficients.

In addition to these off-axis branch cuts, the D-Logs for the scalar form factor also exhibit a cut on the positive real q^2 -axis, as shown in Fig. 5.3. This cut is located at approximately 30.2 GeV^2 , and can be associated with the resonance of the B meson with $J = 0$, corresponding to a mass of around 5.5 GeV . However, in this case, the exponent tends to be 0.5 —a new information respect the PAs—. Another distinction from the vector form factor is that the additional cuts appearing in the denominator no longer have small exponents and are not as far from the origin. As a result, their contribution can affect the shape of the function near the convergence region.

We again analyse the convergence of the approximants splitting the q^2 domain in two regions. For the vector form factor, a convergence pattern typical of Stieltjes functions is observed in the negative q^2 region, except for the D-Log D_1^1 , as shown in Fig. 5.4. However, it is important to remark that the PAs in the P_1^N sequence cannot always be guaranteed to follow Stieltjes behavior, even if they are constructed using Taylor coefficients of a Stieltjes function (c.f. Section 2.1.3). In addition, the D-Logs with $N = 1$ fail to account for the cut in the numerator on the negative real q^2 -axis. In the positive q^2 region, approximant D_1^1 also do not follow the expected convergence pattern, while the other D-Logs systematically approximate the function from below.

On the other hand, the convergence for the scalar form factor, as shown in Fig. 5.5, follows a Stieltjes-like pattern in the region $q^2 < 0$. As well as, in the region $q^2 > 0$, the approximants generally approach the function from below, except (in both regions) for the D-Logs with $N = 1$, which preserve the expected range of convergence but change the direction of approximation compared to the other approximants in the same sequence.

The D-Logs obtained using the values from the z -parameterisation corresponding to the decay $B_s \rightarrow K$ exhibit a similar analytical structure, determining the resonance values for

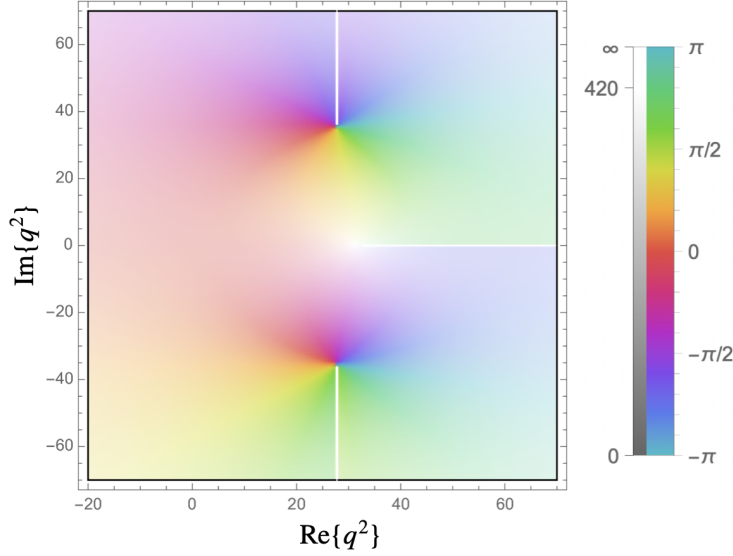


Figure 5.3: Representation of D-Log D_5^4 apply to scalar form factor in the q^2 -complex plane, where cyclic color function represents the argument and darkness (gray scale) represents the modulus. White lines are branch cuts.

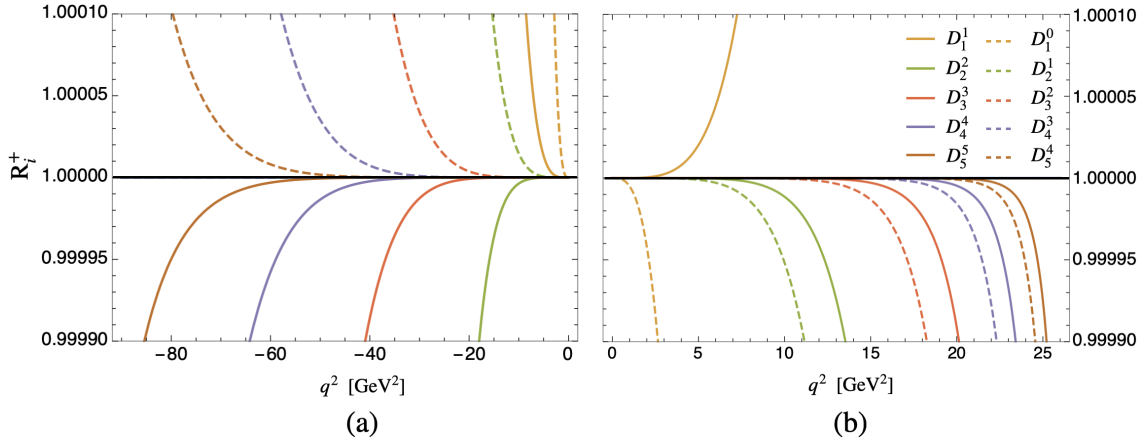


Figure 5.4: Convergence ratio $R_i^{(+)}$, for vector form factor using D-Logs to z -model for $B \rightarrow \pi$ decay. (a) negative q^2 region, (b) positive q^2 region.

the B meson in both its vector and scalar forms. For the scalar form factor, the D-Logs predict a branch cut located around 32.4 GeV^2 , which differs by only 0.2% from the value used by the z -model for $m_{B^*(0+)}$ (see Table 5.1), but with an associated multiplicity of 1.2. Again, these approximants exhibit two cuts outside the real q^2 -axis. For the vector form factor, the D-Logs predict a mass of $m_{B^*(1-)} \sim 5.324 \text{ GeV}$ also very accurate to the input used by the z -parameterisation, and a branch cut appears in the numerator that behaves

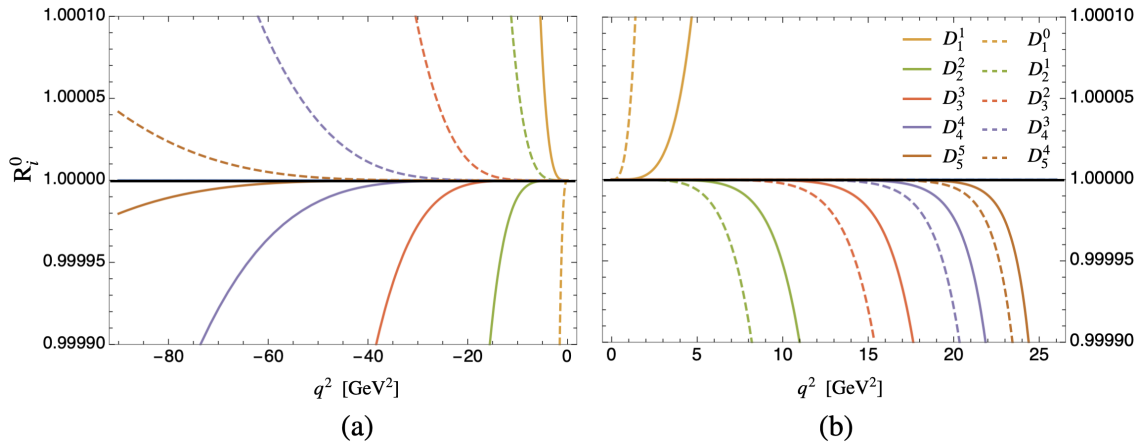


Figure 5.5: Convergence ratio $R_i^{(0)}$, for scalar form factor using D-Logs to z-model for $B \rightarrow \pi$ decay. (a) negative q^2 region, (b) positive q^2 region.

almost like a zero of the function, as its exponent is very close to 1. This cut is located in the negative q^2 region, around -33.53 GeV^2 .

To conclude this section, we aim to compare the convergence behavior of the PAs and the D-Logs. For this purpose, we examine the first term of the Taylor series that each approximant can predict. For instance, the PA P_3^2 is constructed using six Taylor coefficients of the original function and can predict the 7th term by expanding its respective Taylor series. Similarly, the D-Log D_2^2 is constructed from the first six Taylor coefficients of the function and also provides a prediction for the 7th term. This allows us to compare which of the two predictions is closer to the corresponding term of the original function's expansion. Table (5.3) presents the differences between the terms predicted by the approximants and the actual terms of the original function as the order of the PAs and D-Logs increases.

In Table 5.3, green highlights indicate cases where the D-Logs provide a better prediction, while orange highlights correspond to better approximations from the PAs. In the lower-order approximants, the PAs generally offer a more accurate prediction. It is also observed that D-Logs tend to give better predictions when they have an odd number of free parameters, such as those in the subdiagonal sequence, whereas they only surpass the convergence of the diagonal PAs starting from D_5^5 (with 12 free parameters). In conclusion, the PAs demonstrate faster convergence for the first few approximants (up to $N = 3$), while the D-Logs require a larger number of parameters to achieve faster convergence in any sequence. Therefore, it cannot be definitively concluded that one method is superior to the other, as both exhibit rapid convergence.

The analysis in this section has allowed us to determine the analytical structures that

Table 5.3: Comparison of convergence between PAs and D-Logs approaching to the vector form factor. Values in the table represent the difference between the predicted Taylor coefficient by the PA (second column) or D-Log (third column) and the Taylor expansion of the Z-model. Background color identified if PA (orange) or D-Log (green) makes a better approximation with same number of free parameters.

No Parameters	PAs	D-Logs
3 (10^{-6})	1.78	-1.21
4 (10^{-9})	5.71	6.44
5 (10^{-11})	6.01	-6.15
6 (10^{-13})	3.20	-14.2
7 (10^{-15})	3.29	-2.95
8 (10^{-17})	2.05	-3.62
9 (10^{-19})	2.05	-1.58
10 (10^{-21})	1.38	-1.68
11 (10^{-23})	1.35	-0.91
12 (10^{-25})	0.95	-0.91

the PAs and D-Logs can exhibit when parameterizing the form factors for the $B \rightarrow \pi$ and $B_s \rightarrow K$ decays, as well as the potential convergence patterns shown by each sequence of approximants. In the next section, we will use experimental and lattice data to directly fit the PAs and D-Logs.

5.3 Fits to the decay $B \rightarrow \pi \ell \nu_\ell$

We start performing fits to the $B \rightarrow \pi \ell \nu_\ell$ differential branching ratio distribution experimental measurements combined with the $B \rightarrow \pi$ form factor Lattice-QCD simulated data. To that end, we minimize the following χ^2 -like function,

$$\chi_{B\pi}^2 = N \left(\frac{\chi_{\text{data}}^2}{N_{\text{data}}} + \frac{\chi_{\text{Lattice}}^2}{N_{\text{Lattice}}} \right), \quad (5.64)$$

where N_{data} is the number of experimental points, N_{Lattice} the number of the Lattice form factor q^2 -points, and $N = N_{\text{data}} + N_{\text{Lattice}}$. The above definition ensures the χ^2 function with a smaller number of points is well represented in $\chi_{B\pi}^2$, and is not overridden by that

with a larger number of points. The individual χ^2 functions in Eq. (5.64) are given by:

$$\chi_{\text{data}}^2 = \sum_{i,j=1}^{13} \Delta_i^{\text{data}} (\text{Cov}_{ij}^{\text{data}})^{-1} \Delta_j^{\text{data}}, \quad (5.65)$$

where

$$\Delta_k^{\text{data}} = \left(\frac{\Delta B}{\Delta q^2} \right)_k^{\text{data}} - \frac{\tau_{B^0}}{\Delta q_k^2} \int_{q_k^{\text{low}}}^{q_k^{\text{high}}} dq^2 \frac{d\Gamma}{dq^2}, \quad (5.66)$$

and

$$\chi_{\text{Lattice}}^2 = \sum_{i,j=1}^5 (f_{+,0}^{\text{Lattice}}(q^2) - P_N^M(q^2))_i (\text{Cov}_{ij}^{\text{Lattice}})^{-1} (f_{+,0}^{\text{Lattice}}(q^2) - P_N^M(q^2))_j. \quad (5.67)$$

For the fit, we use the spectrum (and correlation) in 13 bins of q^2 ($N_{\text{data}} = 13$) from the HFLAV group [171], which results from the average of the four most precise measurements of the differential $B \rightarrow \pi \ell \nu_\ell$ decay rate from BaBar [154, 155] and Belle [156, 157], the theoretical prediction of the partial decay rate Eq. (5.5) and the B^0 -meson lifetime τ_{B^0} . For the Lattice QCD information on the shape of the vector and scalar form factors, contained in $f_{+,0}^{\text{Lattice}}(q^2)$ in Eq. (5.67), we use the results from the FLAG group reported in 2019 [139], which are given in their Table (41). However, these are presented as a formula, resulting from fits to a z -parametrization with 5 fit parameters (those that we already use in Section 5.2), rather than as synthetic data for several values of q^2 . For our analysis, we have generated synthetic data at three representative values of q^2 from their z -fits using Eqs. (5.11) and (5.12). In particular, we have generated, respectively, 3 and 2 data points for the vector and scalar form factors ($N_{\text{Lattice}} = 5$), which we gather in Table 5.4 and use in our fits. Although synthetic data can be easily generated from the z -parameterisation results, choosing the number of points and the q^2 leading to an optimal description of the form factors is not as straightforward. In our case, we can generate 5 data points at most, as it would be inconsistent to generate more synthetic data than the independent coefficients of the z -fit; if more are generated, the resulting correlation matrix has zero eigenvalues, which implies a non-invertible covariance matrix⁶. We have checked that a z -fit with 5 parameters to the data given in Table 5.4 yields the results of Table (41) from

⁶It would be beneficial if the Lattice form factor calculations computed by any Collaboration were provided at representative q^2 values, along with the corresponding bin-to-bin correlations, as an standard, in addition to the parameterisation coefficients chosen by the group to make the fit. This would enable independent parameterisation of the results without assumptions regarding the functional form of the form factors.

FLAG review 2019 [139].

Table 5.4: Central values, uncertainties and correlation matrix for the $B \rightarrow \pi$ vector and scalar form factors, $f_{+,0}^{B \rightarrow \pi}(q^2)$, generated at three representative values of q^2 from the FLAG results [139] and used in our fits in Eqs. (5.64) and (5.74).

Form factor	q^2 [GeV ²]	Central values	Correlation matrix				
			$f_+^{B\pi}$		$f_0^{B\pi}$		
			18	22	26	18	22
$f_+^{B\pi}$	18	1.007(48)	1	0.615	0.129	0.586	0.151
	22	1.967(52)		1	0.382	0.170	0.245
	26	6.332(256)			1	0.306	0.221
$f_0^{B\pi}$	18	0.413(25)				1	0.734
	22	0.588(21)					1

Fitting with PAs

For the dominant vector form factor, we start fitting with Padé sequences of the type $P_1^M(q^2)$ and $P_2^M(q^2)$, where the poles are left free to be fitted, and we reach, respectively, $M = 3$ and $M = 2$ as the best approximants with the current data. The results of the fits for $|V_{ub}|$ and the fitted coefficients are presented in Table 5.5 for the two Padé sequences.⁷ In the table, the poles denoted by the symbol † are Froissart doublet poles⁸. The element PA $P_2^2(q^2)$ (also the $P_2^3(q^2)$) has complex-conjugate poles with an small imaginary which are pair up by a close-by zero in the numerator, thus becoming effectively a defect. However, these poles lie within the radius of convergence, indicating certain degree of unitarity violation in the data [70], since their presence is forbidden when dealing with Stieltjes functions.

We also show the coefficients of the PA $P_1^1(q^2)$ used for the description of the scalar form factor, which provides an optimal description of the data.⁹ The latter contains only 2 free parameters, a_1^0 and the effective $m_{B^*(0^+)}$ pole, as in our fits the constraint at $q^2 = 0$, *i.e.* $f_+^{B \rightarrow \pi}(0) = f_0^{B \rightarrow \pi}(0)$ (cf. Eq. (5.4)), has been implemented explicitly through $a_0^+ = a_0^0$.

Since we know the resonance mass in advance, we can fit with sequences of the type $T_1^M(q^2)$ and $P_{1,1}^M(q^2)$, where the $B^*(1^-)$ pole is fixed to the value provided in Table 5.1, $m_{B^*(1^-)} = 5.325$ GeV [140], we would have reached, respectively, $M = 3$ and $M = 2$ as the

⁷In the table, the element $P_2^3(q^2)$ is only shown for illustration.

⁸A defect pair where the pole is cancel by a near-zero in the numerator (c.f. Pade Theory Section 2.1).

⁹We have also tried a $P_1^2(q^2)$ approximant for the scalar form factor and found no impact on $|V_{ub}|$.

best approximants and obtained the results collected in Table 5.6.

In Fig. 5.6 we provide a graphical account of the convergence pattern for $|V_{ub}|$ and $f_{+,0}^{B \rightarrow \pi}(0)$ resulting from the four types of sequences we have considered. The stability observed for these quantities is quite reassuring. The values obtained for the individual χ^2 functions, χ_{data}^2 and χ_{Lattice}^2 , imply a good quality of the fits. Furthermore, we note that the approximants with two poles yield excellent values for the quantity $(\chi_{\text{data}}^2 + \chi_{\text{Lattice}}^2)/\text{dof}$. In terms of the latter, our best fit¹⁰ is obtained with a $\mathbb{P}_{1,1}^2$ approximant, which yields:

$$|V_{ub}|_{\text{PAs}} = 3.86(11) \times 10^{-3}, \quad (5.68)$$

although the values of $|V_{ub}|$ obtained with the other approximants are almost identical as it can be seen on the tables. For our best fit, $\mathbb{P}_{1,1}^2$, the quoted uncertainty on $|V_{ub}|$ is 2.9% (cf. Eq. (5.68)) and we gather the resulting fit parameters along with the correlation matrix in Table C.1 of Appendix C. Our $|V_{ub}|$ value in Eq. (5.68) is larger, and slightly more precise than, the FNAL/MILC result, $|V_{ub}| = 3.72(16) \times 10^{-3}$ [148], and the FLAG reported value, $|V_{ub}| = 3.73(14) \times 10^{-3}$ [139]. The reason for that is due to the adopted χ^2 fit function in Eq. (5.64), which we consider as more democratic. In addition, this procedure has an impact on the comparison with respect to $|V_{ub}|$ determinations from inclusive decays $B \rightarrow X_u \ell \nu_\ell$, $|V_{ub}| = 4.25(12)_{-14}^{+15}(23) \times 10^{-3}$ [140], with which our values differ by only 1.35σ . In Fig. 5.7, we show the differential branching ratio distribution (left plot) and the outputs for the vector and scalar form factors (right plot) resulting from our preferred fit $\mathbb{P}_{1,1}^2$.

We performed an analysis including only the vector form factor Lattice data into the fit, for which we have taken the limit $m_\ell \rightarrow 0$ in Eq. (5.5) and used the synthetic data from Table C.2 of Appendix C, which have been generated from the FLAG standalone z -fit to the vector form factor given in Eq. (224) in [139]. In this fit, we would have reached $M = 2$ and obtained the results shown in Table 5.7. As a matter of example, in this table we only report P_1^M sequence. Similar results and conclusions are obtained using the other approximants considered in Tables 5.5 and 5.6.

Note that $|V_{ub}|$ in this fit, $|V_{ub}| = 3.65(11) \times 10^{-3}$, shifts by about $\sim 1.3\sigma$ downwards with respect to the value given in Eq. (5.68), $|V_{ub}| = 3.86(11) \times 10^{-3}$, obtained with the scalar form factor Lattice data taken into account. The origin of this shift stems from the fact that the FLAG value for $f_{+,0}^{B \rightarrow \pi}(0)$ resulting from a standalone z -fit to the vector form factor, $f_{+,0}^{B \rightarrow \pi}(0) = 0.288(87)$ [139], which is the most relevant input for the extraction

¹⁰Our best fit is defined as the last approximant of a given sequence with all parameters different from zero at one-sigma distance and with χ^2/dof closer to 1

Table 5.5: Best fit values and uncertainties for the output quantities of our $\chi_{B\pi}^2$ fits Eq. (5.64) for Padé sequences of the type P_1^M and P_2^M .

Parameter	Element of the P_1^M sequence				Element of the P_2^M sequence			
	P_1^0	P_1^1	P_1^2	P_1^3	P_2^0	P_2^1	P_2^2	P_2^3
$ V_{ub} \times 10^3$	2.47(6)	3.66(10)	3.85(11)	3.86(11)	3.85(11)	3.88(11)	3.86(12)	3.86(12)
a_0^+	0.398(7)	0.245(8)	0.253(8)	0.240(11)	0.246(7)	0.248(7)	0.244(7)	0.242(10)
$a_1^+ \times 10^3$	—	7.9(4)	2.8(1.4)	8.1(3.3)	—	-1.9(1.4)	-3.5(9)	-2.5(4.5)
$a_2^+ \times 10^4$	—	—	2.4(6)	-3.3(3.3)	—	—	-1.7(8)	-2.5(2.4)
$a_3^+ \times 10^5$	—	—	—	1.7(1.0)	—	—	—	0.2(9)
$m_{B^*(1^-)}$ pole(s) [GeV]	5.26	5.29	5.31	5.33	5.32&7.11	5.34&6.40	†	†
$a_1^0 \times 10^2$	-1.3(1)	-0.2(1)	-0.5(1)	-0.4(1)	-0.4(1)	-0.5(1)	-0.5(1)	-0.5(1)
$m_{B^*(0^+)}$ pole [GeV]	5.17	5.72	5.45	5.43	5.47	5.39	5.38	5.38
$\chi_{\text{data}}^2 [N_{\text{data}} = 13]$	157.07	12.64	11.51	11.92	10.76	11.87	10.80	10.90
$\chi_{\text{Lattice}}^2 [N_{\text{Lattice}} = 5]$	18.19	5.15	1.72	0.67	1.53	0.75	0.42	0.34
$(\chi_{\text{data}}^2 + \chi_{\text{Lattice}}^2)/\text{dof}$	13.48	1.48	1.20	1.26	0.95	1.05	1.02	1.12

Table 5.6: Best fit values and uncertainties for the output quantities of our $\chi_{B\pi}^2$ fits Eq. (5.64) for Padé sequences of the type \mathbb{T}_1^M and $\mathbb{P}_{1,1}^M$.

Parameter	Element of the \mathbb{T}_1^M sequence				Element of the $\mathbb{P}_{1,1}^M$ sequence			
	\mathbb{T}_1^0	\mathbb{T}_1^1	\mathbb{T}_1^2	\mathbb{T}_1^3	$\mathbb{P}_{1,1}^0$	$\mathbb{P}_{1,1}^1$	$\mathbb{P}_{1,1}^2$	$\mathbb{P}_{1,1}^3$
$ V_{ub} \times 10^3$	2.19(5)	3.55(9)	3.87(11)	3.85(11)	3.85(11)	3.87(11)	3.86(11)	3.85(11)
a_0^+	0.445(6)	0.246(8)	0.256(7)	0.241(9)	0.245(7)	0.248(7)	0.247(8)	0.243(11)
$a_1^+ \times 10^3$	—	9.1(3)	1.5(1.2)	7.7(2.7)	—	-1.3(9)	-1.3(8)	3.5(11.4)
$a_2^+ \times 10^4$	—	—	3.2(5)	-2.7(2.3)	—	—	-0.3(1.0)	-1.9(3.3)
$a_3^+ \times 10^5$	—	—	—	1.5(6)	—	—	—	0.9(2.0)
$m_{B^*(1^-)}$ pole(s) [GeV]	= 5.325	= 5.325	= 5.325	= 5.325	= 5.325&7.03	= 5.325&6.64	= 5.325&6.46	= 5.325&8.97
$a_1^0 \times 10^2$	-1.9(1)	-0.4(1)	-0.5(1)	-0.4(1)	-0.4(1)	-0.5(1)	-0.4(1)	-0.4(1)
$m_{B^*(0^+)}$ pole [GeV]	4.78	5.57	5.36	5.44	5.45	5.43	5.44	5.44
$\chi_{\text{data}}^2 [N_{\text{data}} = 13]$	182.19	17.21	13.64	11.65	11.27	11.26	10.95	11.17
$\chi_{\text{Lattice}}^2 [N_{\text{Lattice}} = 5]$	41.05	11.53	1.93	0.78	1.57	1.04	1.15	0.92
$(\chi_{\text{data}}^2 + \chi_{\text{Lattice}}^2)/\text{dof}$	15.95	2.21	1.30	1.13	0.92	0.95	1.01	1.10

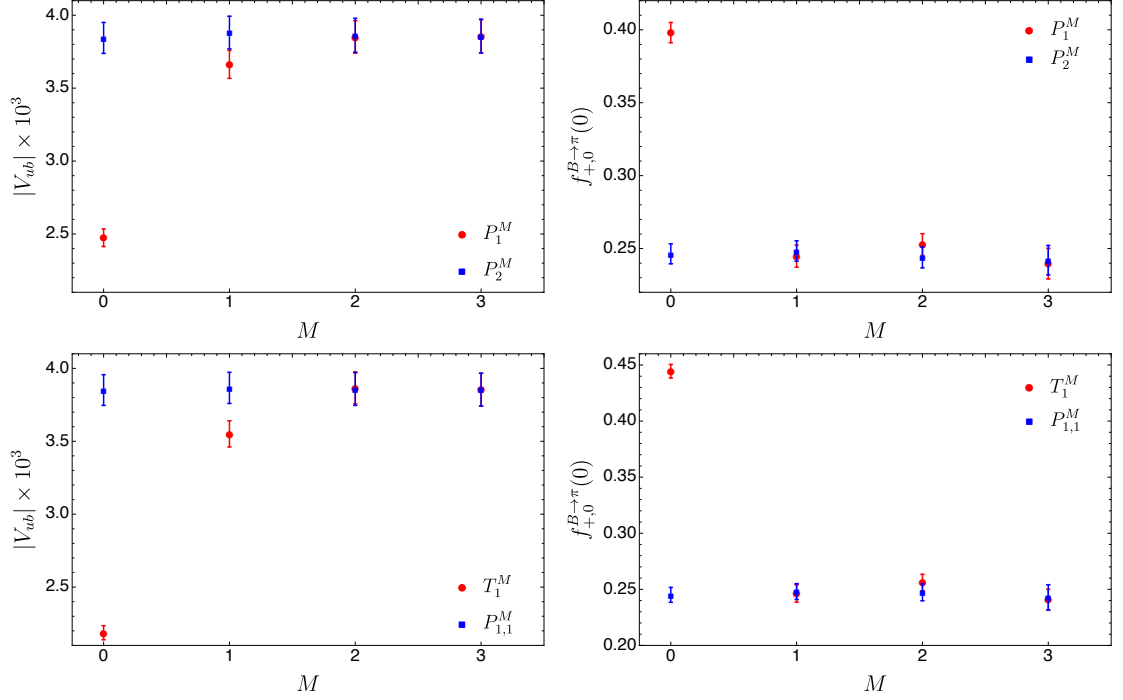


Figure 5.6: Convergence pattern of the P_1^M and P_2^M (upper panels), and T_1^M and $P_{1,1}^M$ (lower panels) sequences for $|V_{ub}|$ and $f_{+0}^{B \rightarrow \pi}(0)$ resulting from our fits in Tables 5.5 and 5.6.

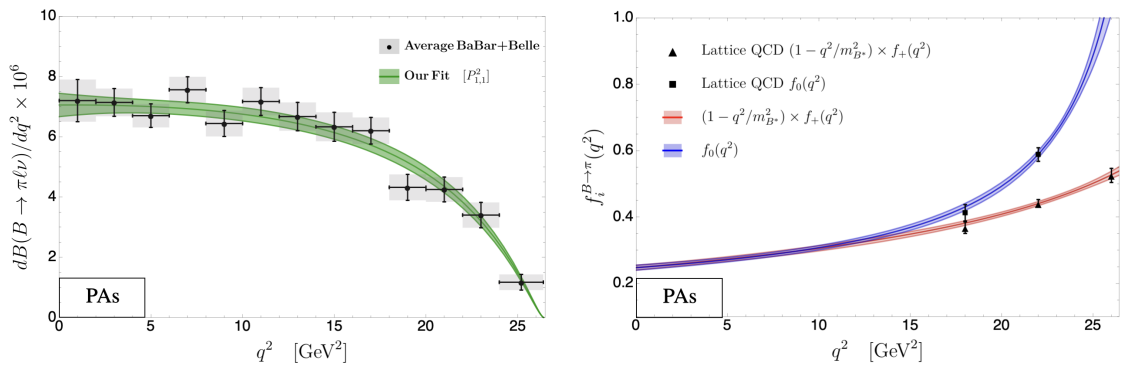


Figure 5.7: *Left*: Averaged BaBar and Belle $B \rightarrow \pi \ell \nu$ differential branching ratio distribution (gray) [171] as compared to our $P_{1,1}^2$ result (green) obtained in combined fits as presented in Table 5.6. *Right*: Output for the $B \rightarrow \pi$ vector (red) and scalar (blue) form factors.

Table 5.7: Best fit values and uncertainties for the output quantities of our $\chi^2_{B\pi}$ fits Eq. (5.64) obtained from the averaged $B \rightarrow \pi \ell \nu_\ell$ BaBar and Belle experimental data [171] in combination with the Lattice-QCD vector form factor simulations [173].

Parameter	Element of the Padé sequence			
	P_1^0	P_1^1	P_1^2	P_1^3
$ V_{ub} \times 10^3$	2.40(6)	3.56(9)	3.65(11)	3.66(11)
a_0^+	0.409(6)	0.251(8)	0.256(8)	0.260(11)
$a_1^+ \times 10^3$	—	8.3(4)	5.8(1.4)	3.5(3.5)
$a_2^+ \times 10^4$	—	—	1.2(7)	3.5(3.3)
$a_3^+ \times 10^6$	—	—	—	-6.6(9.4)
$m_{B^*(1-)} \text{ pole [GeV]}$	5.28	5.31	5.33	5.32
$\chi^2_{\text{data}} [N_{\text{data}} = 13]$	163.01	14.82	11.80	11.84
$\chi^2_{\text{Lattice}} [N_{\text{Lattice}} = 3]$	5.80	0.004	0.16	0.05
$(\chi^2_{\text{data}} + \chi^2_{\text{Lattice}})/\text{dof}$	11.25	1.06	0.92	0.99

of $|V_{ub}|$, shifts by about 1.2σ upwards with respect to their z -fits including the scalar form factor, $f_+^{B \rightarrow \pi}(0) = 0.139(90)$ [139], which is obtained with the restriction $f_+^{B \rightarrow \pi}(0) = f_0^{B \rightarrow \pi}(0)$. In this case, our $|V_{ub}|$ value is found to be in line with the HFLAV result, $|V_{ub}| = 3.70(10)(12) \times 10^{-3}$ [171], obtained from z -fits with the vector form factor only; our central value is slightly smaller due to the form adopted in Eq. (5.64).

Fitting with D-Logs

When fitting the vector form factor to experimental and lattice data using the D-Logs, we use the fit functions given by Eqs. (5.50) and (5.51), corresponding to the diagonal and subdiagonal sequences, respectively. Similarly, Eqs. (5.62) and (5.63) provide the fit functions for the scalar form factor. To minimize the number of parameters, and since the dominant contribution to the differential decay rate comes from the vector form factor, the D-Log $D_1^0(q^2)$ was used to fit the scalar form factor¹¹.

Initially, a fit was performed with all parameters left free to evaluate the behavior of the approximants as a model-independent method. The results for the coefficients obtained from this fit are presented in Table 5.8. In this case, the best fit was achieved with D_1^1 , yielding a $\chi^2/\text{dof} = 1.11$, which falls in the middle of the two best fits obtained by the PAs. In the table, the symbol † indicates a defect in the D-Logs. For instance, in the case of D_2^2 ,

¹¹Other approximants were considered but none of them generated a better fit, even considering the use of partial D-Logs and PAs.

the coefficient of the exponential is effectively zero, reducing the approximant to the values of D_2^1 . Similarly, the exponents of the second cut in D_2^N are also close to zero, which leads to the loss of two fit coefficients.

Table 5.8: Best fit values and uncertainties for the output quantities of our $\chi_{B\pi}^2$ fits Eq. (5.64) for D-Log sequences of the type D_1^N and D_2^N .

Parameter	Element of the D_1^N sequence		Element of the D_2^N sequence	
	D_1^0	D_1^1	D_2^1	D_2^2
$ V_{ub} \times 10^3$	3.89(7)	3.87(8)	3.86(8)	3.86(8)
f_0^+	39.9(2.6)	24(9)	27(13)	27(16)
a_1^+	—	0.007(5)	—	0.00(0.02) [†]
1st Br-point $\sim m_{B^*(1^-)}$ [GeV]	5.424(10)	5.389(27)	5.401(20)	5.40(5)
c_1^+	1.501(22)	1.36(10)	1.42(7)	1.42(22)
2nd Br-point [GeV]	—	—	2(3)	2(4)
c_2^+	—	—	0.05(9) [†]	0.05(19) [†]
f_0^0	0.979	1.096	1.15	1.15
1st Br-point $\sim m_{B^*(0^+)}$ [GeV]	5.03(4)	5.09(6)	5.11(7)	5.11(7)
c_1^0	0.423(28)	0.46(4)	0.47(5)	0.47(5)
$\chi_{\text{data}}^2 [N_{\text{data}} = 13]$	13.07	11.44	11.22	11.22
$\chi_{\text{Lattice}}^2 [N_{\text{Lattice}} = 5]$	0.37	0.76	0.73	0.73
$(\chi_{\text{data}}^2 + \chi_{\text{Lattice}}^2)/\text{dof}$	1.12	1.11	1.20	1.33

Table 5.9: Best fit values and uncertainties for the output quantities of our $\chi_{B\pi}^2$ fits Eq. (5.64) for Partial D-Log sequences of the type $\text{PD}_{0,1}^N$ and $\text{PD}_{1,1}^N$.

Parameter	Element of the $\text{PD}_{0,1}^N$ sequence		Element of the $\text{PD}_{1,1}^N$ sequence	
	$\text{PD}_{0,1}^0$	$\text{PD}_{0,1}^1$	$\text{PD}_{1,1}^1$	$\text{PD}_{1,1}^2$
$ V_{ub} \times 10^3$	3.59(8)	3.80(7)	3.79(7)	3.80(7)
f_0^+	20.7(4)	10.2(7)	$3(4) \times 10^{-5}$	04(25)
a_1^+	—	0.0187(16)	—	0.0186(17)
1st Br-point $\sim m_{B^*(1^-)}$ [GeV]	= 5.325	= 5.325	= 5.325	= 5.325
c_1^+	1.287(10)	1.112(19)	1.124(17)	1.112(19)
2nd Br-point [GeV]	—	—	11.6(7)	083(732)
c_2^+	—	—	2.60(24)	0.1(7) [†]
f_0^0	1.110	1.464	1.524	1.464
1st Br-point $\sim m_{B^*(0^+)}$ [GeV]	5.14(5)	5.24(5)	5.26(5)	5.24(5)
c_1^0	0.422(34)	0.54(4)	0.55(4)	0.54(4)
$\chi_{\text{data}}^2 [N_{\text{data}} = 13]$	34.40	10.14	10.09	10.14
$\chi_{\text{Lattice}}^2 [N_{\text{Lattice}} = 5]$	10.96	2.25	2.47	2.25
$(\chi_{\text{data}}^2 + \chi_{\text{Lattice}}^2)/\text{dof}$	3.49	1.03	1.14	1.24

Our best fit, D_1^1 , predicts a branch cut associated with the mass of $B^*(1^-)$ around 5.39 GeV, representing a deviation of 1.3% from the value reported by the PDG [5], with an

associated exponent of 1.36. In contrast, the resonance associated with the scalar form factor ($m_{B^*(0^+)}$) is located below the B meson mass, with a multiplicity of 0.46. Although these results deviate slightly from the values expected based on PDG and FLAG data, they remain consistent with the approximants of the same order studied in section 5.2.

A notable outcome is the highly precise determination of V_{ub} , which surpasses the precision of the fit obtained with the PAs. This result remains nearly unchanged across all the D-Logs considered.

$$|V_{ub}|_{\text{Dlogs}} = 3.87(8) \times 10^{-3}, \quad (5.69)$$

To refine the fit, we considered using Partial D-Logs, allowing us to introduce the mass of $B^*(1^-)$ at the location of the first cut. We examined the first two approximants of the sequences $\mathbb{PD}_{0,1}^N$ and $\mathbb{PD}_{1,1}^N$, with their respective coefficients listed in Table 5.9. In this case, the best fit was obtained for $\mathbb{PD}_{0,1}^1$, yielding a $\chi^2/\text{dof} = 1.03$.

Once again, we observe "D-Log-defects" in the $D_{1,1}^N$ sequence of D-Logs. For example, the partial D-Log $\mathbb{PD}_{1,1}^2$ clearly replicates the branch cuts and their multiplicities from $\mathbb{PD}_{0,1}^1$ due to $c_2^+ \simeq 0$. Additionally, the multiplicity for the cut at $m_{B^*(1^-)}^2$ decreases to 1.11, suggesting it may correspond to a pole rather than a cut. The cut associated with the scalar form factor shifts to a higher position, with its exponent adjusting to 0.5.

However, a significant deviation is observed in the central value of $|V_{ub}|$, which departs from our previous results by approximately 1σ , yet aligns more closely with values reported by FLAG ($|V_{ub}| = 3.73(14) \times 10^{-3}$) [139] and FNAL/MILC ($|V_{ub}| = 3.72(7) \times 10^{-3}$) [148], with an uncertainty of 1.8%.

$$|V_{ub}|_{\text{Partial-Dlogs}} = 3.80(7) \times 10^{-3}, \quad (5.70)$$

It is important to note that, in the case of the D-Logs, the kinematic constraint at $q^2 = 0$ does not follow a simple relationship as it does with the PAs. Instead, this condition introduces a complex interdependence among nearly all the coefficients of the approximant, resulting in high correlations between them. Consequently, this constraint evolves as the order of the approximant increases.

Figure 5.8a shows the differential branching ratio distribution, including the fit obtained with our best approximant ($f_+(q^2) \approx \mathbb{PD}_{0,1}^1(q^2)$, $f_0(q^2) \approx D_1^0(q^2)$) and the corresponding 1σ error bands, alongside the data from the BaBar and Belle collaborations [171]. In Fig. 5.8b, we present the shapes of the scalar and vector form factors using our preferred fit, along with synthesized data generated from lattice QCD results presented by FLAG [173].

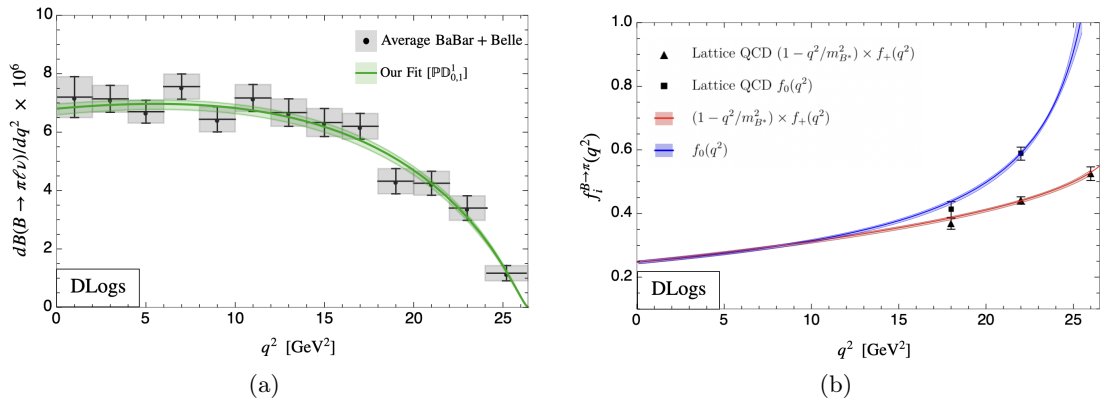


Figure 5.8: (a) Averaged BaBar and Belle $B \rightarrow \pi\ell\nu$ differential branching ratio distribution (gray) [171] as compared to our $\text{PD}_{0,1}^1$ result (green). (b) Corresponding outputs for the $B \rightarrow \pi$ vector (red) and scalar (blue) form factors.

5.4 Fits to the decay $B_s \rightarrow K\ell\nu_\ell$

For the determination of $|V_{ub}|$ from the decay $B_s \rightarrow K\ell\nu_\ell$, we follow a strategy similar to that of the previous section for $B \rightarrow \pi\ell\nu$, using recent experimental information on the decay spectrum together with the form factors shape information from theory given by the Lattice-QCD Collaborations.

The RBC/UKQCD Lattice Collaboration provides its results for both the vector and scalar form factors as synthetic, correlated data at three representative q^2 values in Tables VI and IX of Ref. [147], while the FNAL/MILC Lattice Collaboration presents their as a formula resulting from fits to a z -expansion parametrization with 8 fit coefficients, which are given in Table X of Ref. [160] and in our Table 5.2. For our study, we have generated synthetic data of the latter at four representative values of q^2 from their z -fits. In particular, we have generated 4 and 3 data points for the vector and scalar form factors, respectively, which we collect in Table 5.10. At most, we can generate 7 data points, as it would be inconsistent to generate more data than the independent coefficients of the z -fit; if more are generated, the resulting covariance matrix is not invertible. We will next use these results, which can be combined with the binned branching ratio LHCb measurements, $BR(B_s \rightarrow K^- \mu^+ \nu_\mu) = 0.36(2)(3) \times 10^{-4}$ for $q^2 < 7 \text{ GeV}^2$ and $BR(B_s \rightarrow K^- \mu^+ \nu_\mu) = 0.70(5)(6) \times 10^{-4}$ for $q^2 > 7 \text{ GeV}^2$ [161], to determine $|V_{ub}|$.

The form of the χ^2 function to be minimized, analogous to that of Eq. (5.64) for $B \rightarrow \pi$,

Table 5.10: Central values, uncertainties and correlation matrix for the $B_s \rightarrow K$ vector and scalar form factors, $f_{+,0}^{B_s \rightarrow K}(q^2)$, generated at four representative values of q^2 from the FNAL/MILC results [160] and used in our fits in Eqs. (5.71) and (5.74).

Form factor	q^2 [GeV ²]	Central values	Correlation matrix						
			$f_+^{B_s K}$				$f_0^{B_s K}$		
			17	19	21	23	17	19	21
$f_+^{B_s K}$	17	0.9268(428)	1	0.9572	0.7571	0.3615	0.6943	0.6749	0.5862
	19	1.2460(441)		1	0.9096	0.5890	0.5778	0.6214	0.6071
	21	1.7530(516)			1	0.8653	0.3985	0.5057	0.5726
	23	2.6593(820)				1	0.1885	0.3161	0.4235
$f_0^{B_s K}$	17	0.4219(196)					1	0.9499	0.7716
	19	0.4991(153)						1	0.9267
	21	0.5974(136)							1

is given by:

$$\chi_{B_s K}^2 = N \left(\frac{\chi_{\text{LHCb}}^2}{N_{\text{LHCb}}} + \frac{\chi_{\text{RBC/UKQCD}}^2}{N_{\text{RBC/UKQCD}}} + \frac{\chi_{\text{FNAL/MILC}}^2}{N_{\text{FNAL/MILC}}} \right), \quad (5.71)$$

where $N_{\text{LHCb}} = 2$ is the number of experimental points, while $N_{\text{RBC/UKQCD}} = 6$ and $N_{\text{FNAL/MILC}} = 7$ are the number of the RBC/UKQCD and FNAL/MILC Lattice points, respectively, and $N = N_{\text{LHCb}} + N_{\text{RBC/UKQCD}} + N_{\text{FNAL/MILC}}$. The first term in Eq. (5.71),

$$\chi_{\text{LHCb}}^2 = \sum_{i=1}^2 (BR_i^{\text{exp}} - BR_i^{\text{th}})^2 / \sigma_{BR_i^{\text{exp}}}^2, \quad (5.72)$$

contains the information of the LHCb experimental measurements of the branching ratio in the (uncorrelated) low and high q^2 regions, BR_i^{exp} is the measured branching ratio and $\sigma_{BR_i^{\text{exp}}}$ the corresponding uncertainty in the i -th bin, while the second and third terms include the theoretical information on the form factors from Lattice through a χ^2 function of the form:

$$\chi_{\text{Lattice}}^2 = \sum_{i,j=1}^{N_{\text{Lattice}}} (f_{+,0}^{\text{Lattice}}(q^2) - f_{+,0}(q^2))_i (\text{Cov}_{ij}^{\text{Lattice}})^{-1} (f_{+,0}^{\text{Lattice}}(q^2) - f_{+,0}(q^2))_j. \quad (5.73)$$

Fitting with PAs

Table 5.11 summarizes the best fit values for $|V_{ub}|$ and the form factor parameters for the various Padé sequences. These fits have been performed using a P_1^0 approximant for the scalar form factor and taking the $f_+^{B_s \rightarrow K}(0) = f_0^{B_s \rightarrow K}(0)$ restriction into account

Table 5.11: Best fit values and uncertainties for the output quantities of our $\chi^2_{B_s K}$ fits Eq. (5.71) for various Padé sequences.

Parameter	Padé element			
	P_1^3	P_2^2	\mathbb{T}_1^3	$\mathbb{P}_{1,1}^3$
$ V_{ub} \times 10^3$	3.58(8)	3.60(9)	3.58(8)	3.58(9)
a_0^+	0.214(5)	0.214(5)	0.214(5)	0.214(5)
$a_1^+ \times 10^3$	7.02(40)	1.12(65)	7.02(40)	6.70(5.40)
$a_2^+ \times 10^4$	-0.55(23)	0.16(20)	-0.50(14)	-0.48(46)
$a_3^+ \times 10^5$	1.12(14)	—	1.10(13)	1.04(96)
$m_{B^*(1^-)} \text{ pole(s) [GeV]}$	5.32	5.33&6.83	= 5.325	= 5.325&29.5
$m_{B^*(0^+)} \text{ pole [GeV]}$	5.70	5.69	5.70	5.70
$\chi^2_{\text{LHCb}} [N_{\text{LHCb}} = 2]$	0.14	0.20	0.14	0.15
$\chi^2_{\text{RBC/UKQCD}} [N_{\text{RBC/UKQCD}} = 6]$	3.25	3.17	3.21	3.21
$\chi^2_{\text{FNAL/MILC}} [N_{\text{FNAL/MILC}} = 7]$	4.89	5.00	4.95	4.94
$(\chi^2_{\text{LHCb}} + \chi^2_{\text{RBC/UKQCD}} + \chi^2_{\text{FNAL/MILC}})/\text{dof}$	1.03	1.05	0.92	1.03

(cf. Eq. (5.4)), thus having the $m_{B^*(0^+)}$ pole as the only free parameter in the scalar sector. We have also tried P_1^1 and P_1^2 approximants for the scalar form factors and found that the fit parameters remain stable. The values of the χ^2 functions reported in the tables imply a very good quality of the fits. For the single pole Padé sequences P_1^M and \mathbb{T}_1^M , we find the fits stabilize for $M = 3$ and the obtained $|V_{ub}|$ value, $|V_{ub}| = 3.58(8) \times 10^{-3}$, has an uncertainty of 2.2%. For the sequences with two poles, we reach P_2^2 and $\mathbb{P}_{1,1}^3$ and obtain $|V_{ub}| = 3.60(9) \times 10^{-3}$ and $|V_{ub}| = 3.58(9) \times 10^{-3}$, respectively, which is a 2.5% error. As seen, the values for $|V_{ub}|$ obtained with the various approximants are almost identical. In terms of the quantity $(\chi^2_{\text{LHCb}} + \chi^2_{\text{RBC/UKQCD}} + \chi^2_{\text{FNAL/MILC}})/\text{dof}$, the approximants P_1^3 and $\mathbb{P}_{1,1}^3$ yield the best fits. Note that the second pole of the approximant $\mathbb{P}_{1,1}^3$ is placed far away from the origin and it thus behaves as a P_1^3 . These values for $|V_{ub}|$ represent a shift of about $(1.8 - 2)\sigma$ downwards with respect to the value $|V_{ub}| = 3.86(11) \times 10^{-3}$ determined from the decay $B \rightarrow \pi\ell\nu_\ell$ (cf. Eq. (5.68)). Despite the differing results, we note that an important aspect to improve the compatibility results for $|V_{ub}|$ is the binned measurement of the $B_s \rightarrow K\ell\nu_\ell$ differential branching ratio distribution, and most importantly its low-energy region, which fixes the q^2 -dependence of the form factors at low-energies. In this sense, the experimental information is presently limited to the two LHCb experimental points, which are rather thick for an accurate extraction of the functional behavior of the form factors, specially at low-energies. Therefore, new and more precise measurements of the decay rate with a thinner resolution of the q^2 bins will definitely allow obtain more conclusive results from the $B_s \rightarrow K\ell\nu_\ell$ decay.

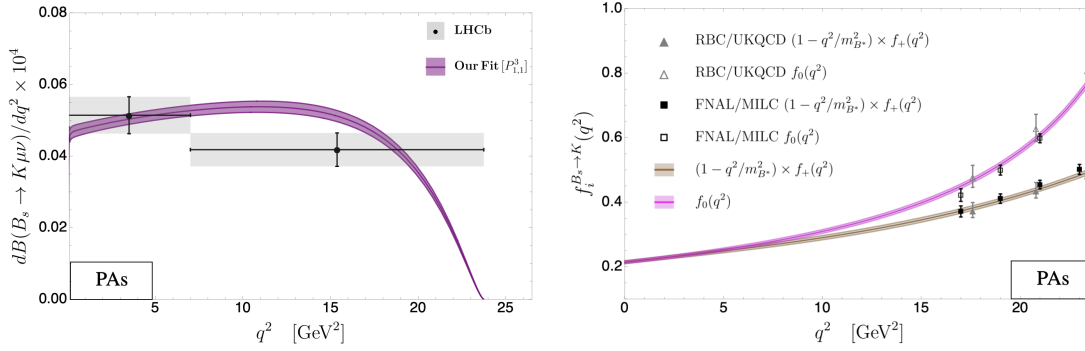


Figure 5.9: *Left:* LHCb $B_s \rightarrow K^- \mu^+ \nu_\mu$ differential branching ratio distribution (gray) [161] as compared to our best fit result (purple) obtained in combined fits as presented in Table 5.11; the two LHCb data points are placed in the middle of each bin and have been divided by the bin width. *Right:* Output for the $B_s \rightarrow K$ vector (brown) and scalar (magenta) form factors compared to the Lattice-QCD data of Ref. [147] and Table 5.10.

A graphical account of our fit with the $\mathbb{P}_{1,1}^3$ approximant is presented in Fig. 5.9 for the differential branching ratio distribution (left plot) and the output for the vector and scalar form factors (right plot), while the resulting parameters and correlation matrix of this fit is given Table C.3 of Appendix C.

Fitting with D-Logs

We present the best fits using D-Logs, including Partial D-Logs, in Table 5.12. As it happened with the PAs, the limited availability of only two experimental points within the kinematic range of $B_s \rightarrow K \mu \nu$ decay restricts the determination of a reliable value for $|V_{ub}|$. As shown in the table, the values do not stabilize across the lower-order D-Logs in any sequence, and for the partial D-Logs, the uncertainty is notably large (reaching 33% in the case of $\text{PD}_{0,1}^0$). Other coefficients do not exhibit a consistent pattern either, although the branch cut positions oscillate around values that align more accurately with the B-meson resonances.

In particular, the best fit was obtained with the D_1^1 approximant for the vector form factor, while the scalar form factor was best fitted using the D_0^1 approximant ($\chi^2/\text{dof} = 1.15$). This fit provided a prediction for $m_{B^*(0+)}$ of approximately 5.74 GeV, differing by only 0.5% from the theoretical prediction [174], with a multiplicity close to 1, indicating pole-like behavior. The predicted mass for $B^*(1^-)$ departs 0.9% from the value provided by the PDG [5]. The value of V_{ub} represents a 3σ deviation downward from the value determined by the $B \rightarrow \pi$ decay (cf. Eq. (5.70)).

Table 5.12: Best fit values and uncertainties for the output quantities of our $\chi^2_{B_s K}$ fits Eq. (5.71) for various D-Log sequences.

Parameter	D-Log approximant			
	D_1^0	D_1^1	$\text{PD}_{0,1}^0$	$\text{PD}_{0,1}^1$
$ V_{ub} \times 10^3$	3.19(7)	3.56(8)	2.49(83)	4.24(45)
f_0^+	40.51(34)	10.96(29)	16.38(9)	4.37(8)
a_1^+	—	0.027(5)	—	0.049(12)
1st Br-point ($m_{B^*(1^-)}$) [GeV]	5.42(7)	5.37(12)	= 5.325	= 5.325
c_1^+	1.49(12)	1.18(10)	1.14(2)	1.00(2)
1st Br-point $\sim m_{B^*(0^+)}$ [GeV]	5.33(5)	5.74(6)	5.37(5)	6.79(84)
c_1^0	0.62(6)	1.04(14)	0.40(23)	2.29(45)
$\chi^2_{\text{LHCb}} [N_{\text{LHCb}} = 2]$	1.03	0.37	7.77	6.46
$\chi^2_{\text{RBC/UKQCD}} [N_{\text{RBC/UKQCD}} = 6]$	6.91	4.31	58.14	2.31
$\chi^2_{\text{FNAL/MILC}} [N_{\text{FNAL/MILC}} = 7]$	11.22	4.57	149.9	20.58
$(\chi^2_{\text{LHCb}} + \chi^2_{\text{RBC/UKQCD}} + \chi^2_{\text{FNAL/MILC}})/\text{dof}$	2.12	1.15	21.58	3.26

5.5 Combined fits to the decays $B \rightarrow \pi\ell\nu_\ell$ and $B_s \rightarrow K\ell\nu_\ell$

In the previous Sections 5.3 and 5.4 we have extracted $|V_{ub}|$ and the corresponding form factor parameters from individual fits to the decays $B \rightarrow \pi\ell\nu_\ell$ and $B_s \rightarrow K^-\mu^+\nu_\mu$ experimental data combined with the Lattice-QCD information on the corresponding vector and scalar form factors, using both PAs and D-Logs. In this section, we explore the potential of performing simultaneous fits to all experimental and theoretical information on both exclusive decays to determine $|V_{ub}|$. For that, we proceed in a similar fashion as in the previous cases, Eqs. (5.64) and (5.71), and minimize the following χ^2 -function:

$$\chi^2 = N \left(\frac{\chi^2_{\text{BaBar+Belle}}}{N_{\text{BaBar+Belle}}} + \frac{\chi^2_{\text{FLAG}}}{N_{\text{FLAG}}} + \frac{\chi^2_{\text{LHCb}}}{N_{\text{LHCb}}} + \frac{\chi^2_{\text{RBC/UKQCD}}}{N_{\text{RBC/UKQCD}}} + \frac{\chi^2_{\text{FNAL/MILC}}}{N_{\text{FNAL/MILC}}} \right), \quad (5.74)$$

where the first two terms contain the information on the decay $B \rightarrow \pi\ell\nu_\ell$ channel, while the three other include that of the $B_s \rightarrow K^-\mu^+\nu_\mu$ channel, with $N_{\text{BaBar+Belle}} = 13$, $N_{\text{FLAG}} = 5$, $N_{\text{LHCb}} = 2$, $N_{\text{RBC/UKQCD}} = 6$, $N_{\text{FNAL/MILC}} = 7$ and $N = N_{\text{BaBar+Belle}} + N_{\text{FLAG}} + N_{\text{LHCb}} + N_{\text{RBC/UKQCD}} + N_{\text{FNAL/MILC}}$. This definition equally weight each data set and prevents sets with a smaller data points, such as the $B_s \rightarrow K\ell\nu_\ell$ spectra, from being dominated by sets with a larger data points, such as the $B \rightarrow \pi\ell\nu_\ell$ spectra.

Fitting with PAs

As in the preceding sections, we have tried various Padé sequences. Here, however, we only show our results for $|V_{ub}|$ and the form factor parameters resulting from the partial Padé sequence $\mathbb{P}_{1,1}^M$, which yielded the best fit results in our previous individual analyses. We reach $M = 2$ and $M = 3$ for the $B \rightarrow \pi$ and $B_s \rightarrow K$ vector form factors, respectively. The resulting fit parameters and the correlation matrix are presented in Table 5.13¹², which have been obtained taking into account the restrictions $f_+^{B \rightarrow \pi}(0) = f_0^{B \rightarrow \pi}(0)$ and $f_+^{B_s \rightarrow K}(0) = f_0^{B_s \rightarrow K}(0)$ simultaneously. The value for the quantity $(\chi_{\text{BaBar+Belle}}^2 + \chi_{\text{FLAG}}^2 + \chi_{\text{LHCb}}^2 + \chi_{\text{RBC/UKQCD}}^2 + \chi_{\text{FNAL/MILC}}^2)/\text{dof} = 1.08$ indicates a good quality of the fit. The resulting value for $|V_{ub}|$ from the combined analysis is found to be:

$$|V_{ub}|_{\text{PAs-comb}} = 3.68(5) \times 10^{-3}, \quad (5.75)$$

which is only a 1.4% error.

We would like to note, on the one hand, that our $|V_{ub}|$ result in Eq. (5.75) corresponds to the most precise determination of $|V_{ub}|$ to date, and that this value is shifted about 1.4σ downwards with respect to $|V_{ub}| = 3.86(11) \times 10^{-3}$ extracted from $B \rightarrow \pi \ell \nu_\ell$ alone (cf. Table 5.5), and about 1σ upwards with respect to $|V_{ub}| = 3.58(9) \times 10^{-3}$ obtained from the individual analysis of the $B_s \rightarrow K \ell \nu_\ell$ channel (cf. Table 5.11). On the other hand, our determination is far more precise than both the leptonic $B \rightarrow \tau \nu_\tau$, $|V_{ub}| = 4.01(9)(63) \times 10^{-3}$ [139], and the inclusive, $|V_{ub}| = 4.25(12)_{-14}^{+15}(23) \times 10^{-3}$ [140], determinations, and that the tension between our $|V_{ub}|$ result in Eq. (5.75) and the latter is of about 1.8σ .¹³

The results of the combined fit are plotted in Fig. 5.10 for the differential $B \rightarrow \pi \ell \nu_\ell$ (left plot) and $B_s \rightarrow K^- \mu^+ \nu_\mu$ (right plot) branching ratio distributions, and in Fig. 5.11 for the corresponding vector and scalar form factors.

Fitting with D-Logs

For the final stage of the analysis, we explored various D-Log sequences, including partial D-Logs and D-Logs with $N = 3$, applied independently to each channel. However, we present only the results for $|V_{ub}|$ and the form factor parameters obtained from the approximant $f_{+/0}(q^2) \approx D_1^1(q^2)_{+/0}$, as this yielded the best fit across all combined analyses. This choice results in 13 fitting parameters, which matches the number of parameters used in the PAs.

¹²In the table, we use c_i to denote the Padé approximant fit parameters of the $B_s \rightarrow K$ form factors.

¹³ 3.4σ if the inclusive determination $|V_{ub}| = 4.32(12)_{-13}^{+12} \times 10^{-3}$ [175] is considered instead, and 1.5σ with respect to the preliminary value $|V_{ub}| = 4.06(9)(16)(15) \times 10^{-3}$ in [176].

Table 5.13: Best fit values using PAs as fitting functions, uncertainties and correlation matrix for the output quantities of our χ^2 fits Eq. (5.74) obtained from a combined fit to the averaged $B \rightarrow \pi \ell \nu_\ell$ BaBar and Belle [171] and the $B_s \rightarrow K^- \mu^+ \nu_\mu$ LHCb [161] experimental data in combination with the Lattice-QCD $B \rightarrow \pi$ [139] and $B_s \rightarrow K$ [147, 160] vector and scalar form factors simulations.

Parameter	Central value	Correlation matrix												
$ V_{ub} \times 10^3$	3.68(5)	1	-0.404	0.086	0.221	-0.185	0.082	-0.082	-0.610	-0.239	0.138	-0.150	0.203	-0.386
a_0^+	0.255(5)		1	-0.432	0.500	-0.405	-0.745	-0.564	0.246	0.096	-0.056	0.061	-0.082	0.156
$a_1^+ \times 10^3$	-1.36(60)			1	0.055	-0.331	0.186	0.048	-0.053	-0.021	0.012	-0.013	0.018	-0.033
$a_2^+ \times 10^4$	-0.66(68)				1	-0.957	-0.750	-0.821	-0.135	-0.053	0.031	-0.033	0.045	-0.085
$m_{B^{*(1-)}} \text{ pole(s) [GeV]}$	= 5.325&6.24					1	0.685	0.775	0.113	0.044	-0.026	0.028	-0.038	0.071
$a_0^0 \times 10^2$	-0.46(6)						1	0.962	-0.050	-0.020	0.011	-0.012	0.017	-0.032
$m_{B^{*(0+)}} \text{ pole(s) [GeV]}$	5.45							1	0.050	0.020	-0.011	0.012	-0.017	0.032
c_0^+	0.211(3)								1	-0.052	0.095	-0.046	0.030	0.765
$c_1^+ \times 10^3$	4.96(2.32)									1	-0.975	0.968	-0.992	-0.121
$c_2^+ \times 10^4$	-0.37(26)										1	-0.994	0.989	0.185
$c_3^+ \times 10^5$	0.81(43)											1	-0.990	-0.115
$m_{B^{*(1-)}} \text{ pole(s) [GeV]}$	= 5.325&12.13												1	0.088
$m_{B^{*(0+)}} \text{ pole(s) [GeV]}$	5.69													1

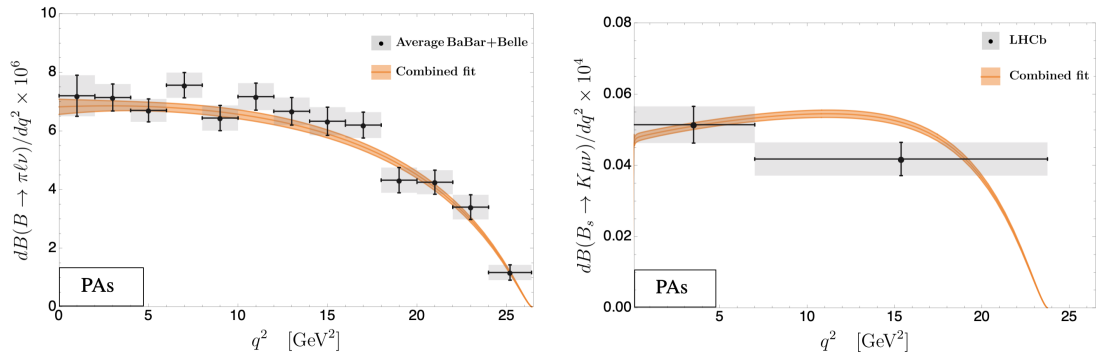


Figure 5.10: Averaged BaBar and Belle $B \rightarrow \pi \ell \nu$ (left) [171] and LHCb $B_s \rightarrow K^- \mu^+ \nu_\mu$ (right) [161] differential branching ratio distributions (gray) as compared to our best fit result using PAs (orange) obtained in combined fits to both decays as presented in Table 5.13. The two LHCb data points are placed in the middle of each bin and have been divided by the bin width.

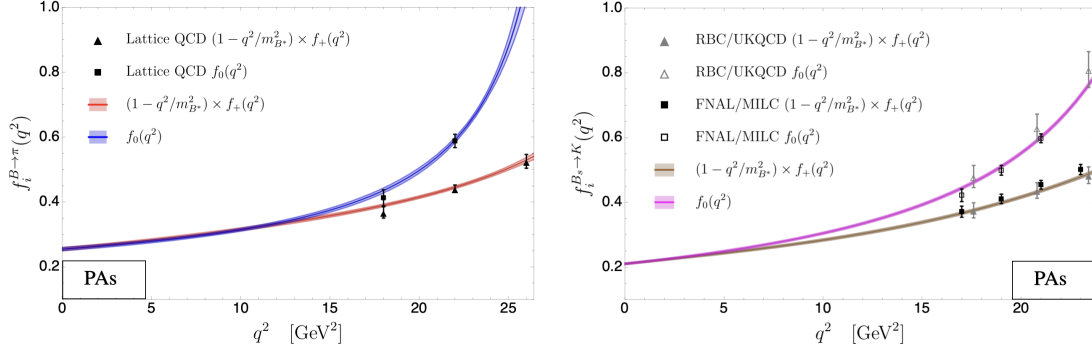


Figure 5.11: Lattice-QCD data for the $B \rightarrow \pi$ (left plot) and $B_s \rightarrow K$ (right plot) vector and scalar form factors compared to our best fit results using PAs obtained in combined fits as presented in Table 5.13.

Table 5.14: Best fit values using D-Log fitting functions, uncertainties and correlation matrix for the output quantities of our χ^2 fits Eq. (5.74) obtained from a combined fit to the averaged $B \rightarrow \pi \ell \nu_\ell$ BaBar and Belle [171] and the $B_s \rightarrow K^- \ell^+ \nu_\ell$ LHCb [161] experimental data in combination with the Lattice-QCD $B \rightarrow \pi$ [139] and $B_s \rightarrow K$ [147, 160] vector and scalar form factors simulations.

Parameter	Central value	Correlation matrix												
$ V_{ub} \times 10^3$	3.72(6)	1.00	0.982	-0.981	0.983	0.983	-0.701	0.764	-0.658	-0.503	0.831	0.928	0.986	0.991
f_0^+	19.5(5.0)		1.00	-1.00	1.00	1.00	-0.560	0.634	-0.506	-0.337	0.712	0.842	1.00	0.999
a_1^+	0.0092(36)			1.000	-1.00	-1.00	0.555	-0.630	0.501	0.332	-0.708	-0.839	-1.00	-0.998
$(b_1^+)^{0.5} \sim m_{B^*(1-)}$	5.37(2)				1.00	1.00	-0.565	0.639	-0.511	-0.343	0.716	0.845	1.00	0.999
c_1^+	1.29(7)					1.000	-0.563	0.637	-0.509	-0.341	0.714	0.844	1.00	0.999
$(b_1^0)^{0.5} \sim m_{B^*(0^+)}$	5.09(5)						1.000	0.999	-0.577	0.650	-0.524	-0.356	0.726	0.853
c_1^0	0.44(3)							1.000	-0.601	0.673	-0.550	-0.385	0.747	0.869
f_0^{++}	7.77(63)								1.000	-0.996	0.985	0.969	-0.963	-0.907
\tilde{a}_1^+	0.035(2)									1.00	-0.973	-0.942	0.976	0.939
$(\tilde{b}_1^+)^{0.5} \sim m_{B^*(1-)}$	5.355(3)										1.000	0.968	-0.965	-0.891
\tilde{c}_1^+	1.11(2)											1.000	-0.882	-0.779
$(\tilde{b}_1^0)^{0.5} \sim m_{B^*(0^+)}$	6.00(7)												1.000	0.978
\tilde{c}_1^0	1.35(8)													1.000

The resulting fit parameters and the correlation matrix are presented in Table 5.14¹⁴. It is important to note that significant correlations arise between the coefficients for each channel, as the constraints $f_{B \rightarrow \pi}^+(0) = f_{B \rightarrow \pi}^0(0)$ and $f_{B_s \rightarrow K}^+(0) = f_{B_s \rightarrow K}^0(0)$ create interdependencies among their parameters. For instance, in the case of D_1^+ , the constraint takes the form: $f_0^0 = f_0^+(b_1^0)c_1^0(b_1^+)^{-c_1^+}$.

However, the value of $(\chi_{\text{BaBar+Belle}}^2 + \chi_{\text{FLAG}}^2 + \chi_{\text{LHCb}}^2 + \chi_{\text{RBC/UKQCD}}^2 + \chi_{\text{FNAL/MILC}}^2)/\text{dof} = 1.36$ indicates that quality of the fit is not the best comparing with individuals fitting and

¹⁴In the table, \tilde{f} , \tilde{a} , \tilde{b} , and \tilde{c} denote the coefficients of the D-Logs used to fit the $B_s \rightarrow K$ form factors.

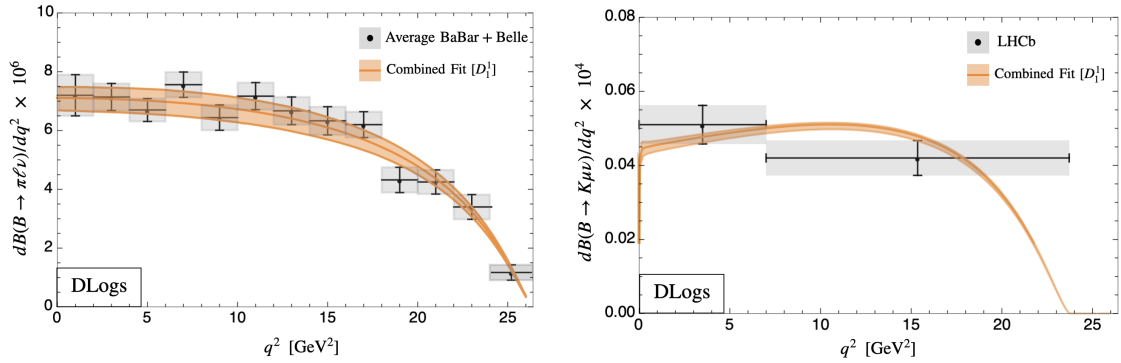


Figure 5.12: Averaged BaBar and Belle $B \rightarrow \pi \ell \nu$ (left) [171] and LHCb $B_s \rightarrow K^- \mu^+ \nu_\mu$ (right) [161] differential branching ratio distributions (gray) as compared to our best fit result using D-logs (orange) obtained in combined fits to both decays as presented in Table 5.14. The two LHCb data points are placed in the middle of each bin and have been divided by the bin width.

the combined fit with PAs. The resulting value for $|V_{ub}|$ from this combined analysis is:

$$|V_{ub}|_{\text{Dlogs-comb}} = 3.72(6) \times 10^{-3}, \quad (5.76)$$

this value has an uncertainty of 1.6%, slightly higher than the one obtained by PAs, but still very precise. This value consistent with $|V_{ub}|$ extracted from $B \rightarrow \pi \ell \nu_\ell$ fitting with D-Logs (shifted 1σ downwards, cf. Table 5.9), and is shifted about 2σ upwards with respect to $|V_{ub}| = 3.56(8) \times 10^{-3}$ obtained from the individual analysis of the $B_s \rightarrow K \ell \nu_\ell$ channel (cf. Table 5.12).

Corresponding results of the combined fit using D-Logs are plotted in Fig. 5.12 where the differential branching ratio distributions for $B \rightarrow \pi \ell \nu_\ell$ is shown in the left plot and $B_s \rightarrow K^- \mu^+ \nu_\mu$ in the right plot. Additionally, corresponding outputs for the vector and scalar form factors in both channels are shown in Fig. 5.13.

Concerning the form factor values at $q^2 = 0$, we obtain:

$$\begin{aligned} f_{+,0}^{B\pi}(0) &= 0.255(5), & f_{+,0}^{B_s K}(0) &= 0.211(3), & \text{for PAs,} \\ f_{+,0}^{B\pi}(0) &= 0.255(92), & f_{+,0}^{B_s K}(0) &= 0.185(18), & \text{for D-Logs,} \end{aligned}$$

which can be compared with the output values: $f_{+,0}^{B\pi}(0) = 0.253(11)$ [148] and $f_{+,0}^{B_s K}(0) = 0.135(50)$ [160] from the FNAL/MILC Lattice Collaborations; $f_{+,0}^{B\pi}(0) = 0.26_{-0.03}^{+0.04}$ [177] and $f_{+,0}^{B_s K}(0) = 0.30_{-0.03}^{+0.04}$ [178], $f_{+,0}^{B\pi}(0) = 0.301(23)$ and $f_{+,0}^{B_s K}(0) = 0.336(23)$ [179], and $f_{+,0}^{B\pi}(0) = 0.252_{-0.028}^{+0.019}$ [145] from light-cone sum rules; $f_{+,0}^{B\pi}(0) = f_{+,0}^{B_s K}(0) = 0.26_{-0.03}^{+0.04} \pm 0.02$

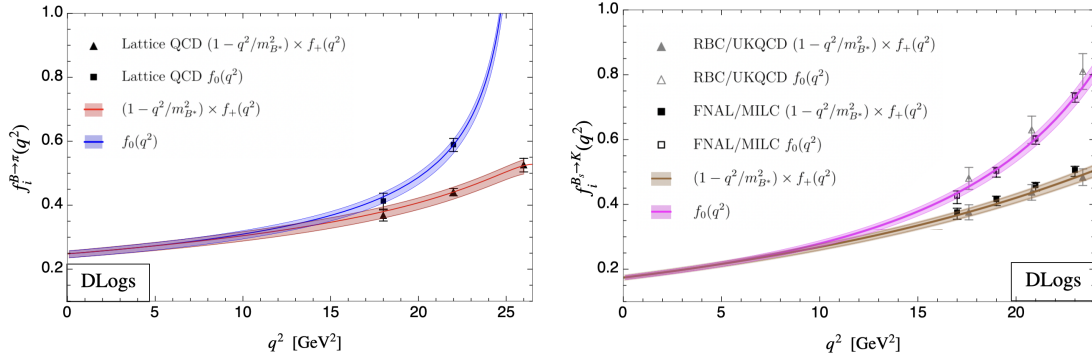


Figure 5.13: Lattice-QCD data for the $B \rightarrow \pi$ (left plot) and $B_s \rightarrow K$ (right plot) vector and scalar form factors compared to our best fit results obtained using D-Logs in combined fits as presented in Table 5.14.

from perturbative QCD [180]; and $f_{+,0}^{B_s K}(0) = 0.284(14)$ from relativistic quark model [181].

The results given in Tables 5.13 and 5.14 correspond, to the best of our knowledge, to the first correlated results between the $B \rightarrow \pi$ and $B_s \rightarrow K$ form factors, which can serve as guidance for those Lattice Collaborations that are planning making available the full theoretical correlation between form factors for different process in their final results [160].

5.6 Phenomenological Applications

For the subsequent analysis, we use the form factor results obtained from the combined fit with PAs, as they provide the most precise determination of $|V_{ub}|$. In Fig. 5.14 we present results for the quantity:

$$R_i(q^2) = \frac{f_i^{B_s K}(q^2)}{f_i^{B \pi}(q^2)} - 1, \quad (5.77)$$

with $i = +, 0$, which provides a measure of $SU(3)$ -breaking considering that in the $SU(3)$ limit, *i.e.* $m_d = m_s$, the $B \rightarrow \pi$ and $B_s \rightarrow K$ form factors should be identical. As seen, while the results for $R_+(q^2)$ (cyan) and $R_0(q^2)$ (purple) are similar at low energies ($q^2 \lesssim 5 \text{ GeV}^2$), $R_0(q^2)$ is larger than $R_+(q^2)$ at higher energies, and the deviations from unity are consistent with the simple counting $(m_s - m_d)/\Lambda_{\text{QCD}} \sim 20\%$.

As a benefit of our results of Table 5.13, we provide calculations for different phenomenological observables such as total decay rates, ratio of τ -to- μ differential decay rates or the forward-backward asymmetry, and its normalized version.

Integrating the differential decay rates (cf. Eq. (5.5)) over the kinematically-allowed q^2

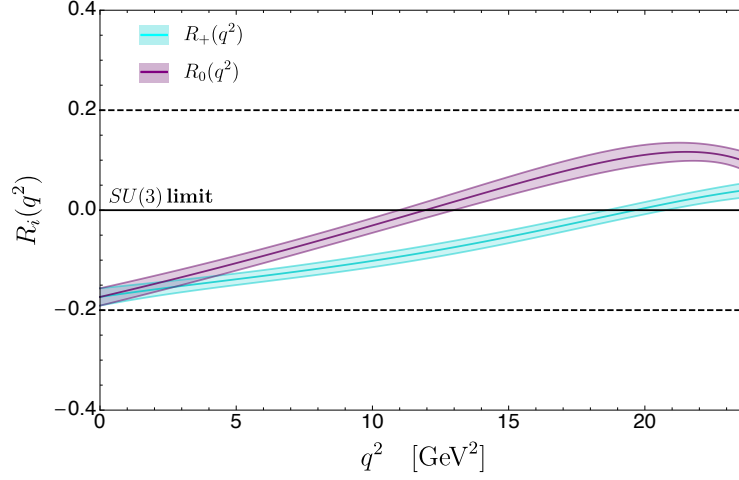


Figure 5.14: $SU(3)$ -breaking ratios $R_+(q^2)$ (cyan) and $R_0(q^2)$ (purple) (cf. Eq. (5.77)) using our determinations of the $B \rightarrow \pi$ and $B_s \rightarrow K$ vector and scalar form factors from Table 5.13.

ranges, and dividing by $|V_{ub}|^2$, we obtain:

$$\Gamma(B \rightarrow \pi \mu \nu_\mu) / |V_{ub}|^2 = 6.90(16) \text{ ps}^{-1}, \quad (5.78)$$

$$\Gamma(B \rightarrow \pi \tau \nu_\tau) / |V_{ub}|^2 = 4.55(9) \text{ ps}^{-1}, \quad (5.79)$$

$$\Gamma(B_s \rightarrow K \mu \nu_\mu) / |V_{ub}|^2 = 5.31(13) \text{ ps}^{-1}, \quad (5.80)$$

$$\Gamma(B_s \rightarrow K \tau \nu_\tau) / |V_{ub}|^2 = 3.70(8) \text{ ps}^{-1}, \quad (5.81)$$

with errors of only about 2%.

The τ -to- μ q^2 -dependent ratio of differential decay rates

$$\mathcal{R}_{\pi(K)}^{\tau/\mu}(q^2) = \frac{d\Gamma(B_{(s)} \rightarrow \pi(K) \tau \nu_\tau) / dq^2}{d\Gamma(B_{(s)} \rightarrow \pi(K) \mu \nu_\mu) / dq^2}, \quad (5.82)$$

and its integrated form

$$R_{\pi(K)}^{\tau/\mu} = \frac{\int_{m_\tau^2}^{(m_{B_{(s)}} - m_{\pi(K)})^2} dq^2 d\Gamma(B_{(s)} \rightarrow \pi(K) \tau \nu_\tau) / dq^2}{\int_{m_\mu^2}^{(m_{B_{(s)}} - m_{\pi(K)})^2} dq^2 d\Gamma(B_{(s)} \rightarrow \pi(K) \mu \nu_\mu) / dq^2}, \quad (5.83)$$

can be used for precise Standard Model test that is independent of $|V_{ub}|$. Fig. 5.15 shows our predictions for Eq. (5.82) using our $B \rightarrow \pi \ell \nu_\ell$ and $B_s \rightarrow K \mu \nu_\mu$ form factor outputs

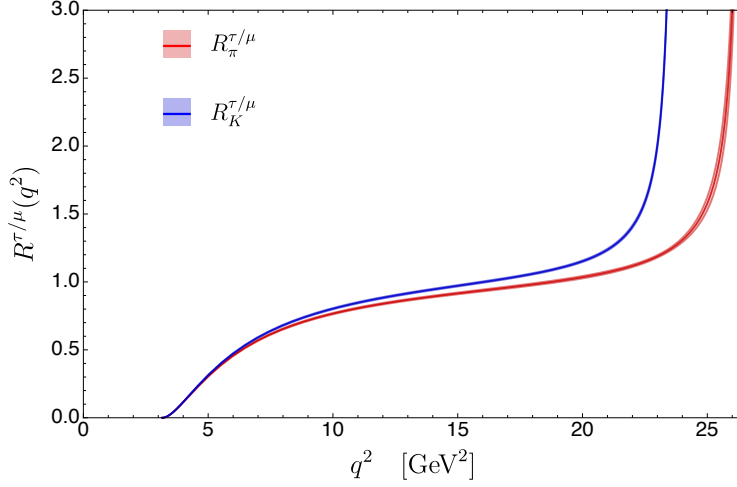


Figure 5.15: Standard Model ratio of differential τ -to- μ decay rates Eq. (5.82) using our determinations of the $B \rightarrow \pi$ and $B_s \rightarrow K$ vector and scalar form factors from Table 5.13.

from Table 5.13, while our numerical predictions for Eq. (5.83) are found to be:

$$R_{\pi}^{\tau/\mu} = 0.660(5), \quad (5.84)$$

$$R_K^{\tau/\mu} = 0.697(3), \quad (5.85)$$

which are only 1% error.

These values are found to be in agreement with, but more precise than, $R_{\pi}^{\tau/\mu} = 0.69(19)$ and $R_K^{\tau/\mu} = 0.77(12)$ from Ref. [147], and $R_K^{\tau/\mu} = 0.77(6)$ from Ref. [160]¹⁵.

Concerning the forward-backward asymmetry, A_{FB} , it is a quantity sensitive to the mass of the final-state charged lepton and its theoretical expression is given by:

$$\begin{aligned} A_{FB}^{B_{(s)} \rightarrow \pi(K) \ell \nu_{\ell}}(q^2) &\equiv \left(\int_0^1 - \int_{-1}^0 \right) d \cos \theta_{\ell} \frac{d^2 \Gamma(B_{(s)} \rightarrow \pi(K) \ell \nu_{\ell})}{dq^2 d \cos \theta_{\ell}} \\ &= \frac{G_F^2 |V_{ub}|^2}{32 \pi^3 m_{B_{(s)}}} \left(1 - \frac{m_{\ell}^2}{q^2} \right)^2 |\vec{p}_{\pi(K)}|^2 \\ &\times \frac{m_{\ell}^2}{q^2} (m_{B_{(s)}}^2 - m_{\pi(K)}^2) \text{Re}[f_+(q^2) f_0(q^2)], \end{aligned} \quad (5.86)$$

where θ_{ℓ} is the angle between the charged-lepton and the $B_{(s)}$ -meson momenta in the q^2

¹⁵In [160], the value $R_K^{\tau/\mu} = 0.836(34)$ is reported, which corresponds to taking m_{τ}^2 as the lower limit of integration in the denominator of Eq. (5.83).

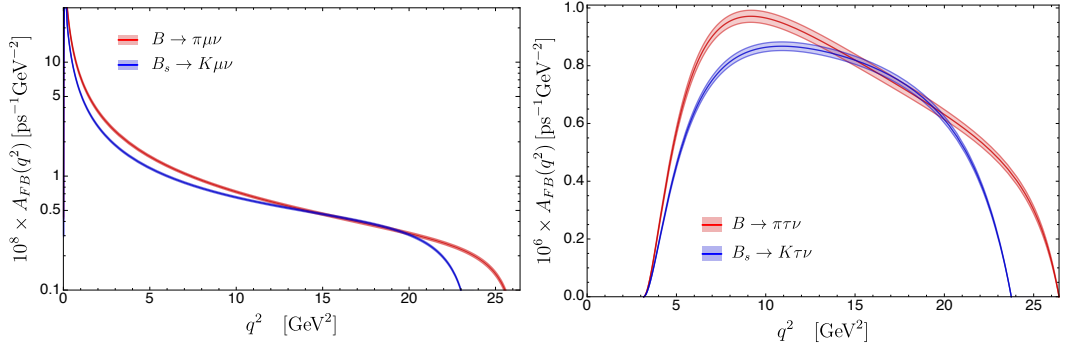


Figure 5.16: Predictions for the forward-backward asymmetry Eq. (5.86) for $B \rightarrow \pi\mu\nu$ and $B_s \rightarrow K\mu\nu$ (left), and $B \rightarrow \pi\tau\nu$ and $B_s \rightarrow K\tau\nu$ (right), using our fit results from Table 5.13.

rest frame. In Fig. 5.16, we show our predictions for A_{FB} using our best fit results taken from Table 5.13.

Integrating over the corresponding kinematic q^2 ranges, and dividing by $|V_{ub}|^2$, we obtain:

$$\int_{m_\mu^2}^{(m_B - m_\pi)^2} dq^2 A_{FB}^{B \rightarrow \pi\mu\nu}(q^2) / |V_{ub}|^2 = 0.034(1) \text{ ps}^{-1}, \quad (5.87)$$

$$\int_{m_\tau^2}^{(m_B - m_\pi)^2} dq^2 A_{FB}^{B \rightarrow \pi\tau\nu}(q^2) / |V_{ub}|^2 = 1.16(3) \text{ ps}^{-1}, \quad (5.88)$$

$$\int_{m_\mu^2}^{(m_{B_s} - m_K)^2} dq^2 A_{FB}^{B_s \rightarrow K\mu\nu}(q^2) / |V_{ub}|^2 = 0.0255(6) \text{ ps}^{-1}, \quad (5.89)$$

$$\int_{m_\tau^2}^{(m_{B_s} - m_K)^2} dq^2 A_{FB}^{B_s \rightarrow K\tau\nu}(q^2) / |V_{ub}|^2 = 0.99(2) \text{ ps}^{-1}, \quad (5.90)$$

with errors of about 3%. While these values are in general agreement with, but more precise than, those in Ref. [147], our results show a difference of about 1.5σ with [160]. Finally, the normalized forward-backward asymmetry,

$$\bar{A}_{FB}^{B_{(s)} \rightarrow \pi(K)\ell\nu\ell}(q^2) \equiv \frac{\int_{m_\ell^2}^{(m_{B_{(s)}}^2 - m_{\pi(K)}^2)^2} dq^2 A_{FB}^{B_{(s)} \rightarrow \pi(K)\ell\nu\ell}(q^2)}{\int_{m_\ell^2}^{(m_{B_{(s)}}^2 - m_{\pi(K)}^2)^2} dq^2 d\Gamma(B_{(s)} \rightarrow \pi(K)\ell\nu\ell) / dq^2}, \quad (5.91)$$

is an interesting observable as it is independent of $|V_{ub}|$. Our predictions are show in

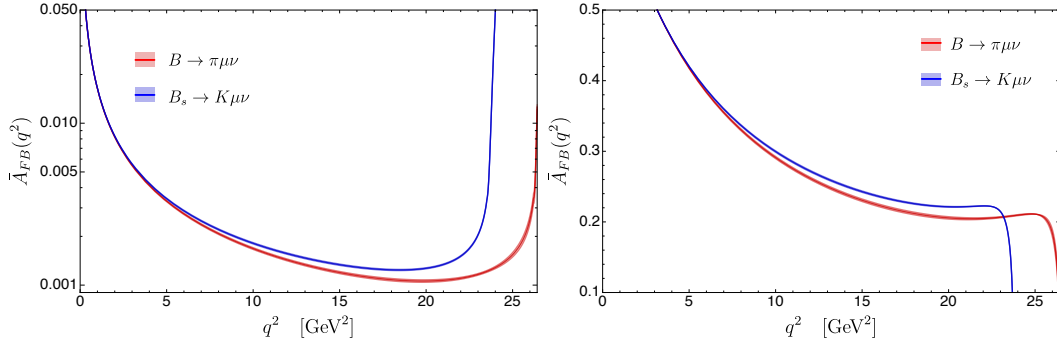


Figure 5.17: Predictions for the normalized forward-backward asymmetry Eq. (5.91) for $B \rightarrow \pi\mu\nu$ and $B_s \rightarrow K\mu\nu$ (left), and $B \rightarrow \pi\tau\nu$ and $B_s \rightarrow K\tau\nu$ (right), using our fit results from Table 5.13.

Fig. 5.17, whereas integrating Eq. (5.91) over the allowed q^2 ranges we find:

$$\bar{A}_{FB}^{B \rightarrow \pi\mu\nu} = 0.0049(1), \quad (5.92)$$

$$\bar{A}_{FB}^{B \rightarrow \pi\tau\nu} = 0.255(1), \quad (5.93)$$

$$\bar{A}_{FB}^{B_s \rightarrow K\mu\nu} = 0.0048(1), \quad (5.94)$$

$$\bar{A}_{FB}^{B_s \rightarrow K\tau\nu} = 0.2684(9), \quad (5.95)$$

with errors of about 2% and 1% for μ and τ , respectively. While these values are found to be in agreement with Ref. [147], our results are more precise. With respect to [160], our results differ by about $\sim 1.6 - 2.1\sigma$ for $\bar{A}_{FB}^{B_s \rightarrow K\mu\nu}$ and $\bar{A}_{FB}^{B_s \rightarrow K\tau\nu}$, respectively.

5.7 Summary & highlights

In this chapter we have explored the role of the decay $B_s \rightarrow K\ell\nu_\ell$ in complementing the traditional channel $B \rightarrow \pi\ell\nu_\ell$ in the determination of the CKM element $|V_{ub}|$. The motivation of this study was the first reported measurement of the branching ratio of the decay $B_s \rightarrow K^- \mu^+ \nu_\mu$ by the LHCb Collaboration [161], making this analysis of timely interest. Our analysis has been based on two principal techniques; the approximation method of Padé approximants and D-Log Padé approximants to the corresponding form factors, and proceeded in three steps. First, we used the most precise measurements of the differential $B \rightarrow \pi\ell\nu_\ell$ branching ratio distribution given by BaBar and Belle, along with the Lattice-QCD calculations of the $B \rightarrow \pi$ vector and scalar form factors, to extract $|V_{ub}|$ from a combined fit which makes use of both information sets in a democratic way.

As a result of this exercise we have obtained $|V_{ub}| = 3.86(11) \times 10^{-3}$ (cf. Eq. (5.68)) for PAs and $|V_{ub}| = 3.80(7) \times 10^{-3}$ for D-Logs (cf. Eq. (5.70)). We note that our result for $|V_{ub}|$ differs about $1.35\sigma - 2.1\sigma$ with the determination from inclusive decays $B \rightarrow X_u \ell \nu_\ell$, $|V_{ub}| = 4.25(12)_{-14}^{+15}(23) \times 10^{-3}$ [140],¹⁶ confirming the trend of obtaining higher values of $|V_{ub}|$ from recent exclusive $B \rightarrow \pi \ell \nu_\ell$ determinations [182, 183]. Second, we have determined $|V_{ub}|$ from the decay $B_s \rightarrow K \ell \nu_\ell$ performing combined fits to the experimental LHCb data and Lattice input on the $B_s \rightarrow K$ form factors. Our fits yield $|V_{ub}| = 3.58(9) \times 10^{-3}$ using PAs and $|V_{ub}| = 3.56(8) \times 10^{-3}$ using D-Logs. Also was determined their form factor parameters and their correlation matrix given in Appendix C. This is a relevant result, as the central $|V_{ub}|$ value from $B_s \rightarrow K \ell \nu_\ell$ suffers a downwards shift of about 1.9σ in the case of PAs and 3σ in the case of D-Logs with respect to the one obtained from $B \rightarrow \pi \ell \nu_\ell$, thus increasing the difference with respect to the determination from inclusive decays to 2.1σ . We traced back these differences to the impact of existing experimental data used in each channel: Lattice input in form factors in both channels tend to yield values for $|V_{ub}|$ around 3.6×10^{-3} while experimental data seem to prefer higher values of around $|V_{ub}| = 3.9 \times 10^{-3}$. Since experimental data for the $B_s \rightarrow K$ is scarce, that channel is dominated by Lattice input thus confronting the $B \rightarrow \pi$ one. Third, and last, we have performed a simultaneous analysis to all available experimental and Lattice-QCD information on both $B \rightarrow \pi \ell \nu_\ell$ and $B_s \rightarrow K^- \mu^+ \nu_\mu$ decays. The resulting fit yields $|V_{ub}|_{PAs} = 3.68(5) \times 10^{-3}$, which is a 1.4% error and differs by only 1.8σ from the inclusive value, and $|V_{ub}|_{DLogs} = 3.72(6) \times 10^{-3}$ with an uncertainty of 1.6% and a deviation of 2σ from the inclusive value.

The process of performing a combined fit to both decays also tests for their compatibility, and the result is a $|V_{ub}|$ that stays $\sim 1\sigma$ (PAs) or even $\sim 2\sigma$ (D-Logs) away from the $|V_{ub}|$ results extracted from the individual decay modes. In this sense, more precise measurements of the differential $B_s \rightarrow K \ell \nu_\ell$ decay distribution with a finer resolution of the q^2 bins will help achieve more conclusive results. Our value is presented and compared with other determinations using different methods and fitted data sets in Fig. 5.18. For this comparison we take the most precise determination for $|V_{ub}|$ between PAs and D-Logs for each stage. As seen, our value ($|V_{ub}|_{PAs\text{-comb}}$) is the most precise to date. The corresponding coefficients for this PAs for the $B \rightarrow \pi$ and $B_s \rightarrow K$ form factor are given in Table 5.13 together with their correlation matrix. The latter represents, to the best of our knowledge, the first correlated results for these form factors. As a benefit of our analysis, in Section 5.6 we have calculated different phenomenological observables such as total decay rates, ratio of τ -to- μ differential decay rates or the forward-backward asymmetry, and its normalized version,

¹⁶ 1.2σ with respect to the preliminary value $|V_{ub}| = 4.06(9)(16)(15) \times 10^{-3}$ [176].

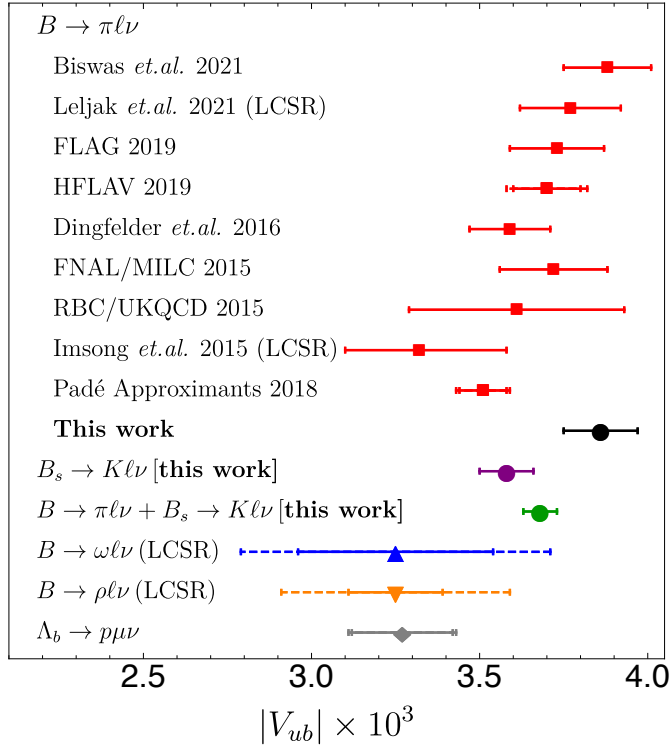


Figure 5.18: Status of $|V_{ub}|$ determinations from exclusive $B \rightarrow \pi l \nu_\ell$ decays (red squares) including Biswas et. al. [182], Leljak et. al. [183], FLAG 2019 [139], HFLAV 2019 [175], Dingfelder et. al. [184], FNAL/MILC 2015 [148], RBC/UKQCD [147], Imsong et. al. [185], Padé approximants [70] and this work (black circle) Eq. (5.70), from $B_s \rightarrow K \mu \nu_\mu$ (this work using D-Logs, purple circle), from a combination of $B \rightarrow \pi l \nu_\ell$ and $B_s \rightarrow K \mu \nu_\mu$ decays (this work using PAs, green circle) Eq. (5.75), from $B \rightarrow \omega l \nu_\ell$ (upward blue triangle) and $B \rightarrow \rho l \nu_\ell$ (downward orange triangle) [186], and from $\Lambda_b \rightarrow p \mu \nu_\mu$ (gray diamond) LHCb [163].

with an accuracy of few percentage.

Looking ahead, improvements in both experimental and theoretical fronts are anticipated. Experiments like Belle-II are expected to gather more precise data on $B_s \rightarrow K$ decays, while future lattice QCD calculations aim to reduce uncertainties in the form factors. These advancements will significantly enhance the precision of exclusive $|V_{ub}|$ determinations, providing a clearer picture of this fundamental parameter in the Standard Model.

Findings and Conclusions

We have observed that both Padé approximants and D-Log Padé approximants exhibit rapid convergence in their canonical constructions, clearly adhering to the convergence patterns outlined in Chapter 2. Additionally, the convergence range for both methods extends beyond the radius of convergence of the Taylor expansion, at least in the cases analyzed. Identifying whether the function being approximated is meromorphic or of Stieltjes type provides valuable guidance in selecting the appropriate sequences for optimal approximation. While both methods display similar convergence behavior in the initial approximants, PAs usually offer a better approximation at the beginning of the sequences. However, at higher orders, the D-Log Padé approximants generally yield superior accuracy, as illustrated in Fig. 4.3 and Table 5.3.

Furthermore, when used as a fitting tool, both PAs and D-Logs demonstrate their effectiveness, offering valuable advantages. For instance, they can easily incorporate the unitarity of the function and help identify potential outliers in the data. In the case of Stieltjes functions, these approximants exhibit a convergence pattern with two sequences—one converging from above and the other from below—allowing for the estimation of a systematic error, a feature absent in many other parameterisations. Both methods are model-independent, providing reliable approximations, yet they retain the flexibility to incorporate prior knowledge, thereby reducing the number of parameters required in the fitting process. In applications such as the determination of V_{ub} and the anomalous magnetic moment of the muon ($a_\mu^{\text{HVP,LO}}$), both approaches achieved uncertainties that have not been matched by other methods to date.

In Chapter 4 we showed that the systematic use of PAs and D-Logs as model-independent fitting functions to the future MUonE data can provide a powerful framework for the extraction of the anomalous magnetic moment of the muon ($a_\mu^{\text{HVP, LO}}$). Our explorations show that this method is superior to the use of a single, fixed, fitting function, which may carry a model dependence and an associated systematic uncertainty that would be difficult to estimate on the basis of real experimental data. The nicest feature of the method is the fact that we expect different sequences to bound the true value, which renders the average of results from these two sequences superior to the estimate arising from a single approximant. This bounding property is guaranteed by theorems for approximants canonically built to Stieltjes functions, i.e. to their Taylor series. In the case where they are employed as fitting functions, we found strong evidence that this convergence pattern is still respected for the central values obtained for each approximant. Therefore, the PAs and D-Logs provide the basis for a model-independent and systematic method, relying only on the analytical structure of the two-point correlator underlying $a_\mu^{\text{HVP, LO}}$, that is able to yield a result with a competitive, although conservative, uncertainty.

In Chapter 5, we investigated the role of the decay $B_s \rightarrow K\mu\nu_\mu$ as a complementary process to the more traditional $B \rightarrow \pi\ell\nu_\ell$ decay in determining the CKM matrix element $|V_{ub}|$. Motivated by recent experimental measurements from the LHCb Collaboration, our analysis employed two main techniques —Padé and D-Log Padé approximants— applied to the form factors of both decay channels. Our results from $B \rightarrow \pi$ yielded values of $|V_{ub}|$ around $3.86(11) \times 10^{-3}$ ($3.80(7) \times 10^{-3}$) for PAs(D-Logs), in slight tension with the inclusive decay determination. In contrast, the $B_s \rightarrow K$ decay produced lower values, around $3.58(9) \times 10^{-3}$ ($3.56(8) \times 10^{-3}$) using PAs(D-Logs), with significant shifts of up to 3σ compared to the $B \rightarrow \pi$ results.

The combined fit of both decays, utilizing all available experimental and lattice QCD input, provided a more precise determination of $|V_{ub}|$ using PAs with $|V_{ub}| = 3.68(5) \times 10^{-3}$, with an impressive uncertainty of 1.4%. The final results differed only modestly (1.2σ - 1.8σ) from the inclusive decay value, reducing the tension observed in individual decay mode analyses. However, the discrepancy between $B_s \rightarrow K$ and $B \rightarrow \pi$ results suggests that more precise data, particularly in $B_s \rightarrow K$ decays, is needed to resolve this issue fully.

Looking ahead, improvements in both experimental and theoretical fronts are anticipated. Experiments like Belle-II are expected to gather more precise data on $B_s \rightarrow K$ decays, while future lattice QCD calculations aim to reduce uncertainties in the form factors. These advancements will significantly enhance the precision of exclusive $|V_{ub}|$ determinations, providing a clearer picture of this fundamental parameter in the Standard Model.

Notation

Here we are going to introduce some notation. We will adopt the unit system that is most convenient for high energy physics, where the speed of light provides the natural scale and quantum effects are not necessarily small, it is:

$$c = 1 = \hbar.$$

We write four-vectors with upper and lower indices, where the metric tensor $g_{\mu\nu}$ is defined by:

$$g_{\mu\nu} = \text{diag}[1, -1, -1, -1],$$

which it can be used to raise or lower indices, as:

$$x^\mu = (t, \vec{x}), \quad x_\mu = g_{\mu\nu}x^\nu = (t, -\vec{x})$$

with the usual convention of summing over repeated indices. The antisymmetric tensor $\epsilon^{\mu\nu\rho\sigma}$ is taken as:

$$\epsilon^{0123} = -\epsilon_{0123} = 1.$$

Therefore, we have for time-like quantities $q^2 > 0$, whereas for space-like quantities, $q^2 < 0$, which is often noted in capital letters as $Q^2 \equiv -q^2 > 0$.

The slashed notation, $\gamma^\mu k^\nu g_{\mu\nu} \equiv \not{k}$ where γ^μ is the Dirac matrix with the following

representation:

$$\gamma^0 = \begin{pmatrix} 1 & 0 \\ 0 & -1 \end{pmatrix}, \quad \gamma^i = \begin{pmatrix} 0 & \sigma^i \\ -\sigma^i & 0 \end{pmatrix}$$

where σ^i are the Pauli matrices. In addition we can define;

$$\gamma^5 = i\gamma^0\gamma^1\gamma^2\gamma^3 = \begin{pmatrix} 0 & 1 \\ 1 & 0 \end{pmatrix}$$

Finally we have to defined the GellMann matrices as;

$$\lambda_1 = \begin{pmatrix} 0 & 1 & 0 \\ 1 & 0 & 0 \\ 0 & 0 & 0 \end{pmatrix}, \quad \lambda_2 = \begin{pmatrix} 0 & -i & 0 \\ i & 0 & 0 \\ 0 & 0 & 0 \end{pmatrix}, \quad \lambda_3 = \begin{pmatrix} 1 & 0 & 0 \\ 0 & -1 & 0 \\ 0 & 0 & 0 \end{pmatrix}$$

$$\lambda_4 = \begin{pmatrix} 0 & 0 & 1 \\ 0 & 0 & 0 \\ 1 & 0 & 0 \end{pmatrix}, \quad \lambda_5 = \begin{pmatrix} 0 & 0 & -i \\ 0 & 0 & 0 \\ i & 0 & 0 \end{pmatrix}$$

$$\lambda_6 = \begin{pmatrix} 0 & 0 & 0 \\ 0 & 0 & 1 \\ 0 & 1 & 0 \end{pmatrix}, \quad \lambda_7 = \begin{pmatrix} 0 & 0 & 0 \\ 0 & 0 & -i \\ 0 & i & 0 \end{pmatrix}, \quad \lambda_8 = \frac{1}{\sqrt{3}} \begin{pmatrix} 1 & 0 & 0 \\ 0 & 1 & 0 \\ 0 & 0 & -2 \end{pmatrix}$$

Fitting functions for PAs and D-Logs

In this appendix we give the explicit expressions of the approximants used in this work as a function of x and in terms of the unknown Taylor coefficients a_n of $\Delta\alpha_{\text{had}}$.

We start with the sequence P_N^N , where the first PA is P_1^1 . As seen in Sec. 2.1, the fitting function is

$$P_1^1(x) = -\frac{b_1 m_\mu^2 x^2}{1 - x + b_2 m_\mu^2 x^2}, \quad (\text{B.1})$$

with $b_1 = a_1$ and $b_2 = a_2/a_1$. The constraints employed are $b_1 < 0$ and $b_2 > 1$. The next approximant in this sequence is P_2^2 , whose final expression is

$$P_2^2(x) = \frac{b_1 m_\mu^2 x^2 (x - 1) + (b_2 - b_1 b_3) m_\mu^4 x^4}{(1 - x)^2 + b_3 m_\mu^2 x^2 (1 - x) + b_4 m_\mu^4 x^4}, \quad (\text{B.2})$$

where the fit parameters are now

$$b_1 = a_1, \quad b_2 = a_2, \quad b_3 = \frac{a_2 a_3 - a_1 a_4}{a_2^2 - a_1 a_3}, \quad b_4 = \frac{a_3^2 - a_2 a_4}{a_2^2 - a_1 a_3}. \quad (\text{B.3})$$

From the structure of $\Delta\alpha_{\text{had}}$ and its series representation in Eq. (4.13), we know that $b_1 < 0$ and $b_2 < b_1$. Analyzing the Stieltjes determinants of Eq. (2.12), we get the additional relations: $b_3 > 0$ and $b_4 > 0$. Since the other approximants of the sequence P_N^N were not applied to the realistic data sets, we will refrain from showing their expressions here.

The P_N^{N+1} sequence starts with P_1^2 , which reads, as a function of x

$$P_1^2(x) = -\frac{b_1 m_\mu^2 x^2 (1-x) + (b_1 b_3 - b_2) m_\mu^4 x^4}{(1-x)^2 + b_3 m_\mu^2 x^2 (1-x)}. \quad (\text{B.4})$$

The b_n parameters in this case, together with their limits, are

$$b_1 = a_1 < 0, \quad b_2 = a_2 < b_1, \quad b_3 = \frac{a_3}{a_2} > 1. \quad (\text{B.5})$$

The last approximant used is P_2^3 , which is given by

$$P_2^3(x) = -\frac{b_1 m_\mu^2 x^2 (1-x)^2 - (b_2 + b_1 b_4) m_\mu^4 x^4 (1-x) + (b_3 + b_1 b_5 + b_2 b_4) m_\mu^6 x^6}{(1-x)^3 - b_4 m_\mu^2 x^2 (1-x)^2 + b_5 m_\mu^4 x^4 (1-x)}, \quad (\text{B.6})$$

where the parameters are

$$b_1 = a_1, \quad b_2 = a_2, \quad b_3 = a_3, \quad b_4 = \frac{a_2 a_5 - a_3 a_4}{a_3^2 - a_2 a_4}, \quad b_5 = \frac{a_4^2 - a_3 a_5}{a_3^2 - a_2 a_4}. \quad (\text{B.7})$$

In addition, the constraints employed in the fits are: $b_3 < b_2 < b_1 < 0$, $b_4 < 0$ and $b_5 > 0$. It is important to stress that all the constraints showed in this Appendix are model independent, since they follow from the fact that $\Delta\alpha_{\text{had}}(t)$ is a Stieltjes function.

The D-Logs are constructed from the Taylor series as was described in Sec. 2.2.1 and reparametrized in terms of the x variable. All the functions employed for fitting purposes are detailed in Tab. 4.2.

B-meson Form Factors simulation & correlation tables

Table C.1: Best fit values, uncertainties and correlation matrix for the output quantities of our best $\chi^2_{B\pi}$ fit Eq. (5.64) obtained with the Padé element $\mathbb{P}_{1,1}^2$ (cf. Table 5.6).

Parameter	Central value	Correlation matrix						
$ V_{ub} \times 10^3$	3.86(11)	1	-0.571	0.035	0.324	-0.251	0.139	-0.121
a_0^+	0.247(8)		1	-0.374	0.341	-0.298	-0.719	-0.473
$a_1^+ \times 10^3$	-1.3(8)			1	0.028	-0.297	0.220	0.105
$a_2^+ \times 10^4$	-0.3(1.0)				1	-0.958	-0.681	-0.795
$m_{B^*(1^-)} \text{ pole(s) [GeV]}$	= 5.325&6.46					1	0.633	0.747
$a_1^0 \times 10^2$	-0.4(1)						1	0.943
$m_{B^*(0^+)} \text{ pole(s) [GeV]}$	5.44							1

Table C.2: Central values, errors and correlation matrix for the $B \rightarrow \pi$ vector form factor, $f_+(q^2)$, generated at three representative values of q^2 from the FLAG [139] results and used in our fits in Table 5.7.

Form factor	q^2 [GeV ²]	Central values	Correlation matrix		
			$f_+^{B\pi}$		
			18	22	26
$f_+^{B\pi}$	18	1.102(44)	1	0.757	0.563
	22	1.964(54)		1	0.400
	26	5.848(226)			1

Table C.3: Best fit values, uncertainties and correlation matrix for the output quantities of our best $\chi_{B_s K}^2$ fit Eq. (5.71) obtained with the Padé element $\mathbb{P}_{1,1}^3$ (cf. Table 5.11).

Parameter	Central value	Correlation matrix						
$ V_{ub} \times 10^3$	3.58(9)	1	-0.674	-0.332	0.168	-0.254	0.306	-0.445
a_0^+	0.214(5)		1	0.035	0.056	0.004	-0.028	0.784
$a_1^+ \times 10^3$	6.70(5.40)			1	-0.945	0.982	-0.997	-0.061
$a_2^+ \times 10^4$	-0.48(46)				1	-0.988	0.963	0.149
$a_3^+ \times 10^5$	1.04(96)					1	-0.992	-0.077
$m_{B^*(1-)} \text{ pole(s) [GeV]}$	= 5.325&29.5						1	0.037
$m_{B^*(0+)} \text{ pole(s) [GeV]}$	5.70							1

Bibliography

- [1] D. J. Gross and F. Wilczek, *Asymptotically free gauge theories. i*, *Physical Review D* **8** (1973) 3633.
- [2] H. D. Politzer, *Reliable perturbative results for strong interactions?*, *Physical Review Letters* **30** (1973) 1346.
- [3] H. Fritzsch, M. Gell-Mann and H. Leutwyler, *Current algebra: Quarks and what else?*, *Physics Letters B* **47** (1973) 365.
- [4] M. E. Peskin and D. V. Schroeder, *An Introduction to Quantum Field Theory*. Addison-Wesley, 1995.
- [5] PARTICLE DATA GROUP collaboration, *Review of Particle Physics*, *Prog. Theor. Exp. Phys.* **2022** (2022) 083C01.
- [6] K. G. Wilson, *Confinement of quarks*, *Phys. Rev. D* **10** (1974) 2445.
- [7] J. Greensite, *An Introduction to the Confinement Problem*. Springer Science & Business Media, 2011.
- [8] Y. Nambu, *Strings, monopoles, and gauge fields*, *Physical Review D* **10** (1974) 4262.
- [9] A. Jaffe and E. Witten, “Yang-mills and mass gap.” Clay Mathematics Institute, 2000.
- [10] A. J. Gentles, *Non-Perturbative QCD on the Continuum : Solving the Dyson-Schwinger Equations*, pp. 145–152. Springer US, Boston, MA, 1995. 10.1007/978-1-4899-1082-0_5.
- [11] S. Weinberg, *The quantum theory of fields*, vol. 2. Cambridge University Press, Cambridge, 2000.

- [12] G. Ecker, *Chiral perturbation theory*, *Progress in Particle and Nuclear Physics* **35** (1995) 1.
- [13] J. Gasser and H. Leutwyler, *Chiral perturbation theory to one loop*, *Annals of Physics* **158** (1984) 142.
- [14] J. Gasser and H. Leutwyler, *Chiral perturbation theory: Expansions in the mass of the strange quark*, *Nucl. Phys.* **B250** (1985) 465.
- [15] S. Weinberg, *Phenomenological lagrangians*, *Physica A: Statistical Mechanics and its Applications* **96** (1979) 327.
- [16] P. Sanchez-Puertas, *A theoretical study of meson transition form factors*, Ph.D. thesis, Fachbereich Physik, Mathematik und Informatik der Johannes Gutenberg-Universität Mainz, 2018. [1709.04792](#).
- [17] V. Bernard, *Chiral perturbation theory and baryon properties*, *Progress in Particle and Nuclear Physics* **60** (2008) 82.
- [18] S. Scherer, *Introduction to chiral perturbation theory*, vol. 27, pp. 277–538. Springer New York, NY, 2003. [hep-ph/0210398](#). [10.1007/0-306-47916-6_3](#).
- [19] T. Horn and C. D. Roberts, *The pion: an enigma within the standard model*, *Journal of Physics G: Nuclear and Particle Physics* **43** (2016) 073001.
- [20] P. Masjuan, S. Peris and J. J. Sanz-Cillero, *Vector Meson Dominance as a first step in a systematic approximation: The Pion vector form-factor*, *Phys. Rev. D* **78** (2008) 074028 [[0807.4893](#)].
- [21] J. A. Oller, E. Oset and J. E. Palomar, *Pion and kaon vector form factors*, *Phys. Rev. D* **63** (2001) 114009.
- [22] J. Bijnens and P. Talavera, *Pion and kaon electromagnetic form factors*, *Journal of High Energy Physics* **2002** (2002) 046.
- [23] G. t Hooft, *'t hooft limit in gauge theories*, *Nuclear Physics B* **72** (1974) 461.
- [24] E. Jenkins, *QCD Baryons in the $1/N_c$ Expansion*, *AIP Conference Proceedings* **623** (2002) 36
[https://pubs.aip.org/aip/acp/article-pdf/623/1/36/11733982/36_1_online.pdf].
- [25] E. Witten, *Baryons in the $1/n_c$ expansion*, *Nuclear Physics B* **160** (1979) 57.

-
- [26] S. Peris, M. Perrottet and E. de Rafael, *Matching long and short distances in large- n_c qcd*, *Journal of High Energy Physics* **1998** (1998) 011.
- [27] S. Peris, B. Phily and E. de Rafael, *Tests of large N_c qcd from hadronic τ decay*, *Phys. Rev. Lett.* **86** (2001) 14.
- [28] E. de Rafael, *Minimal hadronic ansatz to large n_c qcd and hadronic τ -decay*, *Nuclear Physics B - Proceedings Supplements* **96** (2001) 316.
- [29] P. D. Ruiz-Femenia et al., *Minimal hadronic approximation to large- n_c qcd and the pseudoscalar masses*, *Journal of High Energy Physics* **2003** (2003) 011.
- [30] R. F. Lebed, *Phenomenology of large $N(c)$ QCD*, *Czech. J. Phys.* **49** (1999) 1273 [[nucl-th/9810080](#)].
- [31] A. V. Manohar, *Large N QCD*, in *Probing the Standard Model of Particle Interactions, Proceedings of the NATO Advanced Study Institute Summer School in Theoretical Physics, Les Houches, France, July 28-September 5, 1997*, pp. 1091–1169, 1998, [hep-ph/9802419](#).
- [32] N. Cabibbo, *Unitary symmetry and leptonic decays*, *Phys. Rev. Lett.* **10** (1963) 531.
- [33] M. Kobayashi and T. Maskawa, *CP-Violation in the Renormalizable Theory of Weak Interaction*, *Progress of Theoretical Physics* **49** (1973) 652 [<https://academic.oup.com/ptp/article-pdf/49/2/652/5257692/49-2-652.pdf>].
- [34] T. Nakada, *B mesons and cp violation: A new frontier*, *Reports on Progress in Physics* **68** (2005) 583.
- [35] A. coll UTfit, Bevan, M. Bona, M. Ciuchini, D. Derkach, M. Pierini, E. Franco et al., *Cp violation theory*, in *Proceedings for 14th International Conference on B-Physics at Hadron Machines (Beauty 2013)*, CERN, 2013.
- [36] U. Collaboration, M. Bona, M. Ciuchini, D. Derkach, F. Ferrari, E. Franco et al., *New utfit analysis of the unitarity triangle in the cabibbo-kobayashi-maskawa scheme*, 2022.
- [37] M. Davier, A. Hoecker and Z. Zhang, *The hadronic contribution to the muon anomalous magnetic moment*, *The European Physical Journal C* **71** (2010) 1515.
- [38] M. Davier, A. Hoecker, B. Malaescu and Z. Zhang, *Reevaluation of the hadronic vacuum polarisation contributions to the Standard Model predictions of the muon*

- $g - 2$ and $\alpha(m_Z^2)$ using newest hadronic cross-section data, *Eur. Phys. J. C* **77** (2017) 827 [[1706.09436](#)].
- [39] M. Davier, A. Hoecker, B. Malaescu and Z. Zhang, *A new evaluation of the hadronic vacuum polarisation contributions to the muon anomalous magnetic moment and to $\alpha(m_Z^2)$* , *Eur. Phys. J. C* **80** (2020) 241 [[1908.00921](#)].
- [40] P. Masjuan and P. Sanchez-Puertas, *Pseudoscalar-pole contribution to the $(g_\mu - 2)$: a rational approach*, *Phys. Rev. D* **95** (2017) 054026 [[1701.05829](#)].
- [41] T. Aoyama et al., *The anomalous magnetic moment of the muon in the Standard Model*, *Phys. Rept.* **887** (2020) 1 [[2006.04822](#)].
- [42] MUON $g-2$ collaboration, *Measurement of the positive muon anomalous magnetic moment to 0.46 ppm*, *Phys. Rev. Lett.* **126** (2021) 141801 [[2104.03281](#)].
- [43] MUON $g-2$ collaboration, *Measurement of the Positive Muon Anomalous Magnetic Moment to 0.20 ppm*, *Phys. Rev. Lett.* **131** (2023) 161802 [[2308.06230](#)].
- [44] MUON $g-2$ collaboration, *Final report of the muon $e821$ anomalous magnetic moment measurement at bnl*, *Phys. Rev. D* **73** (2006) 072003 [[hep-ex/0602035](#)].
- [45] G. Hardy, *Divergent Series*. Oxford University Press, 1949, [10.2307/3611423](#).
- [46] L. KANTOROVICH and G. AKILOV, *Xiv - a general theory of approximation methods*, in *Functional Analysis (Second Edition)*, L. KANTOROVICH and G. AKILOV, eds., pp. 401–442, Pergamon, (1982), [DOI](#).
- [47] C. M. Bender and S. A. Orszag, **Advanced mathematical methods for scientists and engineers I: Asymptotic methods and perturbation theory**. Springer Science & Business Media, 2013.
- [48] H. Padé, *Sur la représentation approchée d'une fonction par des fractions rationnelles*, Ph.D. thesis, Université de Paris, Paris, France, 1892.
- [49] C. Brezinski, *History of continued fractions and Padé approximants*, vol. 12. Springer Science & Business Media, 2012.
- [50] C. Brezinski, *Extrapolation algorithms and padé approximations: a historical survey*, *Applied Numerical Mathematics* **20** (1996) 299.

-
- [51] G. A. Baker Jr, **Essentials of Padé approximants**. Academic Press, New York, 1975.
- [52] G. A. Baker and P. Graves-Morris, **Padé approximants**. Cambridge University Press, Cambridge, 2nd ed., 1996.
- [53] P. Masjuan Queralt, *Rational Approximations in Quantum Chromodynamics*, Ph.D. thesis, Universitat Autònoma de Barcelona, 2010. [1005.5683](#).
- [54] H. Vazquez-Leal, B. Benhammouda, U. Filobello-Nino et al., *Direct application of padé approximant for solving nonlinear differential equations*, *SpringerPlus* **3** (2014) 563.
- [55] I. Andrianov and A. Shatrov, *Padé approximants, their properties, and applications to hydrodynamic problems*, *Symmetry* **13** (2021) .
- [56] F. Zullo, *Lommel functions, padé approximants and hypergeometric functions*, 2024.
- [57] E. O. Dobrolyubov, N. R. Ikononov, L. A. Knizhnerman and S. P. Suetin, *Rational hermite-padé approximants vs padé approximants. numerical results*, 2023.
- [58] M. Froissart, *Asymptotic behavior and subtractions in the mandelstam representation*, *Phys. Rev.* **123** (1961) 1053.
- [59] J. Gilewicz and Y. Kryakin, *Froissart doublets in padé approximation in the case of polynomial noise*, *Journal of Computational and Applied Mathematics* **153** (2003) 235.
- [60] P. Masjuan, J. J. Sanz-Cillero and J. Virto, *Some remarks on the padé unitarization of low-energy amplitudes*, *Physics Letters, Section B: Nuclear, Elementary Particle and High-Energy Physics* **668** (2008) 14.
- [61] P. Masjuan and S. Peris, *Padé theory applied to the vacuum polarization of a heavy quark*, *Physics Letters, Section B: Nuclear, Elementary Particle and High-Energy Physics* **686** (2010) 307.
- [62] R. d. Montessus, *Sur les fractions continues algébriques*, *Bulletin de la Société Mathématique de France* **30** (1902) 28.
- [63] S. Peris, *Large- n c qcd and pade approximant theory*, *Physical Review D—Particles, Fields, Gravitation, and Cosmology* **74** (2006) 054013.

- [64] P. Masjuan and S. Peris, *A rational approach to resonance saturation in large- n_c qcd*, *Journal of High Energy Physics* **2007** (2007) 040.
- [65] J. J. Sanz-Cillero, *Padé theory and phenomenology of resonance poles*, in *Proceedings of the Conference on Approximation and Extrapolation of Convergent and Divergent Sequences and Series*, 2010, <https://arxiv.org/abs/1002.3512> [[1002.3512](#)].
- [66] C. Pommerenke, *Padé approximants and convergence in capacity*, *Journal of Mathematical Analysis and Applications* **41** (1973) 775.
- [67] P. Masjuan and S. Peris, *A Rational approximation to $\langle VV-AA \rangle$ and its $O(p^6)$ low-energy constant*, *Phys. Lett. B* **663** (2008) 61 [[0801.3558](#)].
- [68] G. Allen, C. Chui, W. Madych, F. Narcowich and P. Smith, *Padé approximation of stieltjes series*, *Journal of Approximation Theory* **14** (1975) 302.
- [69] B. Simon, *Large orders and summability of eigenvalue perturbation theory: A mathematical overview*, *International Journal of Quantum Chemistry* **21** (1982) 3.
- [70] S. González-Solís and P. Masjuan, *Study of $b \rightarrow \pi \ell \nu_\ell$ and $b^+ \rightarrow \eta^{(\prime)} \ell^+ \nu_\ell$ decays and determination of $|v_{ub}|$* , *Physical Review D* **98** (2018) .
- [71] M. Knecht and E. de Rafael, *Patterns of spontaneous chiral symmetry breaking in the large- n_c limit of qcd-like theories*, *Physics Letters B* **424** (1998) 335.
- [72] S. Peris, M. Perrottet and E. De Rafael, *Matching long and short distances in large- n_c qcd*, *Journal of High Energy Physics* **1998** (1998) 011.
- [73] E. de Rafael, *Analytic approaches to kaon physics*, *Nuclear Physics B-Proceedings Supplements* **119** (2003) 71.
- [74] S. Peris, *Electroweak matrix elements at large N_c : matching quarks to mesons*, pp. 259–269. World Scientific, 2002.
https://www.worldscientific.com/doi/pdf/10.1142/9789812776914_0024.
10.1142/9789812776914_0024.
- [75] A. Pich, *Present status of chiral perturbation theory*, *International Journal of Modern Physics A* **20** (2005) 1613.
- [76] H. Stahl, *The convergence of padé approximants to functions with branch points*, *Journal of Approximation Theory* **91** (1997) 139.

-
- [77] G. A. Baker, *Application of the padé approximant method to the investigation of some magnetic properties of the ising model*, *Phys. Rev.* **124** (1961) 768.
- [78] G. A. Baker, H. E. Gilbert, J. Eve and G. S. Rushbrooke, *High-temperature expansions for the spin- $\frac{1}{2}$ heisenberg model*, *Phys. Rev.* **164** (1967) 800.
- [79] G. A. Baker Jr and D. Hunter, *Methods of series analysis. ii. generalized and extended methods with application to the ising model*, *Physical Review B* **7** (1973) 3377.
- [80] G. A. Baker, *Analysis of hyperscaling in the ising model by the high-temperature series method*, *Phys. Rev. B* **15** (1977) 1552.
- [81] D. Boito, C. Y. London, P. Masjuan and C. Rojas, *Model-independent extrapolation of muone data with padé and d-log approximants*, *arXiv preprint arXiv:2405.13638* (2024) .
- [82] D. Boito, M. Golterman, K. Maltman and S. Peris, *Spectral-weight sum rules for the hadronic vacuum polarization*, *Phys. Rev. D* **107** (2023) 034512 [2210.13677].
- [83] D. Boito, C. Y. London and P. Masjuan, *Higher-order QCD corrections to $H \rightarrow b\bar{b}$ from rational approximants*, *JHEP* **01** (2022) 054 [2110.09909].
- [84] D. Boito, P. Masjuan and F. Oliani, *Higher-order QCD corrections to hadronic τ decays from Padé approximants*, *JHEP* **08** (2018) 075 [1807.01567].
- [85] P. Masjuan, *$\gamma * \gamma \rightarrow \pi^0$ transition form factor at low-energies from a model-independent approach*, *Phys. Rev. D* **86** (2012) 094021 [1206.2549].
- [86] P. Masjuan and J. J. Sanz-Cillero, *Padé approximants and resonance poles*, *Eur. Phys. J. C* **73** (2013) 2594 [1306.6308].
- [87] R. Escribano, P. Masjuan and P. Sanchez-Puertas, *η and η' transition form factors from rational approximants*, *Phys. Rev. D* **89** (2014) 034014 [1307.2061].
- [88] R. Escribano, S. González-Solís, P. Masjuan and P. Sanchez-Puertas, *η' transition form factor from space- and timelike experimental data*, *Phys. Rev. D* **94** (2016) 054033 [1512.07520].
- [89] K. Knopp, *Theory of Functions, Part II*. Dover Publications, New York, 1996.

- [90] J. B. Conway, *Functions of One Complex Variable I*. Springer, New York, 2nd ed., 1995.
- [91] V. Puiseux, *Recherches sur les fonctions algébriques*, *Journal de Mathématiques Pures et Appliquées* **15** (1850) 365.
- [92] T. Aoyama, M. Hayakawa, T. Kinoshita and M. Nio, *Complete Tenth-Order QED Contribution to the Muon $g-2$* , *Phys. Rev. Lett.* **109** (2012) 111808 [[1205.5370](#)].
- [93] T. Aoyama, T. Kinoshita and M. Nio, *Theory of the Anomalous Magnetic Moment of the Electron*, *Atoms* **7** (2019) 28.
- [94] A. Czarnecki, W. J. Marciano and A. Vainshtein, *Refinements in electroweak contributions to the muon anomalous magnetic moment*, *Phys. Rev. D* **67** (2003) 073006 [[hep-ph/0212229](#)].
- [95] C. Gnendiger, D. Stöckinger and H. Stöckinger-Kim, *The electroweak contributions to $(g - 2)_\mu$ after the Higgs boson mass measurement*, *Phys. Rev. D* **88** (2013) 053005 [[1306.5546](#)].
- [96] A. Keshavarzi, D. Nomura and T. Teubner, *Muon $g - 2$ and $\alpha(M_Z^2)$: a new data-based analysis*, *Phys. Rev. D* **97** (2018) 114025 [[1802.02995](#)].
- [97] A. Keshavarzi, D. Nomura and T. Teubner, *$g - 2$ of charged leptons, $\alpha(M_Z^2)$, and the hyperfine splitting of muonium*, *Phys. Rev. D* **101** (2020) 014029 [[1911.00367](#)].
- [98] G. Colangelo, M. Hoferichter and P. Stoffer, *Two-pion contribution to hadronic vacuum polarization*, *JHEP* **02** (2019) 006 [[1810.00007](#)].
- [99] M. Hoferichter, B.-L. Hoid and B. Kubis, *Three-pion contribution to hadronic vacuum polarization*, *JHEP* **08** (2019) 137 [[1907.01556](#)].
- [100] B.-L. Hoid, M. Hoferichter and B. Kubis, *Hadronic vacuum polarization and vector-meson resonance parameters from $e^+e^- \rightarrow \pi^0\gamma$* , *Eur. Phys. J. C* **80** (2020) 988 [[2007.12696](#)].
- [101] A. Kurz, T. Liu, P. Marquard and M. Steinhauser, *Hadronic contribution to the muon anomalous magnetic moment to next-to-next-to-leading order*, *Phys. Lett. B* **734** (2014) 144 [[1403.6400](#)].

-
- [102] K. Melnikov and A. Vainshtein, *Hadronic light-by-light scattering contribution to the muon anomalous magnetic moment revisited*, *Phys. Rev. D* **70** (2004) 113006 [[hep-ph/0312226](#)].
- [103] G. Colangelo, M. Hoferichter, M. Procura and P. Stoffer, *Rescattering effects in the hadronic-light-by-light contribution to the anomalous magnetic moment of the muon*, *Phys. Rev. Lett.* **118** (2017) 232001 [[1701.06554](#)].
- [104] G. Colangelo, M. Hoferichter, M. Procura and P. Stoffer, *Dispersion relation for hadronic light-by-light scattering: two-pion contributions*, *JHEP* **04** (2017) 161 [[1702.07347](#)].
- [105] M. Hoferichter, B.-L. Hoid, B. Kubis, S. Leupold and S. P. Schneider, *Pion-pole contribution to hadronic light-by-light scattering in the anomalous magnetic moment of the muon*, *Phys. Rev. Lett.* **121** (2018) 112002 [[1805.01471](#)].
- [106] M. Hoferichter, B.-L. Hoid, B. Kubis, S. Leupold and S. P. Schneider, *Dispersion relation for hadronic light-by-light scattering: pion pole*, *JHEP* **10** (2018) 141 [[1808.04823](#)].
- [107] A. Gérardin, H. B. Meyer and A. Nyffeler, *Lattice calculation of the pion transition form factor with $N_f = 2 + 1$ Wilson quarks*, *Phys. Rev. D* **100** (2019) 034520 [[1903.09471](#)].
- [108] J. Bijnens, N. Hermansson-Truedsson and A. Rodríguez-Sánchez, *Short-distance constraints for the HLbL contribution to the muon anomalous magnetic moment*, *Phys. Lett. B* **798** (2019) 134994 [[1908.03331](#)].
- [109] G. Colangelo, F. Hagelstein, M. Hoferichter, L. Laub and P. Stoffer, *Short-distance constraints on hadronic light-by-light scattering in the anomalous magnetic moment of the muon*, *Phys. Rev. D* **101** (2020) 051501 [[1910.11881](#)].
- [110] G. Colangelo, F. Hagelstein, M. Hoferichter, L. Laub and P. Stoffer, *Longitudinal short-distance constraints for the hadronic light-by-light contribution to $(g - 2)_\mu$ with large- N_c Regge models*, *JHEP* **03** (2020) 101 [[1910.13432](#)].
- [111] G. Colangelo, M. Hoferichter, A. Nyffeler, M. Passera and P. Stoffer, *Remarks on higher-order hadronic corrections to the muon $g-2$* , *Phys. Lett. B* **735** (2014) 90 [[1403.7512](#)].

- [112] T. Blum, N. Christ, M. Hayakawa, T. Izubuchi, L. Jin, C. Jung et al., *Hadronic Light-by-Light Scattering Contribution to the Muon Anomalous Magnetic Moment from Lattice QCD*, *Phys. Rev. Lett.* **124** (2020) 132002 [[1911.08123](#)].
- [113] S. Borsanyi et al., *Leading hadronic contribution to the muon magnetic moment from lattice QCD*, *Nature* **593** (2021) 51 [[2002.12347](#)].
- [114] P. Masjuan, A. Miranda and P. Roig, *τ data-driven evaluation of Euclidean windows for the hadronic vacuum polarization*, *Phys. Lett. B* **850** (2024) 138492 [[2305.20005](#)].
- [115] M. Hansen, A. Lupo and N. Tantalo, *Extraction of spectral densities from lattice correlators*, *Phys. Rev. D* **99** (2019) 094508 [[1903.06476](#)].
- [116] G. Bailas, S. Hashimoto and T. Ishikawa, *Reconstruction of smeared spectral function from Euclidean correlation functions*, *PTEP* **2020** (2020) 043B07 [[2001.11779](#)].
- [117] J. A. Miranda and P. Roig, *New τ -based evaluation of the hadronic contribution to the vacuum polarization piece of the muon anomalous magnetic moment*, *Phys. Rev. D* **102** (2020) 114017 [[2007.11019](#)].
- [118] C. M. Carloni Calame, M. Passera, L. Trentadue and G. Venanzoni, *A new approach to evaluate the leading hadronic corrections to the muon $g-2$* , *Phys. Lett. B* **746** (2015) 325 [[1504.02228](#)].
- [119] G. Abbiendi et al., *Measuring the leading hadronic contribution to the muon $g-2$ via μe scattering*, *Eur. Phys. J. C* **77** (2017) 139 [[1609.08987](#)].
- [120] G. Abbiendi, *Letter of intent: the MUonE project*, tech. rep., CERN, Geneva, 2019.
- [121] F. Ignatov, R. N. Pilato, T. Teubner and G. Venanzoni, *An alternative evaluation of the leading-order hadronic contribution to the muon $g - 2$ with MUonE*, *Phys. Lett. B* **848** (2024) 138344 [[2309.14205](#)].
- [122] G. Abbiendi, *Status of the MUonE experiment*, *Phys. Scripta* **97** (2022) 054007 [[2201.13177](#)].
- [123] D. Greynat and E. de Rafael, *Hadronic vacuum polarization and the MUonE proposal*, *JHEP* **05** (2022) 084 [[2202.10810](#)].
- [124] M. Golterman, K. Maltman and S. Peris, *New strategy for the lattice evaluation of the leading order hadronic contribution to $(g - 2)_\mu$* , *Phys. Rev. D* **90** (2014) 074508 [[1405.2389](#)].

-
- [125] O. Costin and G. V. Dunne, *Conformal and uniformizing maps in Borel analysis*, *Eur. Phys. J. ST* **230** (2021) 2679 [2108.01145].
- [126] G. Ballerini et al., *A feasibility test run for the MUonE project*, *Nucl. Instrum. Meth. A* **936** (2019) 636.
- [127] G. Abbiendi et al., *Results on multiple Coulomb scattering from 12 and 20 GeV electrons on carbon targets*, *JINST* **15** (2020) 01 [1905.11677].
- [128] G. Abbiendi et al., *A study of muon-electron elastic scattering in a test beam*, *JINST* **16** (2021) P06005 [2102.11111].
- [129] C. Bouchiat and L. Michel, *La résonance dans la diffusion méson π — méson π et le moment magnétique anormal du méson μ* , *J. Phys. Radium* **22** (1961) 121.
- [130] S. J. Brodsky and E. De Rafael, *Suggested boson-lepton pair couplings and the anomalous magnetic moment of the muon*, *Phys. Rev.* **168** (1968) 1620.
- [131] B. E. Lautrup and E. De Rafael, *Calculation of the sixth-order contribution from the fourth-order vacuum polarization to the difference of the anomalous magnetic moments of muon and electron*, *Phys. Rev.* **174** (1968) 1835.
- [132] B. e. Lautrup, A. Peterman and E. de Rafael, *Recent developments in the comparison between theory and experiments in quantum electrodynamics*, *Phys. Rept.* **3** (1972) 193.
- [133] D. Bernecker and H. B. Meyer, *Vector Correlators in Lattice QCD: Methods and applications*, *Eur. Phys. J. A* **47** (2011) 148 [1107.4388].
- [134] C. Aubin, T. Blum, M. Golterman and S. Peris, *Model-independent parametrization of the hadronic vacuum polarization and $g-2$ for the muon on the lattice*, *Phys. Rev. D* **86** (2012) 054509 [1205.3695].
- [135] T. Carleman, **Über die Approximation analytischer Funktionen durch lineare Aggregate von vorgegebenen Potenzen**. Almqvist & Wiksell, 1923.
- [136] V. V. Gligorov, *Quark flavor physics: Status and future prospects*, *International Journal of Modern Physics A* **38** (2023) 2330009 [<https://doi.org/10.1142/S0217751X23300090>].

- [137] R. Fleischer, *Cp violation in b decays: recent developments and future perspectives*, *The European Physical Journal Special Topics* **233** (2024) 391.
- [138] M. Martinelli, *Cp violation in the quark sector: Mixing matrix unitarity*, *Symmetry* **16** (2024) .
- [139] S. Aoki, Y. Aoki, D. Bečirević, T. Blum, G. Colangelo, S. Collins et al., *Flag review 2019: Flavour lattice averaging group (flag)*, *The European Physical Journal C* **80** (2020) .
- [140] P. A. Zyla, R. M. Barnett, J. Beringer, O. Dahl, D. A. Dwyer, D. E. Groom et al., *Review of particle physics*, *Progress of Theoretical and Experimental Physics* **2020** (2020) 1.
- [141] S. Gottlieb, *Lattice qcd impact on determination of ckm matrix: Status and prospects*, *Proceedings of Science* **363** (2019) .
- [142] S. González-Solis, P. Masjuan and C. Rojas, *Padé approximants to $b \rightarrow \pi \ell \nu_\ell$ and $B_s \rightarrow K \ell \nu_\ell$ and determination of $|V_{ub}|$* , *Phys. Rev. D* **104** (2021) 114041.
- [143] G. Ciezarek, M. Franco Sevilla, B. Hamilton et al., *A challenge to lepton universality in b-meson decays*, *Nature* **546** (2017) 227.
- [144] E. Kou, P. Urquijo, W. Altmannshofer, F. Beaujean, G. Bell, M. Beneke et al., *The belle ii physics book*, *Progress of Theoretical and Experimental Physics* **2019** (2019) .
- [145] A. Bharucha, *Two-loop corrections to the $b \rightarrow \pi$ form factor from qcd sum rules on the light-cone and $|v_{ub}|$* , *Journal of High Energy Physics* **2012** (2012) .
- [146] E. Gulez, A. Gray, M. Wingate, C. T. Davies, G. P. Lepage and J. Shigemitsu, *Erratum: B meson semileptonic form factors from unquenched lattice qcd (physical review d. particles, fields, gravitation and cosmology (2006) 73, (074502))*, *Physical Review D - Particles, Fields, Gravitation and Cosmology* **75** (2007) .
- [147] J. M. Flynn, T. Izubuchi, T. Kawanai, C. Lehner, A. Soni, R. S. V. D. Water et al., *$B \rightarrow \pi \nu$ and $bs \rightarrow k \nu$ form factors and $|v_{ub}|$ from 2+1-flavor lattice qcd with domain-wall light quarks and relativistic heavy quarks*, *Physical Review D - Particles, Fields, Gravitation and Cosmology* **91** (2015) .

-
- [148] J. A. Bailey, A. Bazavov, C. Bernard, C. M. Bouchard, C. DeTar, D. Du et al., *$|v_{ub}|$ from $b \rightarrow \pi \nu$ decays and (2+1)-flavor lattice qcd* , *Physical Review D - Particles, Fields, Gravitation and Cosmology* **92** (2015) .
- [149] D. Becirevic and A. B. Kaidalov, *Comment on the heavy \rightarrow light form factors*, *Physics Letters, Section B: Nuclear, Elementary Particle and High-Energy Physics* **478** (2000) 417.
- [150] P. Ball and R. Zwicky, *New results on $b \rightarrow \pi, k, \eta$ decay form factors from light-cone sum rules*, *Phys. Rev. D* **71** (2005) 014015.
- [151] C. G. Boyd, B. Grinstein and R. F. Lebed, *Constraints on form factors for exclusive semileptonic heavy to light meson decays*, *Physical Review Letters* **74** (1995) 4603.
- [152] C. Bourrely, L. Lellouch and I. Caprini, *Model-independent description of $b \rightarrow \pi \ell \nu$ decays and a determination of $|V_{ub}|$* , *Phys. Rev. D* **79** (2009) 013008.
- [153] N. E. Adam, J. P. Alexander, K. Berkelman, D. G. Cassel, J. E. Duboscq, R. Ehrlich et al., *Study of exclusive charmless semileptonic b decays and $|v_{ub}|$* , *Physical Review Letters* **99** (2007) .
- [154] B. Collaboration, P. D. A. Sanchez, J. P. Lees, V. Poireau, E. Prencipe, V. Tisserand et al., *Study of $b \rightarrow \pi \ell \nu$ and $b \rightarrow \rho \ell \nu$ decays and determination of $|v_{ub}|$* , *Physical Review D - Particles, Fields, Gravitation and Cosmology* **83** (2011) .
- [155] J. P. Lees, V. Poireau, V. Tisserand, J. G. Tico, E. Grauges, A. Palano et al., *Branching fraction and form-factor shape measurements of exclusive charmless semileptonic b decays, and determination of $|v_{ub}|$* , *Physical Review D - Particles, Fields, Gravitation and Cosmology* **86** (2012) .
- [156] H. Ha, E. Won, I. Adachi, H. Aihara, T. Aziz, A. M. Bakich et al., *Measurement of the decay $b_0 \rightarrow \pi^- \ell^+ \nu$ and determination of $|v_{ub}|$* , *Physical Review D - Particles, Fields, Gravitation and Cosmology* **83** (2011) .
- [157] A. Sibidanov, K. E. Varvell, I. Adachi, H. Aihara, D. M. Asner, V. Aulchenko et al., *Study of exclusive $b \rightarrow x_u \ell \nu$ decays and extraction of $|v_{ub}|$ using full reconstruction tagging at the belle experiment*, *Physical Review D - Particles, Fields, Gravitation and Cosmology* **88** (2013) .

- [158] C. M. Bouchard, G. P. Lepage, C. Monahan, H. Na and J. Shigemitsu, $b_s \rightarrow k \mu$ form factors from lattice qcd, *Physical Review D - Particles, Fields, Gravitation and Cosmology* **90** (2014) .
- [159] F. Bahr, D. Banerjee, F. Bernardoni, A. Joseph, M. Koren, H. Simma et al., Continuum limit of the leading-order hqet form factor in $b_s \rightarrow k \ell \nu$ decays, *Physics Letters, Section B: Nuclear, Elementary Particle and High-Energy Physics* **757** (2016) 473.
- [160] A. Bazavov, C. Bernard, C. Detar, D. Du, A. X. El-Khadra, E. D. Freeland et al., $b_s \rightarrow k \nu$ decay from lattice qcd, *Physical Review D* **100** (2019) .
- [161] R. Aaij, C. A. Beteta, T. Ackernley, B. Adeva, M. Adinolfi, H. Afsharnia et al., First observation of the decay $b_s^0 \rightarrow k^- \mu^+ \nu_\mu$ and a measurement of $|v_{ub}|/|v_{cb}|$, *Physical Review Letters* **126** (2021) .
- [162] X. W. Kang, B. Kubis, C. Hanhart and U. G. Meißner, B_4 decays and the extraction of $|v_{ub}|$, *Physical Review D - Particles, Fields, Gravitation and Cosmology* **89** (2014) .
- [163] R. Aaij, B. Adeva, M. Adinolfi, A. Affolder, Z. Ajaltouni, S. Akar et al., Determination of the quark coupling strength $|v_{ub}|$ using baryonic decays, *Nature Physics* **11** (2015) 743.
- [164] W. Detmold, C. Lehner and S. Meinel, $\lambda_b \rightarrow p \ell^- \nu_\ell$ and $\lambda_b \rightarrow \lambda_c \ell^- \nu_\ell$ form factors from lattice qcd with relativistic heavy quarks, *Physical Review D - Particles, Fields, Gravitation and Cosmology* **92** (2015) .
- [165] M. Wirbel, B. Stech and M. Bauer, Exclusive semileptonic decays of heavy mesons, *Zeitschrift für Physik C Particles and Fields* **29** (1985) 637.
- [166] B. Grinstein, M. B. Wise and N. Isgur, Weak mixing angles from semileptonic decays in the quark model, *Physical Review Letters* **56** (1986) 298.
- [167] S. Nussinov and W. Wetzel, Comparison of exclusive decay rates for bu and bc transitions, *Physical Review D* **36** (1987) 130.
- [168] M. Suzuki, The decay $\overline{B}_0 \rightarrow \pi^+ \ell^- \nu$ to probe $|v_{ub}|$, *Physical Review D* **37** (1988) 239.
- [169] C. Bourrely, L. Lellouch and I. Caprini, Erratum: Model-independent description of $b \rightarrow \pi \ell \nu$ decays and a determination of $|v_{ub}|$ (physical review d - particles, fields,

- gravitation and cosmology (2009) 79 (013008)*), *Physical Review D - Particles, Fields, Gravitation and Cosmology* **82** (2010) .
- [170] R. Eden, P. Landshoff, D. Olive and J. Polkinghorne, *The Analytic S-Matrix*. Cambridge University Press, Cambridge, 1966.
- [171] Y. Amhis, S. Banerjee, E. Ben-Haim, F. Bernlochner, A. Bozek, C. Bozzi et al., *Averages of b-hadron, c-hadron, and τ -lepton properties as of summer 2016*, *European Physical Journal C* **77** (2017) .
- [172] K. A. Olive and others (Particle Data Group), *Review of particle physics*, *Chinese Physics C* **38** (2014) 090001.
- [173] S. Aoki, Y. Aoki, D. Bećirević, C. Bernard, T. Blum, G. Colangelo et al., *Review of lattice results concerning low-energy particle physics: Flavour lattice averaging group (flag)*, *European Physical Journal C* **77** (2017) .
- [174] C. Lang, D. Mohler, S. Prelovsek and R. Woloshyn, *Predicting positive parity bs mesons from lattice qcd*, *Physics Letters B* **750** (2015) 17.
- [175] Y. Amhis, S. Banerjee, E. Ben-Haim, F. U. Bernlochner, M. Bona, A. Bozek et al., *Averages of b-hadron, c-hadron, and τ -lepton properties as of 2018: Heavy flavor averaging group (hflav)*, *European Physical Journal C* **81** (2021) .
- [176] L. Cao, *New results on inclusive $b \rightarrow x_{\{u\}}\ell\nu$ decay from the belle experiment*, .
- [177] G. Duplancić, A. Khodjamirian, T. Mannel, B. Melić and N. Offen, *Light-cone sum rules for $b \rightarrow \pi$ form factors revisited*, *Journal of High Energy Physics* **2008** (2008) .
- [178] G. Duplancić and B. Melić, *$b, b_s \rightarrow k$ form factors: An update of light-cone sum rule results*, *Physical Review D - Particles, Fields, Gravitation and Cosmology* **78** (2008) .
- [179] A. Khodjamirian and A. V. Rusov, *$b_s \rightarrow k_\ell\nu\ell$ and $b_s \rightarrow \pi k_\ell\ell^-$ decays at large recoil and ckm matrix elements*, *Journal of High Energy Physics* **2017** (2017) .
- [180] W. F. Wang and Z. J. Xiao, *Semileptonic decays $b/b_s \rightarrow (\pi, k)(l^+l^-, l\nu, \nu\bar{l})$ in the perturbative qcd approach beyond the leading order*, *Physical Review D - Particles, Fields, Gravitation and Cosmology* **86** (2012) .
- [181] R. N. Faustov and V. O. Galkin, *Charmless weak bs decays in the relativistic quark model*, *Physical Review D - Particles, Fields, Gravitation and Cosmology* **87** (2013) .

- [182] A. Biswas, S. Nandi, S. K. Patra and I. Ray, *A closer look at the extraction of $|v_{ub}|$ from $b \rightarrow \pi \ell \nu$* , *Journal of High Energy Physics* **2021** (2021) .
- [183] D. Lejnak, B. Melić and D. van Dyk, *The $b^- \rightarrow \pi$ form factors from qcd and their impact on $|v_{ub}|$* , *Journal of High Energy Physics* **2021** (2021) .
- [184] J. Dingfelder and T. Mannel, *Leptonic and semileptonic decays of b mesons*, *Reviews of Modern Physics* **88** (2016) .
- [185] I. S. Imson, A. Khodjamirian, T. Mannel and D. van Dyk, *Extrapolation and unitarity bounds for the $b \rightarrow \pi$ form factor*, *Journal of High Energy Physics* **2015** (2015) .
- [186] A. Bharucha, D. M. Straub and R. Zwicky, *$B \rightarrow v \ell^+ \ell^-$ in the standard model from light-cone sum rules*, *Journal of High Energy Physics* **2016** (2016) .